Computational Investigations of Single-Chain Nanoparticles:

Novel Synthesis Routes, Complex Flow Behavior and Reversible Gel Formation

by
Maud Formanek

Thesis supervisor:
Angel Moreno

University of the Basque Country (UPV/EHU)
Donostia - San Sebastián, December 2019

Nothing in life is to be feared,
it is only to be understood.
Now is the time to understand more,
so that we may fear less.

— Maria Skłodowska-Curie

Table of Contents

Chapter 1

Introduction

1.1   Preface

> *"Have fun on sea and land*
> *Unhappy it is to become famous*
> *Riches, honors, false glitters of this world*
> *All is but soap bubbles"*
> **No conclusion could be more appropriate today.**
> —Pierre-Gilles de Gennes, *Nobel lecture, 9.12.1991*

In 1991, Pierre-Gilles de Gennes won the Nobel prize in physics for his work on phase transitions driven by ordering in liquid crystals and polymers. He ended his acceptance speech, titled 'Soft Matter', with a poem found on a 1758 engraving by Daullé depicting an elegant young woman, seated on a wall and blowing soap bubbles next to a man gazing at her admiringly. Although de Gennes never explained why he chose the poem, and it might sound a bit obscure to some, I believe it beautifully alludes to the paradox standing soft matter had in the 20th century. During what some people term the *Polymer Age*, we have become surrounded more and more by synthetic soft matter products in our daily life, from the shampoo we use to wash our hair, the clothes we wear, the packaging of our foods, to the skyscrapers we build. *"All is but soap bubbles"* rings more true than ever. At the same time, the theoretical investigation and understanding of the typical constituents of soft materials, such as surfactants, polymers, liquid crystals, to name a few, has lagged behind the technological advances in the field. But more importantly, it has not received the attention it deserves. From my own experience as an undergraduate, despite the indisputable importance of soft matter in our everyday world, talented young students with a penchant for theory still dream of answering the 'big' questions in quantum physics, particle physics and relativity. Extremes are fascinating: be it the forces that hold quarks together (extremely small) or the curvature of spacetime (extremely big). Studying the intermediate lacks this aura of grandeur and might have seemed trivial in the beginning: In the world of the mesoscale, quantum effects can be neglected just as much as relativity. However, thanks to pioneering theoreticians in the field, such as Pierre-Gilles de Gennes, Sam Edwards or Paul Flory, we have begun to understand that the ordinary is not necessarily the simple. Emergent collective behaviors driven by the sum of small forces and the importance of entropy in molecules with many degrees of freedom make soft matter systems difficult to predict. Furthermore, the realization that all living matter is inherently soft matter and that remarkable insights can be gained from the treatment of living systems by means of statistical physics has brought soft matter physics to the attention of a broader community. Indeed, today, in the 21st century, soft

matter constitutes one of the fastest growing interdisciplinary research fields [1]. All is still but soap bubbles, but those bubbles shine brighter than ever.

1.2 Soft Matter, Polymers and Nanotechnology

Soft matter is a fairly loosely defined term encompassing a wide range of materials that share a few common characteristics. As the name suggests, they are 'soft': they can easily be deformed by mechanical stresses, because the strength of their molecular interactions are of the magnitude of thermal fluctuations k_BT at room temperature. Furthermore, they inhabit the mesoscale: their constituents are typically bigger than atoms or simple molecules ($\sim$ nm) , but smaller than what can be observed by the naked eye ($\sim$ 100 μm). Especially at the *nanoscale*, surface-to-volume ratios can become very large and materials exhibit interesting size-dependent properties different from the bulk.
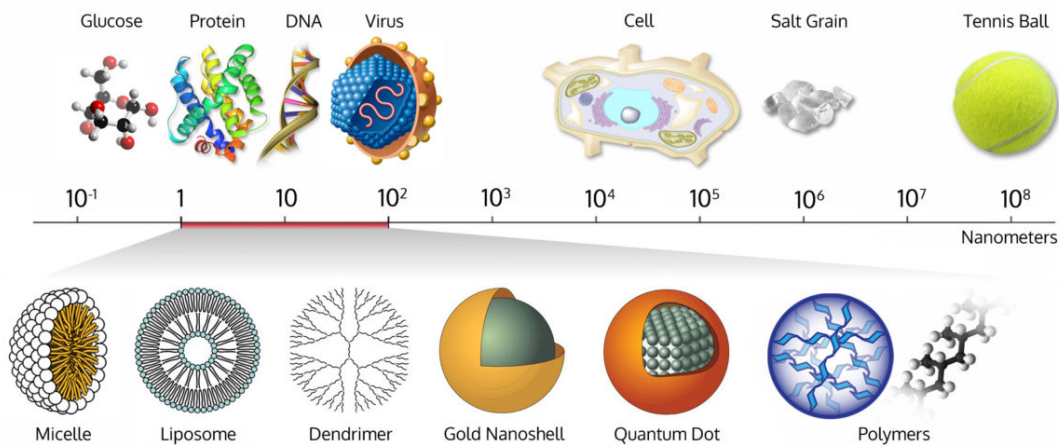
Figure 1.1: Examples of molecules, materials and objects inhabiting different scales. The nanoscale (1-100 nm) is highlighted, showing various synthetic nanoparticles. Reproduced with permission [2].

These two features of soft matter materials, mesoscopic size and low interaction strengths, lead to a phenomenon called *self-assembly*, in which molecules reversibly organize through hierarchical processes. Beginning with the formation of small clusters and aggregates, the summation of various interactions and their interplay with entropic contributions can result in large macroscopic structures. These processes often elude a prediction from the properties of the individual constituents and are dependent on subtle changes in composition or environmental factors. As such, soft matter systems are highly tunable and responsive, which makes them so valuable for a wide range of technological applications.

Polymers represent a sub-group within soft matter. The term derives from the Greek words *poly* ("many") and *mer* ("part") and as such refers to molecules consisting of repeating elementary units, the *monomers*. Contrary to weakly associating self-assembled structures, the monomers of polymers are linked together via covalent bonds, which withstand breaking under normal circumstances. The number of monomers making up a polymer is called its *degree of polymerization N*. What is exactly meant by the term monomer is not well defined and can refer to anything that repeats along the polymer chain. For a chemist, this might be a group of atoms, such as an ethylene group $–CH_2–CH_2–$, which forms polyethylene upon *polymerization*, the process of linking monomers together. For a theoretical physicist attempting a more abstract description, on the other hand, a monomer might denote a segment of the polymer that shares some characteristics or a length scale that separates two distinct regimes, such as a Kuhn length or a blob.
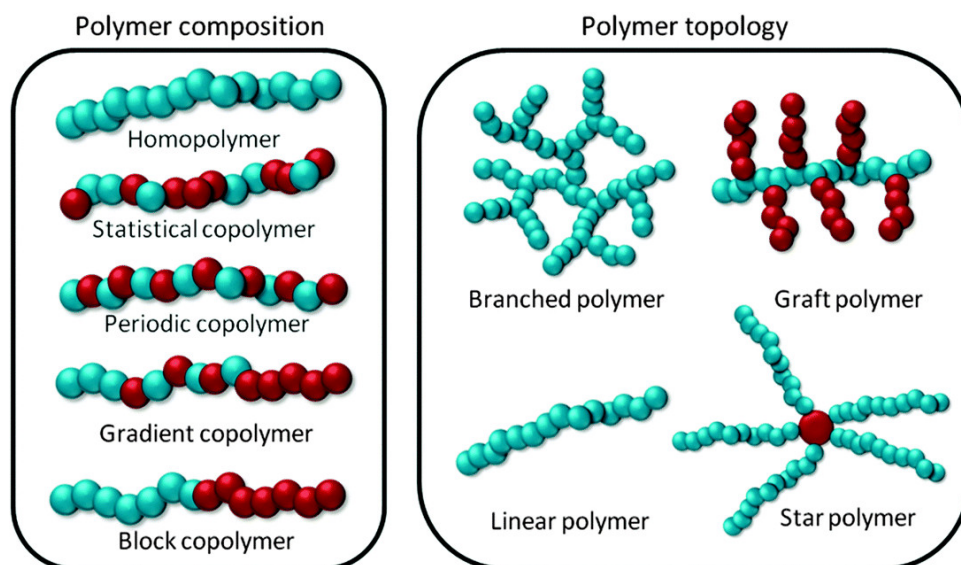
Figure 1.2: Schematic illustration of various possibilities of polymer compositions and topologies. Reproduced from [3] with permission of the Royal Society of Chemistry.

Polymers can be characterized by their composition, their architecture and their specific interactions or mechanical properties, illustrated in Figure 1.2. *Composition* refers to both the number of different monomer types present in a given polymer as well as their arrangement along the polymer contour. While *homopolymers* consist of only one repeating unit, *heteropolymers* contain two or more distinct monomers, which can be linked together in various patterns. In the case of two monomeric species, we can differentiate between *random*, *periodic*, *gradient* or *block* copolymers. *Architecture* or *Topology* describes the way branches or loops in the polymer backbone lead to a deviation from a linear chain. Examples include ring, star, comb / graft or ladder polymers and dendrimers. Recently, knotted polymers have received increased attention due to their importance in the un-

derstanding of DNA organization and transcription [4]. One of the motivations for this thesis is the question of which role the specific topology of a polymer plays in determining its structural and dynamical properties, a question that remains elusive to this day.

1.3 Single-Chain Nanoparticles

Promising Canditates for Technological Applications or a Model for Intrinsically Disordered Proteins?

Particularly sophisticated self-assembled structures can be found in nature in the form of chromatin, cell membranes, virus capsids and proteins. Advances in characterization techniques such as protein crystallization, X-ray scattering, NMR and fluorescent labeling and the subsequent explosion of known structures of biomolecules have led to the emergence of the central paradigm of biological materials: The structure-function relationship. The idea that the formation of a well-defined three dimensional shape completely determines the possible tasks a molecule can carry out has since revolutionized the field of drug design, but also inspired scientists and engineers in the field of nanotechnology to gain greater control over the size and shape of synthetic molecules. This goal has been achieved for a variety of hard nanoparticles, such as quantum dots, gold nanoclusters or metal oxide nanoparticles.

However, in the realm of soft materials, similar control proves elusive, precisely because of their distinguishing features, small size and weak interactions. Various methods have been proposed to harness their self-assembly behavior by tuning one or more of the following properties of their building blocks: the chemistry, the composition, or the architecture [5]. Prominent examples that have arisen from such efforts are micelle-forming amphiphiles [6] (chemistry), patchy particles such as DNA-coated colloids [7, 8] (composition) as well as dendrimers [9], star polymers [10] and nanogels [11] (architecture).

Mimicking nature's design of its most abundant molecular machines, proteins, a new approach to producing soft nano-objects was born in the beginning of the 21st century: *Single-chain technology* [12] aims to synthesize linear functionalized polymers which can collapse via purely intramolecular interactions to a precise shape, reminscent of the folding process of proteins [13]. Ideally, these *single-chain nanoparticles* (SCNPs) could be made from biocompatible polymers, respond to environmental triggers and be endowed
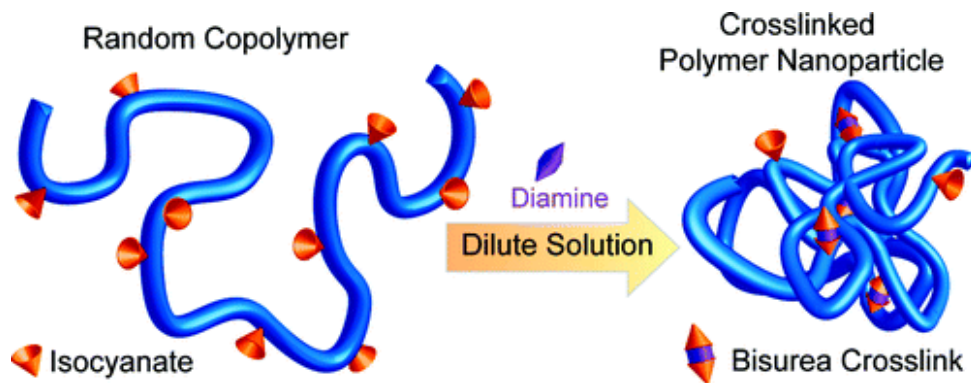
Figure 1.3: Schematic illustration of SCNP synthesis. A precursor molecule functionalized with reactive groups (here isocyanate) is cross-linked under highly dilute conditions via the addition of diamine to form a SCNP. Reproduced with permission of the American Chemical Society from [14].

with specific functions. As such, they represent a versatile addition to the library of nanoparticles with a vast range of potential applications from catalysis to nanomedicine.

Single-chain nanoparticles are soft nano-objects synthesized from a linear polymer precursor, which is functionalized with reactive groups capable of forming intramolecular bonds (see Figure 1.3). They are typically a few nanometers (≤ 20 nm) in size and possess a large surface-to-volume ratio. The necessary technological ingredients for their synthesis include controlled polymerization, monomer functionalization and cross-linking protocols that ensure their purely intramolecular collapse.

Precise control over the molecular weight, the polydispersity and the architecture of the precursor polymers has been achieved by several controlled/living polymerization techniques [15] including atom transfer radical polymerization (ATRP) [16], nitroxide mediated polymerization (NMP) [17], reversible addition-fragmentation chain transfer (RAFT) [18] and ring opening polymerization (ROP) [19].

Reactive units that can form bonds are introduced in the polymer either directly during the polymerization process or they are subsequently attached via postpolymerization modification reactions. The chemistry of the functional units is chosen based on efficiency, specificity and the absence of side products [20]. They are classified either by (i) the architecture of the bond or (ii) the type of interaction:

(i) Regarding the architecture of the bond, we can distinguish between cross-links formed by identical monomeric subunits in a pairwise manner (homocoupling), those formed by complementary functional groups (heterocoupling) and those mediated by external multifunctional cross-linkers.

(ii) Regarding the type of interaction, we can distinguish between covalent, dynamic covalent and non-covalent bonds. Especially interesting candidates for the synthesis of irreversible SCNPs is so-called "click" chemistry, due to its high efficiency, high functional group tolerance and mild reaction conditions [21]. A few examples currently in use in SCNP fabrication are copper-mediated azide-alkyne cycloaddition [22], thiol-ene couplings [23] and amine-isocyanate reactions [14]. On the other hand, non-covalent bonds such as hydrogen bonds [24, 25] and $\pi - \pi$ stacking [26], more closely model the folding process in biopolymers and are inherently reversible. Their gradual dependence on external variables such as temperature, pH and solvent conditions give the resulting SCNPs a higher tunability than their covalent counterparts. Finally, dynamic covalent bonds such as disulfide bridges [27] combine elements of both covalent and non-covalent bonds: Under normal conditions, they are kinetically trapped, but exchange reactions can be activated through external stimuli. As such, SCNPs formed via dynamic covalent bonds represent an interesting new class of highly adaptable and responsive nanoparticles. For an overview of the state-of-the art of SCNP synthesis, we would like to recommend the excellent review by Lyon *et al.* [28].

The cross-linking process is typically carried out in highly dilute conditions to avoid intermolecular bonds and thus aggregation. Novel synthesis protocols that take advantage of tunable solvent conditions or inert crowder molecules to improve control over the resulting structure of SCNPs have been recently proposed by computer simulations. Some of these will be discussed in Chapter 3.

Since single-chain technology is still in its infancy, reports on applications have been limited to proof-of-concept experiments thus far. Nonetheless, these demonstrate promising possibilities for the use of SCNPs in a broad range of applications, such as nanomedicine, catalysis, sensing and advanced materials.

SCNPs are especially interesting candidates for drug delivery by exploiting the enhanced permeability and retention (EPR) effect of tumor cells, that makes them accumulate more molecules in the nanometer range than healthy cells [29, 30]. Nanoparticles can encapsulate toxic, insoluble anti-cancer drug molecules and be functionalized with peptides or antibodies that target specific tumor tissues. Several biocompatible SCNPs have been synthesized whose non-toxicity in the absence of a drug was tested both *in vitro* and *in vivo* [31, 32, 33]. The successful release of small non-soluble bioactive cargos from a SCNP carrier upon a change in solvent conditions was also shown by several groups [34, 35, 36, 37]. Pioneering work by Hamilton and Harth [38] even reported the cellular uptake of peptides through the combination of SCNPs and dendritic transport molecules.

The EPR effect can furthermore be exploited by using specially functionalized SCNPs as image contrast agents in magnetic resonance imaging (MRI) or as gamma emitters for single photon emission computerized tomography (SPECT) [33]. For MRI, the results are particularly promising: SCNPs forming metal complexes with paramagnetic Gd^{3+} ions exhibit a strong increase in relaxivity values compared to traditional contrast agents, reflecting their effect on spin relaxation and thus creating a brighter contrast [39, 40]. A third imaging method that can potentially profit from single-chain technology is fluorescence imaging: The entrapment or conjugation of fluorophores [41, 42, 43, 44, 45] and quantum dots [46] can lead to both reduced photobleaching [32] and enhanced photoemission [40].

SCNPs exhibit key characteristics that make them well suited for use as enzyme-mimetic catalysts: Their two limiting topologies, sparse ones containing multiple compact domains or globular ones with a single large pocket (as can be achieved with amphiphilic precursors) can be exploited as cavities for the incorporation of insoluble catalysts. Their large surface-to-volume ratio further facilitates the diffusion of reagents and products to and out of these catalytic sites. Improvements in efficiency or product size control via the use of single-chain nanoparticles as nanoreactors have been achieved for the synthesis of small chemical compounds [47, 48, 49, 50, 51, 52, 53, 54, 55], polymers [56, 57], gold nanoparticles [58], quantum dots [46] and carbon nanodots [59].

Two particularly sophisticated SCNP systems have been developed for sensing applications: Polynorbone polymers grafted with bipyridine units can reversibly fold via $\pi - \pi$ interactions to fluorescent SCNPs. The strong affinity of pyridin for certain metal ions leads to fluorescence quenching as the $\pi - \pi$ interactions are replaced by metal complexes [41]. Catalytic and sensing properties were successfully combined in another pyridine-functionalized SCNP with the ability to catalyse the reduction of $NaAuCl_4$ by hydrazine to form gold nanoparticles. Under normal conditions, the steric constraints of the SCNPs' catalytic pockets stabilizes gold nanoparticles about ∼8 nm in size. In the presence of zein protein, however, pyridin binds to zein residues, leading to the partial unfolding of the SCNP and the growth of larger gold nanoparticles (∼100 nm). The concentration of zein protein determines the color of the resulting solution, allowing zein detection in the range of 12 to 3000 μg/ml [60].

Furthermore, SCNPs have been proposed as additives to tune the properties of a variety of soft materials. The good size control over SCNPs in the nanometer range lends itself to the templating of porosity in thin films for microelectronic applications

[13, 61, 62]. The reduced viscosity of SCNPs with respect to their linear precursors owning to their decreased hydrodynamic radius [63] renders them useful as rheology modifiers in melts of thermoplastics [64], elastomeric polymers [65] and nanocomposites [66, 67, 68]. Particularly promising is the case of all-polymer nanocomposites, where SCNPs provide an efficient pathway to arrest phase separation in homogeneous binary polymer blends [69] and can induce disentanglement of PEO chain motions [70, 71, 72]. Furthermore, phase diagrams of such nanocomposites including purely entropic effects [73, 74], but also weak interactions[75], free volume effects [76] and small ionic charges [77] were predicted theoretically and allow the determination of a critical nanoparticle size as a limit for miscibility [78].

1.4 Polymer Physics and the Importance of Being a Fractal

Since this thesis focuses on computational investigations of simplified polymers, we would like to briefly introduce the reader to the fundamental concepts required to understand the theoretical description of this special class of molecules. For a more detailed introduction to polymer physics, we refer the interested reader to the classic textbook *Polymer Physics* by Rubinstein and Colby [79].

As we will see throughout this thesis, theoretical or computational investigations of polymers often lead to the discovery of *scaling laws*, which means that a particular quantity y depends in a power-law manner on another, i.e. $y(x) \sim x^\nu$. This ubiquitous behavior of a variety polymer properties can be attributed to their self-similarity: Polymers are fractals. To put it in Benoit Mandelbrot's words, who coined the term: *"A fractal is a shape made of parts similar to the whole in some way."*. Fractals can be constructed regularly through iteration of a set of rules or stochastically. A quick look around reveals an astonishing number of fractals encountered in nature: snow flakes, leafs, blood vessels, trees, coastlines and clouds all exhibit self-similar patterns on some length scales.

An example of a regular fractal is the Sierpinski triangle shown in Figure 1.4. To create it, start with a filled equilateral triangle. Now divide it equally into four parts and remove the middle one. This represents the first iteration, which is then repeated for each of the three remaining filled triangles. Three become nine triangles, which then turn into

Figure 1.4: Evolution of the Sierpinsky triangle in five iterations. Reproduced with minor changes from [80].

27 and so on. We can now ask how the area A of the Sierpinsky triangle changes when we increase its side length. Since it is a fractal, we expect a power law

$$A = \alpha l^{\mathcal{D}}\,. \tag{1.1}$$

We call $\mathcal{D}$ its fractal dimension. To calculate it, have a look at the second iteration in Figure 1.4. Let l_1 be the side-length of a sub-triangle and A_1 its area. If we double the side-length of the whole Sierpinsky triangle, $l_2 = 2l_1$, we end up with three sub-triangles. Using equation 1.1, it follows that

$$A_2 = \alpha l_2^{\mathcal{D}} = \alpha (2l_1)^{\mathcal{D}}\,, \tag{1.2}$$

$$A_2 = 3A_1 = 3\alpha l_1^{\mathcal{D}}\,. \tag{1.3}$$

This set of equations can easily be solved and we arrive at

$$\mathcal{D} = \frac{\log 3}{\log 2} \cong 1.58\,. \tag{1.4}$$

Polymers are obviously not regular structures such as a Sierpinsky triangle. Their large number of degrees of freedom allows them to adopt a plethora of conformations. Nonetheless, the averages over all possible conformations behave in a fractal manner. This is both true for the size of the whole polymer as a function of its degree of polymerization, $\langle R^2 \rangle \sim N^{2\nu}$, but also for any subsection of the chain.

1.4.1   The fractal nature of ideal chains

To illustrate this behavior, let us briefly derive the average end-to-end vector of an ideal, completely flexible linear polymer, consisting of $N = n+1$ monomers, linked together by n backbone bonds. We call a polymer *ideal* if we can neglect any net interactions between monomers i and j which are separated by a sufficient number of bonds. The end-to-end vector is given by the sum over all n bond vectors $\boldsymbol{b}_i = \boldsymbol{r}_i - \boldsymbol{r}_{i-1}$ in the chain:

$$\boldsymbol{R} = \sum_{i=1}^{n} \boldsymbol{b}_i\,. \tag{1.5}$$

Over time, an ensemble of polymer chains will sample all possible configurations and since there are no energetic differences between bond vectors of different orientations, the average end-to-end vector will be zero. However, the mean-square end-to-end distance will be non-zero:

$$\langle R^2 \rangle \equiv \langle \boldsymbol{R} \cdot \boldsymbol{R} \rangle = \left\langle \left(\sum_{i=1}^{n} \boldsymbol{b}_i \right) \cdot \left(\sum_{j=1}^{n} \boldsymbol{b}_j \right) \right\rangle = \sum_{i=1}^{n} \sum_{j=1}^{n} \langle \boldsymbol{b}_i \cdot \boldsymbol{b}_j \rangle . \tag{1.6}$$

Assuming all bond vectors have the same length l, the scalar product between bond vectors $\boldsymbol{b}_i$ and $\boldsymbol{b}_j$ only depends on the bond angle θ_{ij}, such that

$$\langle R^2 \rangle = l^2 \sum_{i=1}^{n} \sum_{j=1}^{n} \langle \cos \theta_{ij} \rangle . \tag{1.7}$$

The average $\langle \cos \theta_{ij} \rangle$ depends on the stiffness of the polymer and the specific polymer model. The simplest model is the *freely-jointed chain model*, that assumes no correlations between bond vectors, such that $\langle \cos \theta_{ij} \rangle = 0$ for $i \neq j$. From this, it follows that

$$\langle R^2 \rangle = nl^2 . \tag{1.8}$$

Models of semi-flexible and stiff polymers, the *freely rotating chain model* and the *worm-like chain model*, treat the bond angle as non-zero but fixed, while the torsion angle is unconstrained. Therefore, the correlation between bond vectors reduces to

$$\langle \boldsymbol{b}_i \cdot \boldsymbol{b}_j \rangle = l^2 \langle \cos \theta \rangle^{|j-i|} = e^{-|j-i|/\ln(\cos \theta)} , \tag{1.9}$$

which is a rapidly decaying function of $|j-i|$, such that the sum

$$\langle R^2 \rangle = l^2 \sum_{i=1}^{N} \sum_{j=1}^{N} \langle \cos \theta_{ij} \rangle = l^2 \sum_{i=1}^{N} C_i' = C_n nl^2 , \tag{1.10}$$

exists and can be calculated analytically for these two models. In the limit of large polymerization degree, it can be shown that $\lim_{n \to \infty} C_n = C_\infty$ is a finite number if $\langle \cos \theta_{i,i+k} \rangle$ decays more rapidly than k^{-1} [81]. The different ideal chain models thus only differ in their values of C_∞, called *Flory's characteristic ratio*, but not in their scaling with the polymerization degree $N = n + 1$. The specific values of C_n for real polymers depend on their chemistry, especially the bulkiness of their side groups that lead to steric hindrances. This result allows us to map any polymer that follows the ideal chain scaling $\langle R^2 \rangle \sim n$ to an equivalent freely jointed chain with the same mean-square end-to-end distance and the same maximum end-to-end distance. This equivalent freely jointed chain will have a reduced number of effective monomers $N_b + 1$ (*Kuhn monomers*) and an increased effective bond length b (*Kuhn length*), since

$$R_{\text{max}} = N_b b , \tag{1.11}$$

and

$$\langle R^2 \rangle = N_b b^2 = b R_{\max} = C_n n l^2 \,. \tag{1.12}$$

In the following, we would like to give an example of how the self-similarity of polymers can provide scaling arguments to extract the essential physics of a problem. Imagine an ideal chain being stretched to a particular elongation R_x. If this extension is small compared to the maximum extension possible $R_x \ll R_{\max} = Nb$, we can assume that the local conformations are essentially unperturbed by the stretch and follow the random walk statistics as they maximize entropy. Thus, up to some chain segment of size ξ, the g monomers within this segment follow the scaling we found for ideal chains,

$$\xi^2 \approx b^2 g \,. \tag{1.13}$$

In order to add up to a total extension of R_x, these N/g random-walk chain segments have to be arranged sequentially in the direction of extension, such that

$$R_x \approx \xi \frac{N}{g} \approx \frac{Nb^2}{\xi} \,. \tag{1.14}$$

This equation determines the number of so called *tension blobs* and their size. It represents the physical length scale below which the chain behaves ideal and above which it experiences the deformation. The conformations of the polymer are only changed with respect to a random walk on length scales greater than the blob size. Each tension blob, however, is forced to go in a particular direction along the direction of the stretch, such that the chain looses one degree of freedom per tension blob. According to the equipartition theorem, this translates to a free energy change of one $k_B T$ per tension blob due to the stretching of the chain:

$$F \approx k_B T \frac{N}{g} \approx k_B T \frac{R_x^2}{Nb^2} \,. \tag{1.15}$$

1.4.2 The fractal nature of real chains

We have seen that the statistics of ideal chains can be derived from the assumptions that correlations between monomers along the backbone of the chain decay fast and thus monomers separated by large contour distances behave essentially independent of each other. This assumption is true in some situations, but in most conditions, monomers experience either an attraction or a repulsion between one another. The effect of the energetic cost of bringing two monomers in close proximity can be parametrized by their *excluded volume* v, which is defined as

$$v = - \int_{\mathbb{R}^3} \left(1 - e^{-U(r)/k_B T} \right) \mathrm{d}^3 r \,, \tag{1.16}$$

where $U(r)$ is the total potential energy between two monomers. As such, v represents an effective net interaction between monomers. The value of v depends strongly on the surrounding environment, especially, solvent type, temperature and density. Typically, we classify them as follows:

1. *Athermal solvents* are those in which the potential energy only has a repulsive contribution and becomes independent of temperature. In this case the excluded volume is simply given by the volume occupied by a spherical monomer with diameter $d = b$ or a cylindrical Kuhn monomer with length b and diameter d:

$$v \approx b^2 d. \tag{1.17}$$

2. *Good solvents*, as the name suggests, are characterized by the chain readily dissolving and swelling in the solvent. The effective repulsion between monomers stems from the domination of the repulsive part of the potential over the small attractive well in $U(r)$, which is modulated by temperature.

$$0 < v < b^2 d \tag{1.18}$$

3. *Theta solvents* are defined by the repulsive and attractive forces exactly balancing each other, such that $v = 0$ and the chain behaves nearly ideal. This can happen at the characteristic θ-*temperature* of the solvent or in the melt state, where the whole volume is occupied by monomers.

4. *Poor solvents* repel the polymers, leading to an effective net attraction between monomers and the collapse of the chain. They are characterized by a negative excluded volume

$$-b^2 d < v < 0 \tag{1.19}$$

How does the excluded volume of a chain in good solvent conditions affect its conformational statistics? Flory theory estimates the free energy of the polymer as a balance between the repulsion energy between monomers and the entropic loss due to the conformational changes. In a good solvent with $v > 0$, the polymer will be swollen with respect to an ideal chain $R > R_{\text{ideal}} = bN^{1/2}$. If we assume a homogeneous distribution of monomers within the pervaded volume R^3, the probability of a monomer occupying the excluded volume of another is given by the ratio of excluded volume v to volume accessible to a monomer $p_v = \frac{v}{(R^3/N)}$. The energetic cost associated with the exclusion

of a monomer is $k_B T$, such that it amounts to $k_B T p_v$ per monomer. Thus, the energetic contribution to the free energy is

$$F_{\text{excl}} \approx k_B T v \frac{N^2}{R^3} \, . \tag{1.20}$$

The entropic contribution can be estimated by the free energy of stretching an ideal chain to an end-to-end distance R we derived earlier in Section 1.4.1 (Equation 1.15). The total free energy then amounts to the sum of the energetic and entropic terms

$$F = F_{\text{excl}} + F_{\text{ent}} \approx k_B T \left(v \frac{N^2}{R^3} + \frac{R^2}{Nb^2} \right) \, . \tag{1.21}$$

Minimizing the free energy with respect to the size R of the chain, yields

$$\frac{\partial F}{\partial R} = k_B T \left(-3v \frac{N^2}{R_{\text{F}}^4} + 2 \frac{R_{\text{F}}}{Nb^2} \right) \overset{!}{=} 0 \tag{1.22}$$

$$R_{\text{F}} \approx v^{1/5} b^{2/5} N^{3/5} \, . \tag{1.23}$$

The simple estimation $R \sim N^\nu$ with the *Flory exponent* $\nu = 3/5 = 0.6$ is in good agreement with both experimental data and computational studies of *self-avoiding walks* on lattices, which are random walks that never visit an already visited site again. What is puzzling is that the theory works so well even though it relies on two erroneous assumptions. For one, it overestimates the energetic contribution, because it neglects correlations between monomers. Furthermore, the conformational entropy is assumed to be the same as for an ideal chain. However, conformations of real and ideal chains differ qualitatively, as the scaling $R \sim N^\nu$ (with $\nu > 0.5$ as in the ideal case) also holds for segments of the chain because of the polymer's self-similarity. More sophisticated theories predict a scaling exponent of $\nu \cong 0.588$, which in most experiments (and also computer simulations) is indistinguishable from the exponent $\nu_{\text{F}} = 3/5 = 0.6$.

The fractal dimension $\mathcal{D} = 1/\nu$ of a polymer is important in deriving predictions about its physical properties that rely on its intramolecular conformations. But how do we extract it? By means of scattering experiments at high dilution (which will be discussed in a bit more detail in the next section), we can determine the form factor of a polymer

$$w(\mathbf{q}) = \frac{1}{N} \sum_{j,k} e^{i\mathbf{q} \cdot (\mathbf{r}_j - \mathbf{r}_k)} = \frac{1}{N} \left[1 + \int g(r) e^{i\boldsymbol{q} \cdot \boldsymbol{r}} \right] , \tag{1.24}$$

It can be expressed as the Fourier transform of the pair correlation function $g(r)$, which is the probability of finding another monomer at a distance r from any given monomer with respect to a homogeneous distribution. If the polymer is a fractal, such that $r \sim n^\nu$, or equivalently, $n \sim r^{\mathcal{D}}$, holds for intermediate length scales $b < r < R_{\text{g}}$, we can approximate

the pair correlation function in this regime as the ratio between monomers found within the volume r^3 and the monomers that would be found within this volume in a homogeneous distribution

$$g(r) \approx \frac{n_{\text{fractal}}}{n_{\text{hom}}} \sim \frac{r^{\mathcal{D}}}{r^3} \sim r^{\mathcal{D}-3} . \tag{1.25}$$

With this approximation, Equation 1.24 can be solved exactly and we find that the form factor scales with the fractal dimension $\mathcal{D}$ in what is called the *fractal regime* $R_{\text{g}}^{-1} \lesssim q \lesssim b^{-1}$ as

$$w(q) \sim \left(q\sqrt{\langle R_{\text{g}}^2 \rangle} \right)^{-\mathcal{D}} . \tag{1.26}$$

1.5 Experimental Charaterization of SCNPs

Putting the cartoon to the test

While the collapse of a linear precursor to a globular nanoparticle via the cross-linking of reactive groups might seem conceptually simple, as scientists we have to ask how close this simple picture (as illustrated in Figure 1.3) comes to the truth. Do the functional reactive groups efficiently form purely intermolecular cross-links? How does the size of the synthesized SCNPs decrease with respect to the precursors? What intramolecular structure do SCNPs adopt? Are they the soft, globular nano-objects we imagine? Fortunately, a variety of techniques are at the physicist's and chemist's disposal to answer just these questions. In case we find discrepancies between our anticipated outcome and the experimental measurements, we can combine the results with computer simulations and theoretical models to understand the underlying molecular mechanisms. In the following we will give a short review of the most common techniques employed to characterize SCNPs and the insights gained from them.

The first step in SCNP characterization is ensuring that the cross-linking reaction has successfully completed. Nuclear magnetic resonance (NMR) acts on atomic nuclei with an intrinsic nuclear magnetic moment called a spin (such as ^{1}H, ^{13}C, or ^{15}N), which orients in a strong external magnetic field. Upon application of a short transversal magnetic pulse with a specific resonance frequency, the spin can flip, entering a higher energy state, and relax back to its ground state with a characteristic relaxation time. The resonance frequency of the nucleus depends on its local environment, a feature which can be exploited to monitor the chemical modification of the SCNP precursor through the formation of bonds. These chemical changes become visible as chemical shifts in the NMR spectra

during the synthesis [58, 47]. Furthermore, NMR can determine the mobility of chain segments through the spin-spin relaxation time. As such, increasing amounts of cross-links present have been shown to correlate with reduced molecular mobility within the molecule in SCNPs that form coumarin dimers upon photoactivation [82, 53].

After the synthesis is completed, we need to probe the production of true *single*-chain nanoparticles (i.e. the absence of intermolecular aggregates) and the collapse of the chain with respect to the precursor. In size exclusion chromatography (SEC) [83], a type of liquid chromatography, a sample solution is forced through a column containing tightly packed porous particles, typically porous silica spheres. The relation of the pore size to the sample size determines the ability of the sample molecules to penetrate the pores [84]. The smaller the molecules, the easier it is for them to enter the pores, which results in a longer retention time and qualitative separation of molecules according to their hydrodynamic radius R_h [85]. Therefore, SEC can also verify that no aggregation has taken place during the cross-linking process and possible aggregates of two or more chains can be isolated. SEC is routinely combined with other characterization techniques such as dynamic light scattering (DLS) [86, 87] or multi-angle light scattering (MALS) [27]. In DLS, temporal fluctuations of scattered light due to constructive and destructive interference are measured, which stem from the translational diffusion D of the particle. Assuming Brownian motion and spherical shapes, the hydrodynamic radius can be determined through the Stokes-Einstein relation $D = \frac{k_B T}{6\pi\eta R_\mathrm{h}}$, where η denotes the viscosity. In MALS, the scattered light is statically measured at many angles to determine the angular dependency of the scattered intensity, which can thus yield quantitative measurements of the molecular weight via an extrapolation to 0°.

A compilation of literature results utilizing size-exclusion chromatography (SEC) and dynamic light scattering (DLS) to determine the hydrodynamic radii of SCNPs and their respective precursors was presented in Ref. [88]. It found that the data can be well described by a simple scaling law $R_H^\mathrm{SCNP} = k(R_H^\mathrm{precursor})^{\nu/\nu_F}$, where $\nu_F = 0.59$ is the Flory exponent and $\nu = 0.48$. As explained in Section 1.4, the significantly reduced exponent $\nu < \nu_F$ reveals that the resulting SCNP adopt more compact conformations than their precursors, which exhibit self-avoiding behavior in good solvent conditions. However, it is far from the limit expected for dense spherical objects, $\nu = 1/3$.

Deeper insights into the intramolecular structure of polymers can be obtained by scattering experiments. During such experiments, an incident beam of particles (most commonly photons or neutrons) interacts with the sample, and is thus deflected with an

angle θ. Individual probe particles exchange momentum with different atoms within the sample and their individual paths create interference. As such, the scattered intensity in a particular direction, characterized by the wavevector $\boldsymbol{q} = \frac{4\pi n}{\lambda} \sin\left(\frac{\theta}{2}\right)$, depends on the distances $\boldsymbol{R}_j - \boldsymbol{R}_i$ between atoms in the sample,

$$I(\boldsymbol{q}) \sim \sum_{i,j} e^{\boldsymbol{q}\cdot(\boldsymbol{R}_j - \boldsymbol{R}_i)} . \tag{1.27}$$

Thus, small wavevectors probe the distributions of atoms at large length scales and big wavevectors can resolve atomic fluctuations. Since it depends on the wavelength λ of the incident beam, high energy sources such as X-rays or neutrons can resolve structural details on the chain segment level, while low energy sources such as DLS can only determine the average dimensions of a polymer.

Experimental investigations by small-angle neutron scattering (SANS) and small-angle X-ray scattering (SAXS) have been carried out for SCNPs obtained through Michael addition (Mi-SCNPs) and Cu-complexation (Cu-SCNPs) [34, 89]. In high dilution, scattering is solely determined by the form factors of the molecules. They were found to scale as $w(q) \sim q^{-1/\nu}$ with exponents $\nu \approx 0.45$ and $\nu \approx 0.55$ for Mi-SCNPs and Cu-SCNPs, respectively. The average internal structure elucidated in this way is consistent with the scaling of the hydrodynamic radii determined by SEC and DLS.

The fractal dimension $\nu \approx 0.5$ found consistently via a range of different methods across different polymer and bond chemistries has finally led to a sobering realization: The image of a neatly folded globular nanoparticle must be further from the truth than pioneers in the field of single-chain technology had hoped for. While $\nu \approx 0.5$ represents a collapse relative to the polymer precursor, which adopts self-avoiding conformations characterized by the Flory exponent ν_F in good solvent conditions, it is far from homogeneous spheres ($\nu = 1/3$) or the ordered native folded state of proteins ($\nu \approx 0.29$, close to the exponent $1/4$ expected for the form factor of dense impenetrable spheres that originates from surface Porod scattering) [90].

Interestingly, however, the apparent scaling exponent of SCNPs constitutes a remarkable similarity with intrinsically disordered proteins, whose intramolecular structure also leads to $\nu \approx 0.5$ [91, 92, 93, 94]. Their most distinctive feature, to which they owe their denomination, is their refusal to crystallize. Thus they elude structural characterization via biology's power house technology of the 20th century, X-ray crystallography. As a consequence, they have puzzled biologists for a long time and called into question the structure-function paradigm. Fortunately, advances in NMR technology and clever experimental designs have made it possible to uncover the structural details of some IDPs,

although the library of determined protein structures is still strongly dominated by crystallizable globular proteins.

What was found is that the term 'disordered' was unjustified: While lacking a static, well-defined 3D structures, except for some rare exceptions all IDPs do show some degree of secondary structure (α-helices and β-sheets) and the presence of compact folded domains. In contrast to globular proteins, however, their ordered domains are separated by flexible segments lacking in secondary structure [95, 96, 97]. This gives them the ability to respond quickly to environmental changes and bind to a variety of cellular targets. Furthermore, as a consequence of their malleability, interactions with inert crowding molecules or specific interactions with target molecules can substantially affect their dynamic and associative properties [98, 99, 100].

1.6   Computer Simulations of SCNPs

Unraveling the molecular origin of the sparse topologies

Does the apparent structural similarity between IDPs and SCNPs suggested by the similar fractal dimension $\mathcal{D} = 1/\nu$ manifest itself in the conformational ensembles of SCNPs? How far do their similarities extend and can insights about the structure and dynamics of SCNPs in complex environments, which are not easily probed for IDPs, serve as simple models for general behaviors of IDPs as well? The experimental techniques discussed so far cannot answer these questions. The random cross-linking of the SCNP precursor results in an intrinsical structural polydispersity with a distribution of different topologies. Experiments working with solutions containing such a variety of different SCNPs necessarily produce average values of any investigated characteristic. This is were computer simulations come into play.

In molecular dynamics simulations, the motion of molecules can be followed directly as they evolve with time according to Newton's equations of motion. Any quantity of interest can then be calculated directly from the ensemble of positions and velocities generated during the course of the simulation. The level of detail captured depends on the model used and ranges from atomistic to mesoscopic (i.e. chain segments) for the relevant models in polymer physics. In the field of single-chain nanoparticles, first computer simulations were performed in 2008 of a united-atom model for polystyrene precursors [101] with

randomly placed benzocyclobutene groups [102, 103, 104]. Preliminary investigations into semiflexible and flexible bead-spring models for SCNPs were carried out as well. The simulations revealed that synthesis in good solvent conditions results in SCNPs of sparse conformations rather than compact structures.

The value of computer simulations for the understanding of the molecular mechanism underlying the formation of sparse structures in SCNPs has been shown by Moreno *et al.* in Ref. [105]. Employing a coarse-grained bead-spring model that does not account for the specific chemistry of the polymer backbone or the functional groups, but retains the essential ingredients of polymer physics, monomer excluded volume and chain connectivity, the authors explored a broad range of polymerization degrees N and fractions of reactive groups $f = N_r/N$. They were able to show that data from different parameters for the average squared radius of gyration R collapse onto a master curve following the scaling $\langle R_g^2 \rangle / b^2 = N^{2\nu}$. The number of cross-links only affected the effective segment length b. The study was followed by a subsequent paper [106] analysing the structure via the calculation of the intramolecular form factors, $w(q) \sim q^{-1/\nu}$. In both cases, the scaling exponent found $\nu \approx 0.5$ was significantly reduced with respect to the self-avoiding Flory exponent of $\nu_F = 0.59$.

The advantage of molecular dynamics simulations lies in the fact that apart from calculating ensemble averages, it allows for a visual inspection and characterization of individual molecules. With their help, the underlying physical mechanism for the prevalence of sparse topologies could be elucidated: The self-avoiding conformations adopted by the precursors under good solvent conditions promote the formation of cross-links between reactive monomers separated by short contour distances. Long-range loops, which are necessary for global compaction, on the other hand, occur very infrequently as they require large reorientations of the precursor chain to bring far apart monomers into close proximity, allowing them to cross-link.

And what about the similarities between SCNPs and intrinsically disordered proteins (IDPs)? In Ref. [106], individual SCNPs were characterized according to their 'domains', defined as clusters of loops formed during the synthesis procedure. A broad distribution of domain sizes was found, along with a correlation between an SCNP's shape, the size of its biggest domain and its relative deformability. The presence of locally compact domains separated by flexible linker segments supports the analogy between IDPs and SCNPs and could make the latter a viable model for studying general (non-specific) responses of the former in complex environments, such as steric crowding and shear flow.

Indeed, investigations by computer simulations complemented by X-ray and neutron scattering experiments of SCNPs in the presence of inert crowders, revealed an interesting collapse behavior to crumpled globular structures, a striking difference with respect to linear polymers [106, 107].

1.7 Aim and Organization

The general aim of this thesis is to deepen our understanding of the structural and dynamical properties of single-chain nanoparticles in poorly understood or even unexplored complex environments: crowding conditions and shear flows. Computer simulations are employed as a tool to calculate observables that can either not be accessed through experiments or are indirectly obtained from them on the basis of approximations or model assumptions. Furthermore, the possibility of investigating single SCNPs with a specific topology instead of the averages of a polydisperse mixture produced by experiments allows us to pose the fundamental question of the role of polymer topology in the resulting structure and dynamics.

One of the main objectives of single-chain technology today is to envision and successfully implement new synthesis methods that circumvent the production of sparse topologies (as in the standard synthesis protocol at high dilution) and instead reliably lead to globular nanoparticles. We propose a novel synthesis protocol based on a change in precursor architecture and performing the cross-linking procedure under crowding conditions.

The high number of degrees of freedom present in polymers lead to complex dynamic behaviors under flow conditions that substantially depend on topology. The topologically polydisperse character of SCNPs might lead to non-trivial responses under shear that stem from the presence of various underlying dynamics at different time scales in SCNP mixtures. To elucidate the role of SCNP topology under homogeneous shear flow, we perform hybrid molecular dynamics simulations including hydrodynamic interaction of various single SCNPs. We complement these with simulations of polydisperse and monodisperse mixtures in the semi-dilute regime.

In recent years, reversible SCNPs have gained increased attention due to their greater responsiveness to external stimuli. However, theoretical investigations into the interplay between intramolecular and intermolecular bonds, which are bound to occur in semi-dilute

solutions, are lacking at this point. Here, we aim to provide a preliminary investigation into the potential for gel formation in systems of reversible SCNPs that mimic reversible covalent bonds.

The thesis is organized as follows. In Chapter 2, we introduce the polymer model and the associated potentials and constraints used in this work. Furthermore, we explain the theoretical background and the implementation of the employed simulation methods, Molecular Dynamics, Langevin Dynamics and Multi-particle Collision Dynamics. Chapter 3 proposes a novel synthesis protocol based on a change from linear to ring polymer precursors and performing the cross-linking procedure under crowding conditions. In Chapter 4, we present extensive computational investigations of the structural and dynamical response of SCNPs to homogeneous shear flows, at the single-molecule level and in the semi-dilute regime. Chapter 5 reports the gel formation in reversibly cross-linking polymers. Finally, we summarize the results and end with our conclusions and outlooks for the future of single-chain technology.

References

[1] I. W. Hamley, *Introduction to soft matter: synthetic and biological self-assembling materials.* John Wiley & Sons, 2013.

[2] P. R. Wich. `https://www.wichlab.com/research/`. Accessed on 31/10/2019.

[3] A. C. Rinkenauer, S. Schubert, A. Traeger, and U. S. Schubert, "The influence of polymer architecture on in vitro pdna transfection," *J. Mater. Chem. B*, vol. 3, pp. 7477–7493, 2015.

[4] J. Dorier and A. Stasiak, "Topological origins of chromosomal territories," *Nucleic Acids Research*, vol. 37, pp. 6316–6322, 09 2009.

[5] J. Callejas-Fernández, J. Estelrich, M. Quesada-Pérez, and J. Forcada, *Soft nanoparticles for biomedical applications.* Royal Society of Chemistry, 2014.

[6] V. P. Torchilin, "Micellar nanocarriers: pharmaceutical perspectives," *Pharmaceutical research*, vol. 24, no. 1, p. 1, 2007.

[7] L. Di Michele and E. Eiser, "Developments in understanding and controlling self assembly of dna-functionalized colloids," *Physical Chemistry Chemical Physics*, vol. 15, no. 9, pp. 3115–3129, 2013.

[8] M. R. Jones, N. C. Seeman, and C. A. Mirkin, "Programmable materials and the nature of the dna bond," *Science*, vol. 347, no. 6224, p. 1260901, 2015.

[9] d. A. Bosman, H. Janssen, and E. Meijer, "About dendrimers: structure, physical properties, and applications," *Chemical reviews*, vol. 99, no. 7, pp. 1665–1688, 1999.

[10] H. Gao, "Development of star polymers as unimolecular containers for nanomaterials," *Macromolecular Rapid Communications*, vol. 33, no. 9, pp. 722–734, 2012.

[11] J. K. Oh, R. Drumright, D. J. Siegwart, and K. Matyjaszewski, "The development of microgels/nanogels for drug delivery applications," *Progress in Polymer Science*, vol. 33, no. 4, pp. 448–477, 2008.

[12] M. Gonzalez-Burgos, A. Latorre-Sanchez, and J. A. Pomposo, "Advances in single chain technology," *Chemical Society Reviews*, vol. 44, no. 17, pp. 6122–6142, 2015.

[13] D. Mecerreyes, V. Lee, C. J. Hawker, J. L. Hedrick, A. Wursch, W. Volksen, T. Magbitang, E. Huang, and R. D. Miller, "A novel approach to functionalized nanoparticles: self-crosslinking of macromolecules in ultradilute solution," *Advanced Materials*, vol. 13, no. 3, pp. 204–208, 2001.

[14] J. B. Beck, K. L. Killops, T. Kang, K. Sivanandan, A. Bayles, M. E. Mackay, K. L. Wooley, and C. J. Hawker, "Facile preparation of nanoparticles by intramolecular cross-linking of isocyanate functionalized copolymers," *Macromolecules*, vol. 42, no. 15, pp. 5629–5635, 2009.

[15] W. A. Braunecker and K. Matyjaszewski, "Controlled/living radical polymerization: Features, developments, and perspectives," *Progress in polymer science*, vol. 32, no. 1, pp. 93–146, 2007.

[16] K. Matyjaszewski and J. Xia, "Atom transfer radical polymerization," *Chemical reviews*, vol. 101, no. 9, pp. 2921–2990, 2001.

[17] C. J. Hawker, A. W. Bosman, and E. Harth, "New polymer synthesis by nitroxide mediated living radical polymerizations," *Chemical reviews*, vol. 101, no. 12, pp. 3661–3688, 2001.

[18] J. Chiefari, Y. Chong, F. Ercole, J. Krstina, J. Jeffery, T. P. Le, R. T. Mayadunne, G. F. Meijs, C. L. Moad, G. Moad, *et al.*, "Living free-radical polymerization by reversible addition- fragmentation chain transfer: the raft process," *Macromolecules*, vol. 31, no. 16, pp. 5559–5562, 1998.

[19] N. E. Kamber, W. Jeong, R. M. Waymouth, R. C. Pratt, B. G. Lohmeijer, and J. L. Hedrick, "Organocatalytic ring-opening polymerization," *Chemical reviews*, vol. 107, no. 12, pp. 5813–5840, 2007.

[20] M. A. Gauthier, M. I. Gibson, and H.-A. Klok, "Synthesis of functional polymers by post-polymerization modification," *Angewandte Chemie International Edition*, vol. 48, no. 1, pp. 48–58, 2009.

[21] A. Sanchez-Sanchez, I. Pérez-Baena, and J. A. Pomposo, "Advances in click chemistry for single-chain nanoparticle construction," *Molecules*, vol. 18, no. 3, pp. 3339–3355, 2013.

[22] A. Ruiz de Luzuriaga, N. Ormategui, H. J. Grande, I. Odriozola, J. A. Pomposo, and I. Loinaz, "Intramolecular click cycloaddition: an efficient room-temperature route towards bioconjugable polymeric nanoparticles," *Macromolecular Rapid Communications*, vol. 29, no. 12-13, pp. 1156–1160, 2008.

[23] D. Chao, X. Jia, B. Tuten, C. Wang, and E. B. Berda, "Controlled folding of a novel electroactive polyolefin via multiple sequential orthogonal intra-chain interactions," *Chem. Commun.*, vol. 49, pp. 4178–4180, 2013.

[24] M. Seo, B. J. Beck, J. M. Paulusse, C. J. Hawker, and S. Y. Kim, "Polymeric nanoparticles via noncovalent cross-linking of linear chains," *Macromolecules*, vol. 41, no. 17, pp. 6413–6418, 2008.

[25] E. J. Foster, E. B. Berda, and E. Meijer, "Metastable supramolecular polymer nanoparticles via intramolecular collapse of single polymer chains," *Journal of the American Chemical Society*, vol. 131, no. 20, pp. 6964–6966, 2009.

[26] S. Burattini, H. M. Colquhoun, J. D. Fox, D. Friedmann, B. W. Greenland, P. J. Harris, W. Hayes, M. E. Mackay, and S. J. Rowan, "A self-repairing, supramolecular polymer system: healability as a consequence of donor–acceptor π–π stacking interactions," *Chemical communications*, no. 44, pp. 6717–6719, 2009.

[27] B. T. Tuten, D. Chao, C. K. Lyon, and E. B. Berda, "Single-chain polymer nanoparticles via reversible disulfide bridges," *Polymer Chemistry*, vol. 3, no. 11, pp. 3068–3071, 2012.

[28] C. K. Lyon, A. Prasher, A. M. Hanlon, B. T. Tuten, C. A. Tooley, P. G. Frank, and E. B. Berda, "A brief user's guide to single-chain nanoparticles," *Polymer Chemistry*, vol. 6, no. 2, pp. 181–197, 2015.

[29] Y. Matsumura and H. Maeda, "A new concept for macromolecular therapeutics in cancer chemotherapy: mechanism of tumoritropic accumulation of proteins and the antitumor agent smancs," *Cancer research*, vol. 46, no. 12 Part 1, pp. 6387–6392, 1986.

[30] D. Peer, J. M. Karp, S. Hong, O. C. Farokhzad, R. Margalit, and R. Langer, "Nanocarriers as an emerging platform for cancer therapy," *Nature nanotechnology*, vol. 2, no. 12, p. 751, 2007.

[31] E. H. Wong, S. J. Lam, E. Nam, and G. G. Qiao, "Biocompatible single-chain polymeric nanoparticles via organo-catalyzed ring-opening polymerization," *ACS Macro Letters*, vol. 3, no. 6, pp. 524–528, 2014.

[32] Y. Bai, H. Xing, G. A. Vincil, J. Lee, E. J. Henderson, Y. Lu, N. G. Lemcoff, and S. C. Zimmerman, "Practical synthesis of water-soluble organic nanoparticles with a single reactive group and a functional carrier scaffold," *Chem. Sci.*, vol. 5, pp. 2862–2868, 2014.

[33] A. B. Benito, M. K. Aiertza, M. Marradi, L. Gil-Iceta, T. Shekhter Zahavi, B. Szczupak, M. Jiménez-González, T. Reese, E. Scanziani, L. Passoni, *et al.*, "Functional

single-chain polymer nanoparticles: targeting and imaging pancreatic tumors in vivo," *Biomacromolecules*, vol. 17, no. 10, pp. 3213–3221, 2016.

[34] A. Sanchez-Sanchez, S. Akbari, A. Etxeberria, A. Arbe, U. Gasser, A. J. Moreno, J. Colmenero, and J. A. Pomposo, ""michael" nanocarriers mimicking transient-binding disordered proteins," *ACS Macro Letters*, vol. 2, no. 6, pp. 491–495, 2013.

[35] A. Sanchez-Sanchez, S. Akbari, A. J. Moreno, F. L. Verso, A. Arbe, J. Colmenero, and J. A. Pomposo, "Design and preparation of single-chain nanocarriers mimicking disordered proteins for combined delivery of dermal bioactive cargos," *Macromolecular Rapid Communications*, vol. 34, no. 21, pp. 1681–1686, 2013.

[36] C. Song, L. Li, L. Dai, and S. Thayumanavan, "Responsive single-chain polymer nanoparticles with host–guest features," *Polymer Chemistry*, vol. 6, no. 26, pp. 4828–4834, 2015.

[37] C.-C. Cheng, D.-J. Lee, Z.-S. Liao, and J.-J. Huang, "Stimuli-responsive single-chain polymeric nanoparticles towards the development of efficient drug delivery systems," *Polymer Chemistry*, vol. 7, no. 40, pp. 6164–6169, 2016.

[38] S. K. Hamilton and E. Harth, "Molecular dendritic transporter nanoparticle vectors provide efficient intracellular delivery of peptides," *ACS Nano*, vol. 3, no. 2, pp. 402–410, 2009. PMID: 19236078.

[39] I. Perez-Baena, I. Loinaz, D. Padro, I. García, H. J. Grande, and I. Odriozola, "Single-chain polyacrylic nanoparticles with multiple gd(iii) centres as potential mri contrast agents," *J. Mater. Chem.*, vol. 20, pp. 6916–6922, 2010.

[40] C. T. Adkins, J. N. Dobish, S. Brown, and E. Harth, "Water-soluble semiconducting nanoparticles for imaging," *ACS macro letters*, vol. 2, no. 8, pp. 710–714, 2013.

[41] M. A. Gillissen, I. K. Voets, E. Meijer, and A. R. Palmans, "Single chain polymeric nanoparticles as compartmentalised sensors for metal ions," *Polymer Chemistry*, vol. 3, no. 11, pp. 3166–3174, 2012.

[42] C. T. Adkins, H. Muchalski, and E. Harth, "Nanoparticles with individual site-isolated semiconducting polymers from intramolecular chain collapse processes," *Macromolecules*, vol. 42, no. 15, pp. 5786–5792, 2009.

[43] G. Li, F. Tao, L. Wang, Y. Li, and R. Bai, "A facile strategy for preparation of single-chain polymeric nanoparticles by intramolecular photo-crosslinking of azide polymers," *Polymer*, vol. 55, no. 16, pp. 3696–3702, 2014.

[44] P. Wang, H. Pu, J. Ge, M. Jin, H. Pan, Z. Chang, and D. Wan, "Fluorescence-labeled hydrophilic nanoparticles via single-chain folding," *Materials Letters*, vol. 132, pp. 102–105, 2014.

[45] C. K. Lyon, E. O. Hill, and E. B. Berda, "Zipping polymers into nanoparticles via intrachain alternating radical copolymerization," *Macromolecular Chemistry and Physics*, vol. 217, no. 3, pp. 501–508, 2016.

[46] G. Qian, B. Zhu, Y. Wang, S. Deng, and A. Hu, "Size-tunable polymeric nanore-actors for one-pot synthesis and encapsulation of quantum dots," *Macromolecular rapid communications*, vol. 33, no. 16, pp. 1393–1398, 2012.

[47] T. Terashima, T. Mes, T. F. A. De Greef, M. A. J. Gillissen, P. Besenius, A. R. A. Palmans, and E. W. Meijer, "Single-chain folding of polymers for catalytic systems in water," *Journal of the American Chemical Society*, vol. 133, no. 13, pp. 4742–4745, 2011. PMID: 21405022.

[48] M. Artar, T. Terashima, M. Sawamoto, E. Meijer, and A. R. Palmans, "Under-standing the catalytic activity of single-chain polymeric nanoparticles in water," *Journal of Polymer Science Part A: Polymer Chemistry*, vol. 52, no. 1, pp. 12–20, 2014.

[49] E. Huerta, P. J. M. Stals, E. W. Meijer, and A. R. A. Palmans, "Consequences of folding a water-soluble polymer around an organocatalyst," *Angewandte Chemie International Edition*, vol. 52, no. 10, pp. 2906–2910, 2013.

[50] E. Huerta, B. van Genabeek, P. J. Stals, E. Meijer, and A. R. Palmans, "A modular approach to introduce function into single-chain polymeric nanoparticles," *Macro-molecular rapid communications*, vol. 35, no. 15, pp. 1320–1325, 2014.

[51] S. Mavila, I. Rozenberg, and N. G. Lemcoff, "A general approach to mono-and bimetallic organometallic nanoparticles," *Chemical Science*, vol. 5, no. 11, pp. 4196–4203, 2014.

[52] Y. Liu, T. Pauloehrl, S. I. Presolski, L. Albertazzi, A. R. Palmans, and E. Meijer, "Modular synthetic platform for the construction of functional single-chain poly-meric nanoparticles: from aqueous catalysis to photosensitization," *Journal of the American Chemical Society*, vol. 137, no. 40, pp. 13096–13105, 2015.

[53] J. Willenbacher, O. Altintas, V. Trouillet, N. Knöfel, M. J. Monteiro, P. W. Roesky, and C. Barner-Kowollik, "Pd-complex driven formation of single-chain nanoparticles," *Polymer Chemistry*, vol. 6, no. 24, pp. 4358–4365, 2015.

[54] M. Artar, E. R. Souren, T. Terashima, E. Meijer, and A. R. Palmans, "Single chain polymeric nanoparticles as selective hydrophobic reaction spaces in water," *ACS Macro Letters*, vol. 4, no. 10, pp. 1099–1103, 2015.

[55] Y. Bai, X. Feng, H. Xing, Y. Xu, B. K. Kim, N. Baig, T. Zhou, A. A. Gewirth, Y. Lu, E. Oldfield, *et al.*, "A highly efficient single-chain metal–organic nanoparticle catalyst for alkyne–azide "click" reactions in water and in cells," *Journal of the American Chemical Society*, vol. 138, no. 35, pp. 11077–11080, 2016.

[56] I. Perez-Baena, F. Barroso-Bujans, U. Gasser, A. Arbe, A. J. Moreno, J. Colmenero, and J. A. Pomposo, "Endowing single-chain polymer nanoparticles with enzyme-mimetic activity," *ACS Macro Letters*, vol. 2, no. 9, pp. 775–779, 2013.

[57] A. Sanchez-Sanchez, A. Arbe, J. Kohlbrecher, J. Colmenero, and J. A. Pomposo, "Efficient synthesis of single-chain globules mimicking the morphology and polymerase activity of metalloenzymes," *Macromolecular rapid communications*, vol. 36, no. 17, pp. 1592–1597, 2015.

[58] J. He, L. Tremblay, S. Lacelle, and Y. Zhao, "Preparation of polymer single chain nanoparticles using intramolecular photodimerization of coumarin," *Soft Matter*, vol. 7, no. 6, pp. 2380–2386, 2011.

[59] B. Zhu, S. Sun, Y. Wang, S. Deng, G. Qian, M. Wang, and A. Hu, "Preparation of carbon nanodots from single chain polymeric nanoparticles and theoretical investigation of the photoluminescence mechanism," *Journal of Materials Chemistry C*, vol. 1, no. 3, pp. 580–586, 2013.

[60] A. Latorre-Sanchez and J. A. Pomposo, "A simple, fast and highly sensitive colorimetric detection of zein in aqueous ethanol via zein–pyridine–gold interactions," *Chemical Communications*, vol. 51, no. 86, pp. 15736–15738, 2015.

[61] B. Zhu, J. Ma, Z. Li, J. Hou, X. Cheng, G. Qian, P. Liu, and A. Hu, "Formation of polymeric nanoparticles via bergman cyclization mediated intramolecular chain collapse," *Journal of Materials Chemistry*, vol. 21, no. 8, pp. 2679–2683, 2011.

[62] J. A. Kaitz, C. M. Possanza, Y. Song, C. E. Diesendruck, A. J. H. Spiering, E. Meijer, and J. S. Moore, "Depolymerizable, adaptive supramolecular polymer nanoparticles and networks," *Polymer Chemistry*, vol. 5, no. 12, pp. 3788–3794, 2014.

[63] I. Perez-Baena, A. J. Moreno, J. Colmenero, and J. A. Pomposo, "Single-chain nanoparticles vs. star, hyperbranched and dendrimeric polymers: effect of the nanoscopic architecture on the flow properties of diluted solutions," *Soft Matter*, vol. 10, no. 47, pp. 9454–9459, 2014.

[64] M. E. Mackay, T. T. Dao, A. Tuteja, D. L. Ho, B. Van Horn, H.-C. Kim, and C. J. Hawker, "Nanoscale effects leading to non-einstein-like decrease in viscosity," *Nature materials*, vol. 2, no. 11, p. 762, 2003.

[65] L. Oria, R. Aguado, J. A. Pomposo, and J. Colmenero, "A versatile "click" chemistry precursor of functional polystyrene nanoparticles," *Advanced Materials*, vol. 22, no. 28, pp. 3038–3041, 2010.

[66] M. E. Mackay, A. Tuteja, P. M. Duxbury, C. J. Hawker, B. Van Horn, Z. Guan, G. Chen, and R. Krishnan, "General strategies for nanoparticle dispersion," *Science*, vol. 311, no. 5768, pp. 1740–1743, 2006.

[67] A. Tuteja, P. M. Duxbury, and M. E. Mackay, "Multifunctional nanocomposites with reduced viscosity," *Macromolecules*, vol. 40, no. 26, pp. 9427–9434, 2007.

[68] A. Tuteja, M. E. Mackay, C. J. Hawker, and B. Van Horn, "Effect of ideal, organic nanoparticles on the flow properties of linear polymers: non-einstein-like behavior," *Macromolecules*, vol. 38, no. 19, pp. 8000–8011, 2005.

[69] J. A. Pomposo, A. R. de Luzuriaga, I. García, A. Etxeberria, and J. Colmenero, "A nanotechnology pathway to arresting phase separation in soft nanocomposites," *Macromolecular rapid communications*, vol. 32, no. 7, pp. 573–578, 2011.

[70] A. Arbe, J. A. Pomposo, I. Asenjo-Sanz, D. Bhowmik, O. Ivanova, J. Kohlbrecher, and J. Colmenero, "Single chain dynamic structure factor of linear polymers in an all-polymer nano-composite," *Macromolecules*, vol. 49, no. 6, pp. 2354–2364, 2016.

[71] D. Bhowmik, J. A. Pomposo, F. Juranyi, V. García-Sakai, M. Zamponi, Y. Su, A. Arbe, and J. Colmenero, "Microscopic dynamics in nanocomposites of poly (ethylene oxide) and poly (methyl methacrylate) soft nanoparticles: a quasi-elastic neutron scattering study," *Macromolecules*, vol. 47, no. 1, pp. 304–315, 2013.

[72] D. Bhowmik, J. A. Pomposo, F. Juranyi, V. García Sakai, M. Zamponi, A. Arbe, and J. Colmenero, "Investigation of a nanocomposite of 75 wt% poly (methyl methacrylate) nanoparticles with 25 wt% poly (ethylene oxide) linear chains: a quasielatic neutron scattering, calorimetric, and waxs study," *Macromolecules*, vol. 47, no. 9, pp. 3005–3016, 2014.

[73] J. Pomposo, A. Ruiz de Luzuriaga, A. Etxeberria, and J. Rodríguez, "Key role of entropy in nanoparticle dispersion: polystyrene-nanoparticle/linear-polystyrene nanocomposites as a model system.," *Physical chemistry chemical physics*, vol. 10, no. 5, pp. 650–651, 2008.

[74] A. Ruiz de Luzuriaga, A. Etxeberria, J. Rodríguez, and J. A. Pomposo, "Phase diagram and entropic interaction parameter of athermal all-polymer nanocomposites," *Polymers for Advanced Technologies*, vol. 19, no. 7, pp. 756–761, 2008.

[75] A. Ruiz de Luzuriaga, H. Grande, and J. A. Pomposo, "A theoretical investigation of polymer-nanoparticles as miscibility improvers in all-polymer nanocomposites," *Journal of Nano Research*, vol. 2, pp. 105–114, 2008.

[76] A. Ruiz de Luzuriaga, H. J. Grande, and J. A. Pomposo, "Phase diagrams in compressible weakly interacting all-polymer nanocomposites," *The Journal of chemical physics*, vol. 130, no. 8, pp. 756–761, 2009.

[77] S. Montes, H. Grande, A. Etxeberria, and J. A. Pomposo, "Miscibility enhancement in all-polymer nanocomposites composed of weakly-charged flexible chains and polar nanoparticles," *Journal of Nano Research*, vol. 6, pp. 123–132, 2009.

[78] P. Khanjani, I. Perez-Baena, L. Buruaga, and J. A. Pomposo, "Unimolecular nanoparticles via carbon-carbon "click" chemistry for all-polymer nanocomposites," *Macromolecular Symposia*, vol. 321-322, no. 1, pp. 145–149, 2012.

[79] M. Rubinstein and R. H. Colby, *Polymer Physics*, vol. 23. Oxford University Press: Oxford, U.K., 2003.

[80] W. Commons. `https://commons.wikimedia.org/wiki/File:Sierpinski_triangle_evolution.svg`. Accessed on 2/12/2019.

[81] J. Baschnagel, J. Wittmer, and H. Meyer, *Computational Soft Matter: From Synthetic Polymers to Proteins*, ch. Monte Carlo Simulation of Polymers: Coarse-Grained Models, pp. 83—-140. NIC, 2004.

[82] G. Njikang, I. C. Kwan, G. Wu, and G. Liu, "Nmr quantification of the partition of coronal chain segments of block copolymer vesicles," *Polymer*, vol. 50, no. 22, pp. 5262–5267, 2009.

[83] J. Moore, "Gel permeation chromatography. i. a new method for molecular weight distribution of high polymers," *Journal of Polymer Science Part A: General Papers*, vol. 2, no. 2, pp. 835–843, 1964.

[84] A. Striegel, W. W. Yau, J. J. Kirkland, and D. D. Bly, *Modern size-exclusion liquid chromatography: practice of gel permeation and gel filtration chromatography*. John Wiley & Sons, 2009.

[85] I. Teraoka, "Calibration of retention volume in size exclusion chromatography by hydrodynamic radius," *Macromolecules*, vol. 37, no. 17, pp. 6632–6639, 2004.

[86] D. M. Stevens, S. Tempelaar, A. P. Dove, and E. Harth, "Nanosponge formation from organocatalytically synthesized poly (carbonate) copolymers," *ACS macro letters*, vol. 1, no. 7, pp. 915–918, 2012.

[87] E. A. Appel, J. del Barrio, J. Dyson, L. Isaacs, and O. A. Scherman, "Metastable single-chain polymer nanoparticles prepared by dynamic cross-linking with nor-seco-cucurbit [10] uril," *Chemical Science*, vol. 3, no. 7, pp. 2278–2281, 2012.

[88] J. A. Pomposo, I. Perez-Baena, F. Lo Verso, A. J. Moreno, A. Arbe, and J. Colmenero, "How far are single-chain polymer nanoparticles in solution from the globular state?," *ACS Macro Letters*, vol. 3, no. 8, pp. 767–772, 2014.

[89] A. Arbe, J. A. Pomposo, A. Moreno, F. LoVerso, M. González-Burgos, I. Asenjo-Sanz, A. Iturrospe, A. Radulescu, O. Ivanova, and J. Colmenero, "Structure and dynamics of single-chain nano-particles in solution," *Polymer*, vol. 105, pp. 532–544, 2016.

[90] D. K. Wilkins, S. B. Grimshaw, V. Receveur, C. M. Dobson, J. A. Jones, and L. J. Smith, "Hydrodynamic radii of native and denatured proteins measured by pulse field gradient nmr techniques," *Biochemistry*, vol. 38, no. 50, pp. 16424–16431, 1999. PMID: 10600103.

[91] J. A. Marsh and J. D. Forman-Kay, "Sequence determinants of compaction in intrinsically disordered proteins," *Biophysical journal*, vol. 98, no. 10, pp. 2383–2390, 2010.

[92] H. Hofmann, A. Soranno, A. Borgia, K. Gast, D. Nettels, and B. Schuler, "Polymer scaling laws of unfolded and intrinsically disordered proteins quantified with single-molecule spectroscopy," *Proceedings of the National Academy of Sciences*, vol. 109, no. 40, pp. 16155–16160, 2012.

[93] P. Bernado and D. I. Svergun, "Structural analysis of intrinsically disordered proteins by small-angle x-ray scattering," *Molecular biosystems*, vol. 8, no. 1, pp. 151–167, 2012.

[94] W. W. Smith, P.-Y. Ho, and C. S. O'Hern, "Calibrated langevin-dynamics simulations of intrinsically disordered proteins," *Physical Review E*, vol. 90, no. 4, p. 042709, 2014.

[95] V. Receveur-Bréchot and D. Durand, "How random are intrinsically disordered proteins? a small angle scattering perspective," *Current Protein and Peptide Science*, vol. 13, no. 1, pp. 55–75, 2012.

[96] J. Habchi, P. Tompa, S. Longhi, and V. N. Uversky, "Introducing protein intrinsic disorder," *Chemical reviews*, vol. 114, no. 13, pp. 6561–6588, 2014.

[97] R. Van Der Lee, M. Buljan, B. Lang, R. J. Weatheritt, G. W. Daughdrill, A. K. Dunker, M. Fuxreiter, J. Gough, J. Gsponer, D. T. Jones, *et al.*, "Classification of intrinsically disordered regions and proteins," *Chemical reviews*, vol. 114, no. 13, pp. 6589–6631, 2014.

[98] H.-X. Zhou, G. Rivas, and A. P. Minton, "Macromolecular crowding and confinement: biochemical, biophysical, and potential physiological consequences," *Annu. Rev. Biophys.*, vol. 37, pp. 375–397, 2008.

[99] D. Johansen, C. M. Jeffries, B. Hammouda, J. Trewhella, and D. P. Goldenberg, "Effects of macromolecular crowding on an intrinsically disordered protein characterized by small-angle neutron scattering with contrast matching," *Biophysical journal*, vol. 100, no. 4, pp. 1120–1128, 2011.

[100] A. Soranno, I. Koenig, M. B. Borgia, H. Hofmann, F. Zosel, D. Nettels, and B. Schuler, "Single-molecule spectroscopy reveals polymer effects of disordered proteins in crowded environments," *Proceedings of the National Academy of Sciences*, vol. 111, no. 13, pp. 4874–4879, 2014.

[101] M. Mondello, H.-J. Yang, H. Furuya, and R.-J. Roe, "Molecular dynamics simulation of atactic polystyrene. 1. comparison with x-ray scattering data," *Macromolecules*, vol. 27, no. 13, pp. 3566–3574, 1994.

[102] J. W. Liu, M. E. Mackay, and P. M. Duxbury, "Nanoparticle formation by crosslinking a macromolecule," *EPL (Europhysics Letters)*, vol. 84, no. 4, p. 46001, 2008.

[103] J. Liu, M. Mackay, and P. Duxbury, "Molecular dynamics simulation of intramolecular cross-linking of bcb/styrene copolymers," *Macromolecules*, vol. 42, no. 21, pp. 8534–8542, 2009.

[104] F. Ferrante, F. L. Celso, and D. Duca, "Construction and characterization of models of hypercrosslinked polystyrene," *Colloid and Polymer Science*, vol. 290, no. 14, pp. 1443–1450, 2012.

[105] A. J. Moreno, F. Lo Verso, A. Sanchez-Sanchez, A. Arbe, J. Colmenero, and J. A. Pomposo, "Advantages of orthogonal folding of single polymer chains to soft nanoparticles," *Macromolecules*, vol. 46, no. 24, pp. 9748–9759, 2013.

[106] A. J. Moreno, F. Lo Verso, A. Arbe, J. A. Pomposo, and J. Colmenero, "Concentrated solutions of single-chain nanoparticles: A simple model for intrinsically disordered proteins under crowding conditions," *J. Phys. Chem. Lett.*, vol. 7, no. 5, pp. 838–844, 2016.

[107] M. Gonzalez-Burgos, A. Arbe, A. J. Moreno, J. A. Pomposo, A. Radulescu, and J. Colmenero, "Crowding the environment of single-chain nanoparticles: A combined study by sans and simulations," *Macromolecules*, vol. 51, no. 4, pp. 1573–1585, 2018.

Chapter 2

Model for SCNPs and Simulation Details

2.1 Introduction

Beginning with the advent of the first computers, simulations have emerged as the invaluable third pillar of the natural sciences, bridging the gap between theory and experiments. Today they are successfully being employed from the smallest to the biggest length and time scales: from resolving electronic structures by quantum *ab initio* methods, modeling the response of cells through the interaction between thousands of proteins by network analysis to tracing the expansion of the universe. It is impossible to name a topic in physics, chemistry or biology to which computer simulations have not made major contributions.

On a very general level, simulations can broadly be divided into two categories: (i) methods that propagate the system in time according to specified interaction potentials and thus produce a 'trajectory' of the system, and (ii) methods that produce an ensemble of conformations of the system with the correct statistical distribution, but provide no dynamical information. Molecular dynamics (MD) is the simplest and best known example of the former, while Monte Carlo (MC) represents the archetype of the latter.

In polymer physics, a particular challenge for the modeling via computer simulation is the hierarchy of length and time-scales present in polymeric systems: On the lower end, atomic vibrations governed by the specific chemistry of the monomers occur on the scale of Ångström and sub-picoseconds. On an intermediate level, the connectivity of the polymer backbone leads to entanglements, which form on the scale of nanometers and nanoseconds. The movement of a typical polymer of micrometer size through a dense melt via reptation occurs during milliseconds. Finally, self-assembly processes, which depend on the interplay between various low-energy interactions and entropical costs, can take even longer to reach their equilibrium state.

Therefore, depending on the process under investigation and the level of detail necessary to understand it, a certain degree of coarse-graining is usually employed in simulations of polymeric systems. This involves reducing the degrees of freedom in the system by either constraining certain movements or replacing the atoms by abstract 'beads'. These can represent a single carbon atom together with its hydrogens, the center-of-mass of several backbone atoms (e.g. a monomer unit) or even a bigger polymer segment, such as a whole Kuhn length. The specific potentials governing the interactions between these new 'beads' are optimized to quantitatively describe the structural and dynamical properties on the length and time scale of interest.

In this thesis, we employ Molecular Dynamics simulations, and extensions thereof, as our main tool for elucidating the structural and dynamical properties of polymer solutions. The models we use to describe the polymers as well as their interactions shall be introduced next in this chapter, followed by a detailed explanation of the algorithms and simulation methods that define the rules according to which the system is propagated in time.

2.2 Coarse-grained Bead-Spring Model

The simulations presented in this thesis are all based upon the same model of both the polymeric precursors as well as the cross-linked single-chain nanoparticles. The precursor polymers consist of a number N of monomers attached to each other in a linear fashion. A fraction $f = N_r/N$ of these beads is reactive, meaning they can cross-link with other reactive groups to form irreversible or reversible bonds. In terms of the interactions between monomers, we follow the well-established Gremer-Krest model [1], which treats a polymer as a coarse-grained chain consisting of beads and springs. Good solvent conditions are implicitly provided by subjecting all monomers to an effective repulsive *Lennard-Jones* potential, i.e.:

$$U^{\text{LJ}}(r) = 4\epsilon \left[\left(\frac{\sigma}{r} \right)^{12} - \left(\frac{\sigma}{r} \right)^{6} + \frac{1}{4} \right] , \tag{2.1}$$

with a cutoff distance $r_{\text{c}} = 2^{1/6}\sigma$, at which both the potential and the corresponding forces are continuous. Neighboring monomers along the polymeric backbone interact with each other via a *finitely-extensible nonlinear elastic* (FENE) potential of the following form:

$$U^{\text{FENE}}(r) = -\epsilon K_{\text{F}} R_0^2 \ln \left[1 - \left(\frac{r}{R_0} \right)^{2} \right] , \tag{2.2}$$

with $K_{\text{F}} = 15$ and $R_0 = 1.5$. Combining LJ and FENE potentials in this way results in a deep energy minimum at $r \approx \sigma$, which defines the bead size of each monomer. Potentials 2.1 and 2.2 further guarantee that chains are unable to cross each other and limit the fluctuation of bonds. Since the polymer is modeled as a fully flexible chain without bending or torsion energies, each bead qualitatively represents a Kuhn length [2] of a real polymer, which is typically around 6-10 Å in common polymers. Unless otherwise specified, simulations were carried out employing standard LJ units, $\epsilon = \sigma = m = 1$ (with m being the monomer mass), setting the energy, length and time ($\tau = \sqrt{\sigma^2 m/\epsilon} \approx 1\text{ps}$ [1]) scales, respectively.

The reactive monomeric species can form either irreversible (as in irreversible SCNPs, Chapters 3, 4) or reversible bonds (as in reversible SCNPs forming physical gels, Chapter

5). The former are modeled via the same FENE potential as monomers along the polymer backbone. In the case of reversible bonds, the interaction takes the form of a Morse potential for the duration of a given bond:

$$U^{\text{rev}}(r) = K \left[2e^{(r_0-r)} - e^{2(r_0-r)} \right] , \tag{2.3}$$

where the parameter K governs the bond strength through modulating the energy barrier that has to be overcome in order to break the bond, and r_0 is chosen such that the minimum of the sum of non-bonded and bonded interactions for both irreversible and reversible bonds is similar in intensity and position. Figure 2.1 shows the total interaction between two bonded monomers for the FENE case and for several realizations of the Morse potential. In the simulations of Chapter 5 we used $K = 29.6, r_0 = 1.448$ and $K = 33.7, r_0 = 1.477$.
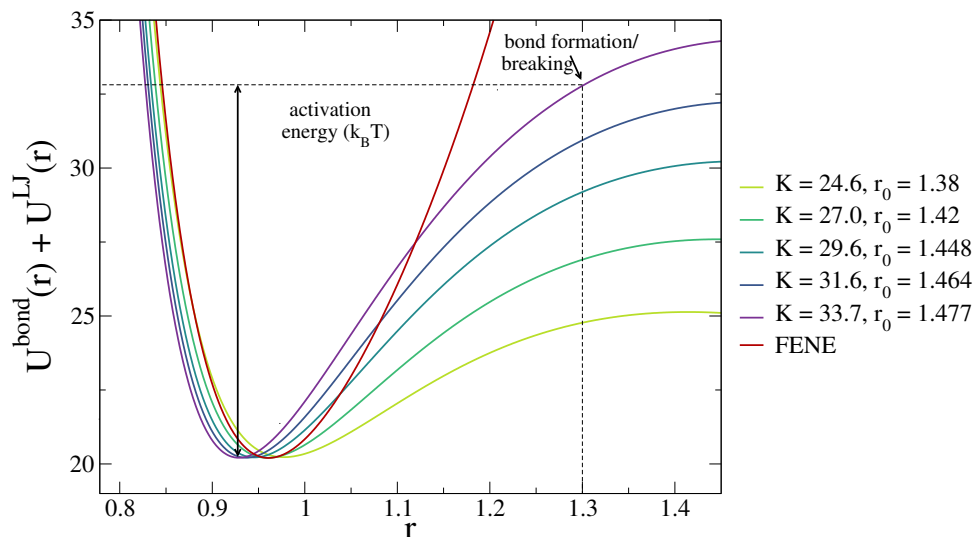

Figure 2.1: Sum of bonded and non-bonded potentials in both the irreversible (FENE) and reversible case with different bond strengths K.

2.3 The Cross-linking Process

Cross-linking in our simulations is supposed to mimic a chemical reaction that takes place between two reactive groups when they approach each other. However, this process is simplified in several ways. We treat cross-links as isotropic and monofunctional. As such, each reactive monomer can only form one bond and in the irreversible case, once formed, such a bond cannot be broken. No directionality is imposed to the bonding process: at any given time, unbonded reactive monomers can cross-link if they are separated by less than

the "capture distance" $r_c = 1.3\sigma$, regardless of their orientation. Should more than one cross-link be possible for a particular monomer, one of the candidate bonds is chosen randomly. Once a bond is formed, in the irreversible case the two involved monomers interact via the FENE potential introduced in Equation 2.2 for the remainder of the simulation. It should be noted that the assumption of isotropic cross-links is adequate to model systems with relatively long side groups that can perform broad rotations. Otherwise directional constraints (e.g., through 'patchy' interactions [3, 4, 5]) should be included to have a more realistic model.

2.4 Reversible Bond Formation and Breakage

Our goal in coming up with a model for a reversible equivalent of the irreversibly cross-linked single-chain nanoparticles was to mimic the character of the irreversible bonds as closely as possible. To this end, we enforce monofunctionality by keeping a list of bonds and we use the same method of bond formation, i.e. a bond is formed if two currently unbonded reactive monomers are within each other's capture distance $r_c = 1.3\sigma$. Subsequently, they interact via the Morse potential given by Equation 2.3. Such a bond can be broken again, if, at a given time-step, the two involved monomers are separated by more than the capture distance r_c. The likelihood of such a bond-breaking event, and thus also the average lifetime of bonds, is governed by the effective activation energy, given by the potential difference at r_c and at the potential minimum (see Figure 2.1). When a bond is broken, the two involved monomers are free to react again, with each other or different partners, once they encounter reactive monomers within the capture distance.

2.5 Molecular Dynamics

In Molecular Dynamics simulations, the time evolution of a system of N interacting atoms or coarse-grained 'beads' is calculated deterministically according to Newton's equations of motion,

$$m_i \frac{\mathrm{d}^2 \boldsymbol{r}_i(t)}{\mathrm{d}t^2} = \boldsymbol{F}_i(t) \text{ with } i = 1, \dots, N \,, \tag{2.4}$$

where m_i, $\boldsymbol{r}_i(t)$ denote the mass and position of a given bead i and $\boldsymbol{F}_i(t)$ is the total force acting on said bead at a given time t. It is given by the negative gradient of the total

potential energy function U with respect to bead i,

$$\boldsymbol{F}_i = -\nabla_{\boldsymbol{r}_i} U(\boldsymbol{r}_1, \ldots, \boldsymbol{r}_N) = \left(\frac{\partial U}{\partial x_i}, \frac{\partial U}{\partial y_i}, \frac{\partial U}{\partial z_i} \right) . \tag{2.5}$$

Together with the initial coordinates and velocities of the beads, the choice of the potentials governing the interactions between individual MD beads thus completely determines the time evolution of the system in theory. However, since Newton's equations of motion are continuous, while CPUs are inherently digital and resources are limited, MD simulations solve these equations numerically by integration. How accurately a particular algorithm follows the 'true' trajectory of the system depends on the time-step and the order of the integration scheme. In this thesis, we employ the Velocity-Verlet algorithm [6, 7] to evolve the positions and velocities of the beads in the system, i.e.

$$\boldsymbol{r}_i(t + \Delta t) = \boldsymbol{r}_i(t) + \boldsymbol{v}_i(t)\Delta t + \frac{\boldsymbol{F}_i(t)}{2m}\Delta t^2 , \tag{2.6}$$

$$\boldsymbol{v}_i(t + \Delta t) = \boldsymbol{v}_i(t) + \frac{1}{2m} \left(\boldsymbol{F}_i(t) + \boldsymbol{F}_i(t + \Delta t) \right) \Delta t . \tag{2.7}$$

At first glance, this appears to involve two force calculations per time-step, but in practice only one additional force calculation is needed in the beginning of the simulation. At each step, the algorithm performs the following operations: 1. update the velocities with the old forces (half step):

$$\boldsymbol{v}_i(t + \Delta t/2) = \boldsymbol{v}_i(t) + \frac{1}{2m}\boldsymbol{F}_i(t)\Delta t , \tag{2.8}$$

2. update the positions (full step):

$$\boldsymbol{r}_i(t + \Delta t) = \boldsymbol{r}_i(t) + \boldsymbol{v}_i(t + \Delta t/2)\Delta t , \tag{2.9}$$

3. recalculate the forces with the new positions, and finally

4. update the velocities with the new forces (half step):

$$\boldsymbol{v}_i(t + \Delta t) = \boldsymbol{v}_i(t + \Delta t/2) + \frac{1}{2m}\boldsymbol{F}_i(t + \Delta t)\Delta t . \tag{2.10}$$

The computationally most expensive task in MD simulation is the calculation of the pair-wise additive forces, since it amounts to evaluating $N(N-1)/2$ distances and interaction potentials. However, since all of our potential energy functions are short-ranged and cut-off at a certain distance r_c, only beads within a radius of r_c contribute to the force acting on a specific bead. To speed up our calculations by limiting the amount of

force calculations, we use cell-lists [8] or Verlet lists [6, 7], depending on performance for a particular problem. Cell lists are constructed by dividing the simulation box into smaller cells of lattice constant $l \geq r_c$, such that only beads belonging to one of the 27 neighboring cells (for a cubic box in 3 dimensions) have to be taken into account in the force calculation. These cell lists can also be used to fill a Verlet list for each bead, denoting the indices of neighboring beads within a distance r_v slightly larger than r_c. These can then be used instead of cell lists for the force calculations for several steps and only have to be updated whenever any bead has been displaced by more than $r_v - r_c$ since the last construction of Verlet lists. One of the two methods or a combination of both of them was used in the different simulations reported in the following Chapters. Single Verlet lists are convenient for small systems ($\sim O(10^2)$ particles) and were used for the cross-linking of isolated SCNPs (Chapter 4). The simulations of big systems ($\sim O(10^4) - O(10^5)$) in equilibrium (for example cross-linking under crowding in Chapters 2.3 or gel formation in Chapter 5) used a combination of cell and Verlet lists. The simulations under shear flow (Chapter 4) only used cell lists. The use of Verlet lists in such simulations is inefficient since the list needs to be updated very frequently in regions of the box where shear flows lead to large displacements per time-step.

2.6 Langevin Dynamics

In classic MD simulations, solvent molecules would be explicitly included as smaller and lighter beads with specific interactions between each other and with the solute beads. However, in most scenarios in soft matter and polymer physics, the specific details of the trajectory of the solvent molecules is not of interest. At the same time, however, their effect on the polymer dynamics can not be neglected. A further complication arises from the disparate length and time scales of solvent and solute, the former of which can be orders of magnitude smaller than the latter and thus would explode computational cost if the solvent were to be included explicitly in the simulation.

To circumvent this problem, several methods have been designed to alter the Molecular Dynamics simulation in such a way that the effect of the solvent is considered without dramatically increasing computing time. One of the most widely used of these techniques is Langevin Dynamics (LD) [9], which adds frictional and random force terms to Newton's equations of motion to account for the collisions between solvent and solute. The resulting Langevin equation reads

$$m_i \frac{\mathrm{d}^2 \boldsymbol{r}_i(t)}{\mathrm{d}t^2} = \boldsymbol{F}_i(t) - \gamma m_i \frac{\mathrm{d}\boldsymbol{r}_i(t)}{\mathrm{d}t} + \mathcal{R}_i(t) \tag{2.11}$$

where γ denotes the friction coefficient, which is proportional to the viscosity of the solvent. The random force term $\mathcal{R}_i(t)$ is an uncorrelated stationary Gaussian process of zero mean $\langle \mathcal{R}_i^\alpha(t) \rangle = 0$ and variance $\langle \mathcal{R}_i^\alpha(t)\mathcal{R}_j^\beta(t') \rangle = 2\gamma m k_B T \delta_{ij}\delta_{\alpha\beta}\delta(t - t')$. Apart from introducing friction in the system, Langevin Dynamics also acts as a thermostat to keep the system at a constant temperature T through the random force. Its limiting distribution corresponds to a canonical ensemble (NVT).

The Langevin equations of motion can easily be implemented as an extension of the Velocity Verlet algorithm by introducing a 'fluctuation' after the first velocity half step (Equation 2.8). The complete set of equations then amounts to

$$\tilde{\boldsymbol{v}}_i(t + \Delta t/2) = \boldsymbol{v}_i(t) + \frac{\Delta t}{2m}\boldsymbol{F}_i(t)\,, \tag{2.12}$$

$$\boldsymbol{v}_i' = e^{-\gamma\Delta t}\tilde{\boldsymbol{v}}_i + \sqrt{\frac{2\gamma k_B T}{m_i}}\mathcal{R}_i^{(1)}\,, \tag{2.13}$$

$$\boldsymbol{r}_i(t + \Delta t) = \boldsymbol{r}_i(t) + \frac{1 - e^{-\gamma\Delta t}}{\gamma}\tilde{\boldsymbol{v}}_i + \sqrt{\frac{2k_B T}{\gamma m_i}}\mathcal{R}_i^{(2)}\,. \tag{2.14}$$

$$\boldsymbol{v}_i(t + \Delta t) = \boldsymbol{v}_i' + \frac{\Delta t}{2m}\boldsymbol{F}_i(t + \Delta t)\,. \tag{2.15}$$

The vectors R_1 and R_2 are given by

$$\begin{pmatrix} \mathcal{R}_i^{(1)\alpha} \\ \mathcal{R}_i^{(2)\alpha} \end{pmatrix} = \begin{pmatrix} \sqrt{\tau_2} & 0 \\ \frac{\tau_1 - \tau_2}{\sqrt{\tau_2}} & \sqrt{\Delta t - \frac{\tau_1^2}{\tau_2}} \end{pmatrix} \cdot \begin{pmatrix} \Omega_i^{(1)\alpha} \\ \Omega_i^{(2)\alpha} \end{pmatrix} \tag{2.16}$$

where α denotes Cartesian components and $\tau_k = (1 - e^{-k\gamma\Delta t})/(k\gamma)$. The quantities $\Omega_i^{(1)a}$ are independent Gaussian random variables of zero mean and variance 1. For a detailed derivation of the algorithm, the reader is referred to the original article introducing the method, Reference [10].

2.7 Multiparticle Collision Dynamics

While Langevin Dynamics accounts for friction between solvent and solute and energy exchange with a heat bath, it does not correctly resolve hydrodynamic interactions for dense solvents. In dilute and semi-dilute solutions of polymers, the hydrodynamic interactions

are not screened by the much stronger excluded volume interactions, and can strongly affect or even dominate the dynamics of the macromolecules [11, 12]. For example, the exclusion or inclusion of hydrodynamic interactions determines the differences between the Rouse [13] and the Zimm [14] model describing the dynamics of ideal chains. Several meso-scale simulation methods have been developed to accurately describe the build-up and propagation of hydrodynamic information. Widely used examples include lattice methods such as Lattice-Boltzmann [15, 16, 17, 18, 19] and lattice gas automata [20], as well as particle based approaches such as Dissipative Particle Dynamics [21, 22, 23, 24] and Multi-particle Collision Dynamics [25, 26, 27].

Multi-particle Collision Dynamics (MPC) has received growing attention over the last decade, especially due to the relative ease with which it can be implemented on highly parallelized GPU architectures [28]. It is a particle-based simulation method for hydrodynamic problems, which reproduces Navier-Stokes behaviour on long time and length scales. For dilute and semi-dilute polymer solutions, it yields the correct dynamic behavior as predicted by the Zimm model [29]. First introduced by Malevanets and Kapral in 1999 [25, 26], it has since been extended and applied to a broad variety of physical, chemical and even biological systems, from macromolecules in simple solvents [30] and fluids with complex boundary conditions [31] to viscoelastic fluids [32].

In Multi-particle Collision Dynamics, the fluid is modeled as N point-like particles, each of which corresponds to a volume of the fluid that is big compared to a single solvent molecule but small compared to the system size $V = L_x L_y L_z$. The MPC procedure consists of two consecutive steps, which are repeated at each given time-step of the simulation: a *streaming* step, in which the particles move ballistically and independently of each other, and a *collision* step, in which the particles interact to exchange momentum and thus propagate the hydrodynamic information through the system [20, 33, 34]. In the following, a short description of the algorithm and the variants thereof used in this thesis, is given.

2.7.1 Stochastic Rotation Dynamics

Over the years, many variants of Multi-particle Collision dynamics have been developed. Especially the momentum exchange during the *collision* step can be implemented in different ways. In the work of this thesis, the most common technique, sometimes termed *Stochastic Rotation Dynamics* [35], is employed. It proceeds as follows. During the

streaming step, the position of each fluid particle is propagated in time according to ballistic motion:

$$\boldsymbol{r}_i(t + \Delta t) = \boldsymbol{r}_i(t) + \boldsymbol{v}_i(t)\Delta t \tag{2.17}$$

When employing any type of boundaries in the simulation – such as walls, periodic boundary conditions, etc. –, their effects have to be applied immediately after this step (see Section 2.7.4). In the subsequent *collision* step, the system is spatially divided into N_{cell} cubic cells with lattice constant a and the particles are sorted into these cells according to their current positions. Each cell is then treated independently and particles within a given cell exchange momentum while conserving the total linear momentum, mass and energy of the system. This is achieved by applying a stochastic rotation on the relative particle velocities:

$$\boldsymbol{v}_i(t + \Delta t) = \boldsymbol{v}_i(t) + \left(\mathbf{R}(\beta) - \mathbb{1}\right)\left(\boldsymbol{v}_i(t) - \boldsymbol{v}_{cm}(t)\right)$$
$$= \boldsymbol{v}_{cm}(t) + \mathbf{R}(\beta)\left(\boldsymbol{v}_i(t) - \boldsymbol{v}_{cm}(t)\right) \tag{2.18}$$

where $\boldsymbol{v}_{cm}$ is the center-of-mass velocity of the specific cell, i.e.

$$\boldsymbol{v}_{cm} = \frac{\sum_{i \in \text{cell}} m_i \boldsymbol{v}_i}{\sum_{i \in \text{cell}} m_i} = \frac{1}{N_c} \sum_{i \in \text{cell}} \boldsymbol{v}_i \,, \tag{2.19}$$

where the latter simplification holds only if all particles are of the same mass.

The matrix $\mathbf{R}(\beta)$ describes a rotation around a unit vector $\boldsymbol{b} = (b_x, b_y, b_z)^T$ by the angle β, which is a constant parameter of the algorithm. The rotation axis $\boldsymbol{b}$ is chosen randomly at each step for each cell j by uniformly sampling from a 2-sphere $\mathbb{S}^2$ of radius 1. Two numbers $\phi \in [0, 2\pi]$ and $\vartheta \in [-1, 1]$ are drawn from uniform distributions of the given intervals and then subjected to the following set of transformations, yielding the components b_α of the unit vector $\boldsymbol{b}$

$$b_x = \sqrt{1 - \vartheta^2} \cos \phi \tag{2.20}$$
$$b_y = \sqrt{1 - \vartheta^2} \sin \phi \tag{2.21}$$
$$b_z = \vartheta \tag{2.22}$$

Defining $c = \cos \beta$ and $s = \sin \beta$, the rotation operator takes on the form

$$\mathbf{R}(\beta) = \begin{pmatrix} b_x^2 + (1 - b_x^2)c & b_x b_y(1 - c) - b_z s & b_x b_z(1 - c) + b_y s \\ b_x b_y(1 - c) + b_z s & b_y^2 + (1 - b_y^2)c & b_y b_z(1 - c) - b_x s \\ b_x b_z(1 - c) - b_y s & b_y b_z(1 - c) + b_x s & b_z^2 + (1 - b_z^2)c \end{pmatrix} \tag{2.23}$$

Malevanets and Kapral have found an H-theorem for this algorithm, stating that the equilibrium distribution of particle velocities is Maxwellian as well as that the correct hydrodynamic behaviour is produced [25]. The size a of the cells should reflect a typical shortest length scale of interest in the system. In the case of polymers, it is usually chosen to coincide with the size of a polymer bead or the equilibrium extension of a backbone bond. In this way, on average only one monomer will interact with a specific cell and a sufficient resolution of hydrodynamic interactions is achieved.

2.7.2 Grid Shift

The sorting of particles into cells and their exchanging of momentum introduces correlations between them, which should decay fast to satisfy the assumption of molecular chaos. This is not the case, however, if the particles' mean free path $\lambda = \Delta t \sqrt{k_B T / m}$ is small compared to the lattice constant a of the cells, i.e. for small time-steps or at low temperatures. For $\lambda \ll a$, particles are likely to stay in their current cell and interact with the same collision partners over several simulation steps, leading to the build-up of these correlations. This effect is problematic, because it violates Galilean invariance. This can be illustrated with a simple thought experiment. Consider what happens if we take the view of a moving observer with constant velocity relative to the fluid. This is equivalent to imposing a homogeneous flow field $\mathcal{V}$ on the system: The stronger the velocity gradient of $\mathcal{V}$, the more particles would leave their current cell and enter a new one at each step. This means that the strength of the imposed flow essentially reduces the correlations within different cells. Thus, the transport properties of the system would depend on the flow field $\mathcal{V}$ and Galilean invariance would be destroyed.

To restore Galilean invariance, we have to make sure that particles exchange momentum with a different group at each time step and correlations decay fast. A simple way to achieve this is to shift the sorting grid by a random vector $\boldsymbol{d}$ with components in the interval $[-a/2, a/2]$ at each time-step [34, 35]. Figure 2.2 illustrates this procedure. Note that this is equivalent to shifting the particles in the direction $-\boldsymbol{d}$ before sorting and shifting them back to their original positions after the collision. Due to the random grid shift, particles are now grouped into different collision environments at each time-step and interact with different neighbors, regardless of their mean free path.
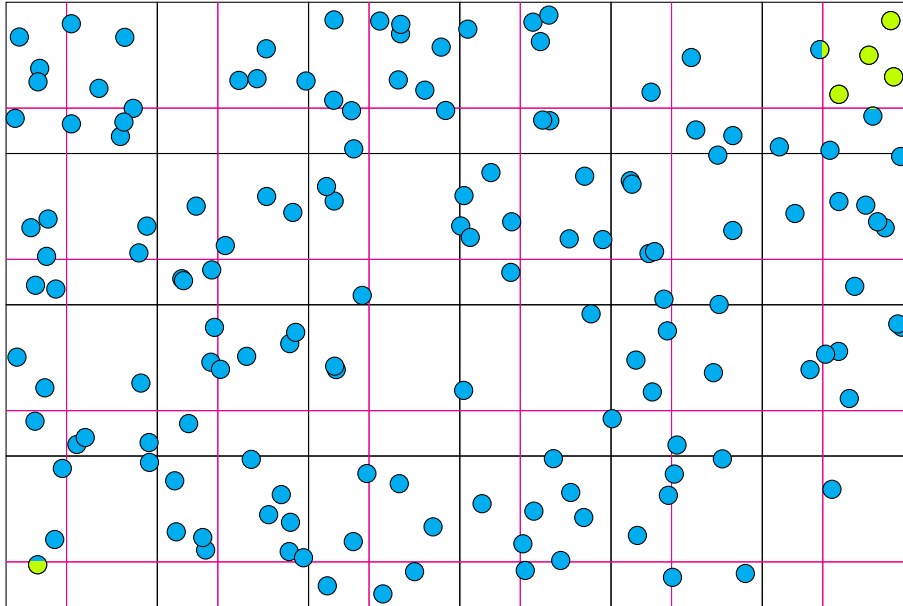
Figure 2.2: Illustration of the grid shift procedure in 2D. Initial cells are coloured black, while cells shifted by the random vector $\boldsymbol{d}$ are coloured purple. The particles belonging to one exemplary box are coloured green to show how boundary conditions are applied. Reproduced from [36]

2.7.3 Maxwell-Boltzmann Scaling Thermostat

The stochastic rotation dynamics variant of MPC conserves energy, mass and volume (see Section 2.7.1), and thus results in statistics corresponding to a microcanonical (NVE) ensemble. However, in the context of this thesis, it is necessary to simulate a canonical (NVT) ensemble, i.e. we want to keep the system at a constant temperature T. Simulations in the canonical ensemble are not only more comparable to experiments, but thermal fluctuations are also necessary to efficiently sample the energy landscape of a system. Furthermore, the presence of external fields, such as the homogeneous shear flow studied in Chapter 4, leads to viscous heating and thus requires a method for controlling the temperature. For the simulations in this work, the *Maxwell-Boltzmann Scaling* thermostat [37], a local cell-level velocity rescaling scheme, was employed. It ensures that within each cell, the set of relative velocities $\{\boldsymbol{v}\} = \{\boldsymbol{v}_{i,cm} | i \in \text{cell}\}$ are distributed according to the Maxwell-Boltzmann distribution

$$P(\{\boldsymbol{v}\}) = \left(\frac{m}{2\pi k_B T}\right)^{3N_c/2} \exp\left(-\frac{m}{2k_B T}\sum_{i\in\text{cell}}\boldsymbol{v}^2_{i,cm}\right), \tag{2.24}$$

where N_c is the number of particles within a given cell. Summing up all possible sets of velocities $\{\boldsymbol{v}\}$ that yield a particular kinetic energy E_k, i.e. $\sum_{i\in\text{cell}}\frac{m_i}{2}\boldsymbol{v}^2_{i,cm} = E_k$, one can

calculate the probability density of the local kinetic energy [38]:

$$P(E_k) = \frac{1}{E_k \Gamma(f/2)} \left(\frac{E_k}{k_b T}\right)^{f/2} \exp\left(\frac{-E_k}{k_b T}\right) \tag{2.25}$$

Here, $f = 3(N_c - 1)$ are the degrees of freedom within a cell and $\Gamma(z)$ denotes the gamma function, $\Gamma(z) = \int_0^\infty x^{z-1} e^{-x} dx$. Note that the probability density converges to a Gaussian function with mean $\langle E_k \rangle = f k_B T/2$ and variance $(\Delta E_k)^2 = f(k_B T)^2/2$ in the limit $N_c \to \infty$.

At each MPC step and for each cell, the particles' relative velocities are scaled by a factor κ to set the kinetic energy of the cell to a new value E_k' sampled from the probability density 2.25:

$$\boldsymbol{v}_{i,cm} \to \kappa \boldsymbol{v}_{i,cm} \qquad \text{with } \kappa = \sqrt{\frac{2E_k'}{\sum_{i \in \text{cell}} m_i \boldsymbol{v}_{i,cm}^2}} \tag{2.26}$$

2.7.4 Boundary Conditions and Shear Flow

A major advantage of the MPCD method is the vast selection of possible boundary conditions that can be implemented with it. These include *slip* [26, 39] and *no-slip boundary conditions* [40], which govern the way in which particles hitting a surface are treated, as well as boundary conditions for simulating the bulk rather than a confined system. Only the latter are used in this work and will be described briefly in the following.

Periodic Boundary Conditions

Periodic boundary conditions are employed in molecular dynamics simulation to address the problem of artificial surface effects stemming from a finite system [41] . To emulate a bulk system, the central box is considered to be replicated periodically along all principal directions, forming an infinite lattice. As such, whenever a particle leaves the central box crossing a particular surface, its image will enter from the opposite surface. Mathematically, this amounts to a mapping of the particle's position $\boldsymbol{r}$ into the central box according to

$$r_j \to r_j' = r_j - \lfloor r_j/L_j \rfloor L_j \qquad \text{for } j \in \{x, y, z\} \tag{2.27}$$

where L_j is the side length of the central box in the j direction. Note that $\lfloor \ \rfloor$ denotes mapping to the largest previous integer (e.g. $\lfloor -0.3 \rfloor = -1$) and as such, this results in a system that has its origin at the lower forward left corner, i.e. $r_j \in [0, L_j)$.

Lees–Edwards Boundary Conditions

Lees–Edwards boundary conditions are a method for introducing shear flow in a system with periodic boundary conditions [42, 9, 32]. The infinite lattice system considered when using periodic boundary conditions is subjected to a uniform shear in the $x - y$ plane with shear rate $\dot{\gamma} = \frac{\mathrm{d}v_x}{\mathrm{d}r_y}$. This means that the layer of boxes whose origins are at $y = 0$ remain stationary, while layers above and below move with a constant velocity of $\boldsymbol{v}_{box} = (\pm\dot{\gamma}L_y, 0, 0)$ in the positive and negative x-direction, respectively (see Figure 2.3). When a particle leaves the central box in the positive y-direction, its image will enter across the opposite surface as in periodic boundary conditions, but with an additional displacement in the x-direction $\mathrm{d}x = -\dot{\gamma}L_y t$, because the layer of boxes below the central layer has moved that amount to the left relative to the central layer. Additionally, the x-component of its velocity will be reduced by $\dot{\gamma}L_y$ compared to the particle that has left the box. In a similar fashion, if the particle leaves the central box in the negative y-direction, its image will enter across the opposite surface with an additional displacement $\mathrm{d}x = +\dot{\gamma}L_y t$, and a velocity increased by $+\dot{\gamma}L_y$. Mathematically, these boundary conditions can be expressed as

$$r_j \rightarrow r_j' = r_j - \lfloor \frac{r_j}{L_j} \rfloor L_j - \delta_{jx} \lfloor \frac{r_y}{L_y} \rfloor \dot{\gamma}L_y t$$
$$v_j \rightarrow v_j' = v_j - \delta_{jx} \lfloor \frac{r_y}{L_y} \rfloor \dot{\gamma}L_y$$

After sufficient equilibration time, this scheme will lead to a linear velocity profile according to

$$v_x(y) = \dot{\gamma} \cdot y \tag{2.28}$$

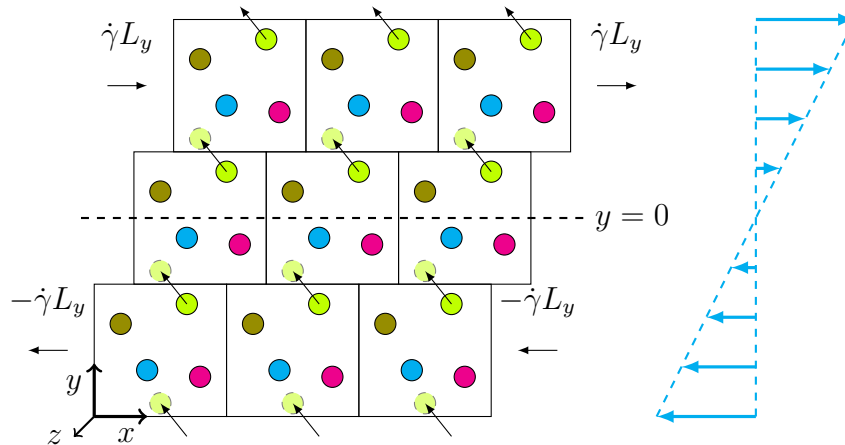Note that periodic boundary conditions are recovered in the case of $\dot{\gamma} = 0$.

Figure 2.3: Lees–Edwards boundary conditions for homogeneous shear flow. The green spheres demonstrate what happens when a particle leaves the central box and boundary conditions are applied. The blue arrows indicate the average velocity profile of the fluid. Reproduced from [36]

2.7.5 Embedded Objects

In this work, we study the effect of shear flow on the properties of dilute and semidilute polymer solutions. To incorporate such macromolecular objects into the MPC algorithm, they simply have to be included as point particles in the *collision* step [30]. For a given cell with N_m monomers of mass M and velocities $\boldsymbol{V}_i$, the calculation of the center-of-mass velocity used in the stochastic rotation (Equation 2.18) has to be modified as follows:

$$\boldsymbol{v}_{cm} = \frac{m \sum_{i \in \text{cell}}^{N_c} \boldsymbol{v}_i + M \sum_{i \in \text{cell}}^{N_m} \boldsymbol{V}_i}{N_c m + N_m M} \tag{2.29}$$

Between successive collisions monomers are propagated in time according to their equations of motion via an integration scheme of time-step Δt_{MD} (such as the velocity-verlet algorithm used in this work), which should be smaller than the time-step Δt of the MPC routine. Furthermore, the average mass of fluid particles per cell should match the mass of a monomer [43], i.e. $M = \langle N_c \rangle m$.

During the stochastic rotation, the embedded particles and the MPC particles exchange momenta. Since the number of MPC particles is orders of magnitude bigger than the number of embedded particles, this interaction is generally strong enough for the MPC particles to act as a heat bath. The introduction of a single thermostat acting on the MPC particles alone is thus sufficient to keep the embedded objects at the desired temperature as well.

References

[1] K. Kremer and G. S. Grest, "Dynamics of entangled linear polymer melts: A molecular-dynamics simulation," *J. Chem. Phys.*, vol. 92, no. 8, pp. 5057–5086, 1990.

[2] M. Rubinstein and R. H. Colby, *Polymer Physics*, vol. 23. Oxford University Press: Oxford, U.K., 2003.

[3] I. Coluzza and C. Dellago, "The configurational space of colloidal patchy polymers with heterogeneous sequences," *Journal of Physics: Condensed Matter*, vol. 24, p. 284111, jun 2012.

[4] I. Coluzza, P. D. J. van Oostrum, B. Capone, E. Reimhult, and C. Dellago, "Sequence controlled self-knotting colloidal patchy polymers," *Phys. Rev. Lett.*, vol. 110, p. 075501, Feb 2013.

[5] I. Coluzza, P. D. J. van Oostrum, B. Capone, E. Reimhult, and C. Dellago, "Design and folding of colloidal patchy polymers," *Soft Matter*, vol. 9, pp. 938–944, 2013.

[6] L. Verlet, "Computer "experiments" on classical fluids. i. thermodynamical properties of lennard-jones molecules," *Phys. Rev.*, vol. 159, pp. 98–103, Jul 1967.

[7] D. Frenkel and B. Smit, *Understanding molecular simulations: from algorithms to applications.* Academic Press, 1996.

[8] D. J. Auerbach, W. Paul, A. F. Bakker, C. Lutz, W. E. Rudge, and F. F. Abraham, "A special purpose parallel computer for molecular dynamics: motivation, design, implementation, and application," *J. Phys. Chem.*, vol. 91, no. 19, pp. 4881–4890, 1987.

[9] M. P. Allen and D. J. Tildesley, *Computer simulation of liquids.* Oxford UP, 1989.

[10] J. A. Izaguirre, D. P. Catarello, J. M. Wozniak, and R. D. Skeel, "Langevin stabilization of molecular dynamics," *J Chem. Phys.*, vol. 114, no. 5, pp. 2090–2098, 2001.

[11] J. G. Kirkwood and J. Riseman, "The intrinsic viscosities and diffusion constants of flexible macromolecules in solution," *The Journal of Chemical Physics*, vol. 16, no. 6, pp. 565–573, 1948.

[12] J. J. Erpenbeck and J. G. Kirkwood, "Statistical mechanics of irreversible processes in polymer solutions," *The Journal of Chemical Physics*, vol. 29, no. 4, pp. 909–913, 1958.

[13] P. E. Rouse, "A theory of the linear viscoelastic properties of dilute solutions of coiling polymers," *The Journal of Chemical Physics*, vol. 21, no. 7, pp. 1272–1280, 1953.

[14] B. H. Zimm, "Dynamics of polymer molecules in dilute solution: Viscoelasticity, flow birefringence and dielectric loss," *The Journal of Chemical Physics*, vol. 24, no. 2, pp. 269–278, 1956.

[15] G. R. McNamara and G. Zanetti, "Use of the boltzmann equation to simulate lattice-gas automata," *Phys. Rev. Lett.*, vol. 61, pp. 2332–2335, Nov 1988.

[16] R. Benzi, S. Succi, and M. Vergassola, "The lattice boltzmann equation: theory and applications," *Physics Reports*, vol. 222, no. 3, pp. 145 – 197, 1992.

[17] A. J. Ladd, "Numerical simulations of particulate suspensions via a discretized boltzmann equation. part 1. theoretical foundation," *Journal of fluid mechanics*, vol. 271, pp. 285–309, 1994.

[18] S. Chen and G. D. Doolen, "Lattice boltzmann method for fluid flows," *Annual Review of Fluid Mechanics*, vol. 30, no. 1, pp. 329–364, 1998.

[19] P. Ahlrichs and B. Dünweg, "Lattice-boltzmann simulation of polymer-solvent systems," *International Journal of Modern Physics C*, vol. 09, no. 08, pp. 1429–1438, 1998.

[20] U. Frisch, B. Hasslacher, and Y. Pomeau, "Lattice-gas automata for the navier-stokes equation," *Phys. Rev. Lett.*, vol. 56, pp. 1505–1508, Apr 1986.

[21] P. J. Hoogerbrugge and J. M. V. A. Koelman, "Simulating microscopic hydrodynamic phenomena with dissipative particle dynamics," *Europhysics Letters (EPL)*, vol. 19, pp. 155–160, jun 1992.

[22] P. Español and P. Warren, "Statistical mechanics of dissipative particle dynamics," *Europhysics Letters (EPL)*, vol. 30, pp. 191–196, may 1995.

[23] R. D. Groot and P. B. Warren, "Dissipative particle dynamics: Bridging the gap between atomistic and mesoscopic simulation," *The Journal of Chemical Physics*, vol. 107, no. 11, pp. 4423–4435, 1997.

[24] M. Ripoll, M. H. Ernst, and P. Español, "Large scale and mesoscopic hydrodynamics for dissipative particle dynamics," *The Journal of Chemical Physics*, vol. 115, no. 15, pp. 7271–7284, 2001.

[25] A. Malevanets and R. Kapral, "Mesoscopic model for solvent dynamics," *J. Chem. Phys.*, vol. 110, no. 17, pp. 8605–8613, 1999.

[26] A. Malevanets and R. Kapral, "Solute molecular dynamics in a mesoscale solvent," *J. Chem. Phys.*, vol. 112, no. 16, pp. 7260–7269, 2000.

[27] A. Lamura, G. Gompper, T. Ihle, and D. M. Kroll, "Multi-particle collision dynamics: Flow around a circular and a square cylinder," *Europhysics Letters (EPL)*, vol. 56, pp. 319–325, nov 2001.

[28] E. Westphal, S. Singh, C.-C. Huang, G. Gompper, and R. Winkler, "Multiparticle collision dynamics: Gpu accelerated particle-based mesoscale hydrodynamic simulations," *Computer Physics Communications*, vol. 185, no. 2, pp. 495 – 503, 2014.

[29] K. Mussawisade, M. Ripoll, R. G. Winkler, and G. Gompper, "Dynamics of polymers in a particle-based mesoscopic solvent," *J. Chem. Phys.*, vol. 123, no. 14, 2005.

[30] A. Malevanets and J. M. Yeomans, "Dynamics of short polymer chains in solution," *Europhys. Lett.*, vol. 52, no. 2, p. 231, 2000.

[31] H. Noguchi and G. Gompper, "Dynamics of fluid vesicles in shear flow: Effect of membrane viscosity and thermal fluctuations," *Phys. Rev. E*, vol. 72, p. 011901, Jul 2005.

[32] B. Kowalik and R. G. Winkler, "Multiparticle collision dynamics simulations of viscoelastic fluids: Shear-thinning gaussian dumbbells," *J. Chem. Phys.*, vol. 138, no. 10, 2013.

[33] G. Gompper, T. Ihle, D. M. Kroll, and R. G. Winkler, *Multi-Particle Collision Dynamics: A Particle-Based Mesoscale Simulation Approach to the Hydrodynamics of Complex Fluids*, p. 1. 2009.

[34] T. Ihle and D. M. Kroll, "Stochastic rotation dynamics. i. formalism, galilean invariance, and green-kubo relations," *Phys. Rev. E*, vol. 67, p. 066705, Jun 2003.

[35] T. Ihle and D. Kroll, "Stochastic rotation dynamics: a galilean-invariant mesoscopic model for fluid flow," *Phys. Rev. E*, vol. 63, no. 2, p. 020201, 2001.

[36] M. Formanek, "Telechelic star polymers under shear flow," Master's thesis, University of Vienna, Wien, 2016.

[37] C. Huang, A. Chatterji, G. Sutmann, G. Gompper, and R. Winkler, "Cell-level canonical sampling by velocity scaling for multiparticle collision dynamics simulations," *J. Comp. Phys.*, vol. 229, no. 1, pp. 168 – 177, 2010.

[38] G. Bussi, D. Donadio, and M. Parrinello, "Canonical sampling through velocity rescaling," *J. Chem. Phys.*, vol. 126, no. 1, p. 014101, 2007.

[39] S. H. Lee and R. Kapral, "Mesoscopic description of solvent effects on polymer dynamics," *J. Chem. Phys.*, vol. 124, no. 21, 2006.

[40] Y. Inoue, Y. Chen, and H. Ohashi, "Development of a simulation model for solid objects suspended in a fluctuating fluid," *J. Stat. Phys.*, vol. 107, no. 1-2, pp. 85–100, 2002.

[41] M. Born and T. von Kármán, "Über schwingungen in raumgittern," *Physikalische Zeitschrift*, vol. 13, no. 297-309, p. 18, 1912.

[42] A. Lees and S. Edwards, "The computer study of transport processes under extreme conditions," *J. Phys. C*, vol. 5, no. 15, p. 1921, 1972.

[43] M. Ripoll, K. Mussawisade, R. G. Winkler, and G. Gompper, "Dynamic regimes of fluids simulated by multiparticle-collision dynamics," *Phys. Rev. E*, vol. 72, p. 016701, Jul 2005.

Chapter 3

Exploring Novel Synthesis Routes: Playing with Precursor Topology and Crowding Conditions

3.1   Introduction

Single-chain nanoparticles are obtained by the formation of irreversible bonds between reactive groups randomly distributed along a linear precursor polymer. The collapse triggered by the cross-linking process is reminiscent of the folding of proteins to their native, functional state and has thus inspired scientists and engineers working in the field to envision a vast range of potential bio-medical applications for SCNPs, such as bioimaging [1, 2], drug delivery [3, 4] and catalysis [5, 6, 7, 8]. For many of these applications, a soft, spherical, well defined structure with accessible cavities or pockets (for the uptake of drugs or reactants), similar to globular proteins, is desirable. Recent studies employing small-angle neutron and X-ray scattering (SANS and SAXS) have elucidated the true morphology of SCNPs synthesized in good solvent conditions and high dilution. They have revealed that, on average, they adopt open, sparse conformations [4, 6, 9, 10], which is demonstrated by the scaling of their size R with their degree of polymerization N as $R \sim N^\nu$, with a scaling exponent of $\nu \approx 0.5$ [11]. This scaling behavior is comparable to that of Gaussian chains in a θ-solvent, but very far from the anticipated limit of globular spherical objects ($\nu = 1/3$). Computer simulations have not only reproduced this result with a very simple non-specific bead-spring model, but also discovered the underlying mechanism for the prevalence of sparse topologies [10]. The self-avoiding conformations adopted by the precursors under good solvent conditions promote the formation of cross-links between reactive monomers separated by short contour distances. Long-range loops, on the other hand, occur very infrequently as they require large reorientations of the precursor chain. Thus, the distribution resulting from the stochastic cross-linking process is dominated by sparse topologies, characterized by local compact domains separated by flexible segments [10, 12]. These typical morphologies are sometimes referred to as a "pearl necklace" or "rings-on-a-chain". Computer simulations have furthermore proposed various alternative synthesis routes to tackle this problem and improve control over SCNP size and shape (Figure 3.1), a few of which shall be discussed in the following.

Orthogonal and multi-orthogonal synthesis involves the incorporation of 2 or more distinct chemical reactive groups in the precursor molecule. These x orthogonal species can only form bonds with others of the same type. Given that all reactive groups are distributed randomly along the precursor backbone, an increasing number x of different chemical species leads, for the same fraction f of total functional groups, to an increase in the average contour distance separating two reactive groups of the same type. As such, in principle, the formation of long-range loops should be enhanced without compromising on the degree of local compaction. However, significant improvements in size and morphology
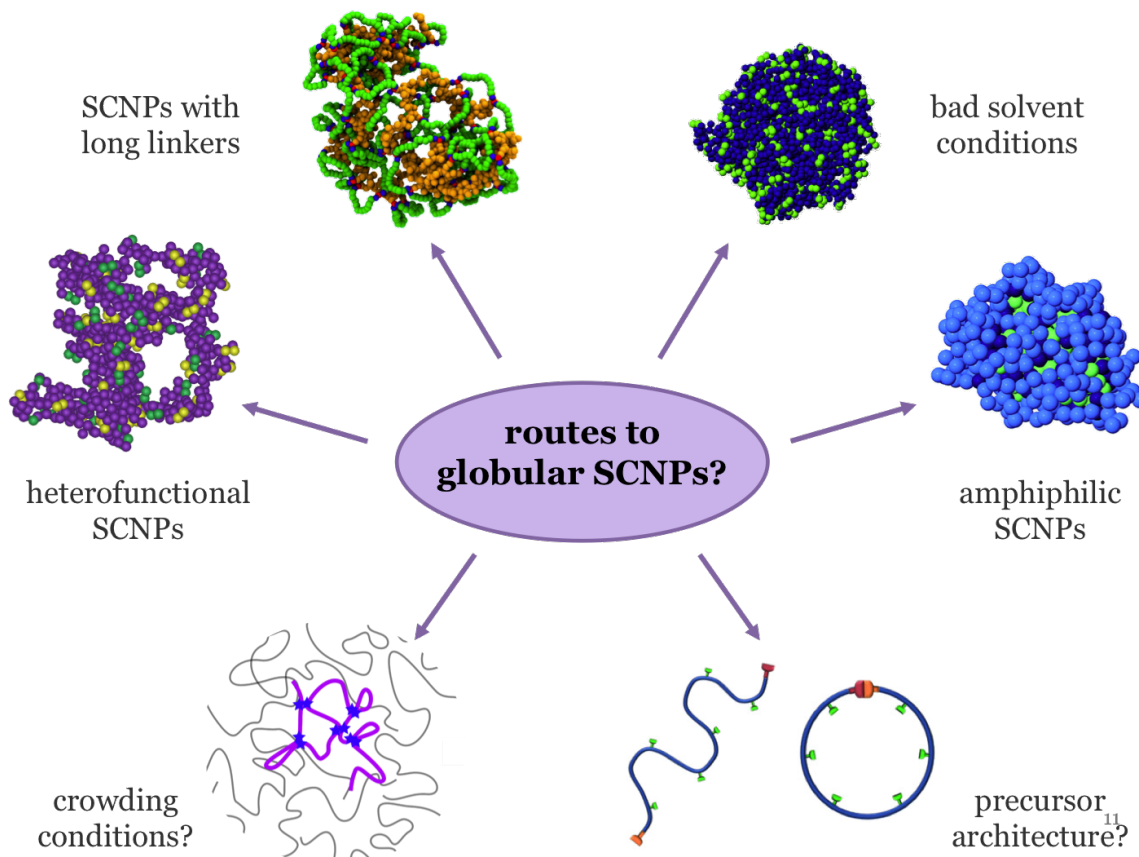
Figure 3.1: Different synthesis routes for achieving globular SCNPs as proposed by simulations. Figures adapted and reproduced from [12, 13, 14, 15]

could only be achieved for $x \geq 4$ [10, 12]. Experimental realization of precursors with such orthogonal functionality is highly nontrivial and thus far only SCNPs with $x = 3$ have been successfully synthesized [16].

A second route involves a change in the precursor architecture. It relies on the use of flexible linker segments, whose ends can cross-link with reactive species along the precursor backbone. The model employed in the simulation was based on the simultaneously explored experimental system of SCNPs synthesized via photoactivated thiol-ene and thiol-yne coupling reactions [13]. The dangling linkers are able to efficiently explore a big part of the space occupied by the backbone and thus increase the probability of forming long-range loops. Both computer simulations and SAXS experiments have confirmed this assumption and have shown that the resulting SCNPs adopt more spherical conformations with a decreased scaling exponent of $\nu = 0.41$ [13] compared to standard SCNPs.

Finally, two experimentally accessible synthesis routes that involve the tuning of solvent conditions have been proposed. These routes need to prevent aggregation of the

precursors in bad solvent. Aggregation (and, as a consequence, intermolecular cross-links) is indeed unavoidable at any concentration of experimental interest (even so low as 0.1 mg/ML) if the precursors move freely in the bad solvent.

In the first route, inspired by the Merrifield synthesis using solid supports [17], the precursor is anchored to a solid substrate at a low surface density and the cross-linking process is performed under bad solvent conditions. This induces a collapse of the precursor chain, bringing reactive groups separated by long contour distances close to each other in space and thus enabling the formation of long-range bonds. Anchoring to the surface prevents aggregation and occurrence of intermolecular cross-links. Furthermore, the resulting SCNPs are globular objects in the swollen state, i.e., after cleaving them from the surface and returning them to a good solvent. Their compactness can be tuned by the fraction of reactive groups present in the precursor [14].

The second approach employs an amphiphilic precursor chain with inert solvophilic and reactive solvophobic monomers. The amphiphilicity of the precursor leads to the formation of a core-shell particle, with the bonded solvophobic groups lying buried within an outer layer of solvophilic chain segments, preventing aggregation and intermolecular cross-links. Interestingly, the morphology of these core-shell nanoparticles is governed by the specific placement of the different monomer types. A random distribution of solvophobic and solvophilic groups yields spherical structures, while a regular placement results in elongated worm-like configurations [14]. The SCNP retains the former shapes in the swollen state, i.e., when it is transferred to a solvent of good quality for both kinds of monomers. Recently, this protocol has been experimentally realized in metallo-folded SCNPs from an amphiphilic random copolymer precursor [18].

Here, we propose two novel synthesis routes: (i) changing the precursor architecture, namely by using ring polymers, and (ii) carrying out synthesis under crowding conditions, as well as a combination of both (ring precursors under crowding). This idea emerges from previous studies that investigated the effect of purely steric crowders on the conformations of fully cross-linked SCNPs. It was found [19, 20] that increasing the concentration of the solution beyond the overlap concentration led to the collapse of the SCNPs to crumpled globular structures [21] (reminiscent of ring polymer melts [22]). This is very different from the well-known collapse to Gaussian random-walk conformations experienced by linear chains, and crumpling was found even for the most sparse topologies of the SCNPs [19]. Therefore, by exploiting the former scenario, in this novel route a low fraction of precursor molecules of either linear or ring architecture is cross-linked in the presence of

inert crowders of the same architecture. We investigate the effect of the steric crowding by analyzing, in dilute solution, after removing the crowders, the size and shape distributions as well as the scaling behaviour of the resulting topologically polydisperse set of SCNPs. We find that ring precursors are promising candidates for achieving globular morphologies already when synthesized at high dilution. Furthermore, the ring SCNPs retain, in dilute conditions, the crumpled globular conformations adopted by their precursors under crowding conditions.

3.2 Simulation Details

The precursor molecules as well as the synthesized SCNPs are modeled according to the coarse-grained bead-spring model introduced in Chapter 2.2. The linear precursor molecules consist of $N = 160$ monomers, whereas the ring precursors are made up of $N = 250$ monomers. This degree of polymerization is chosen such that the linear and ring precursors adopt the same radius of gyration at high dilution, i.e. $R_g \approx 10\sigma$, and thus allow a comparison of the size and shape characteristics across the different precursor architectures. The fraction of reactive groups, $f = N_r/N$, is the same for both architectures, which corresponds to $N_r = 40$ for linear chains and $N_r = 62$ for rings. The reactive groups are distributed randomly across the polymer contour, with the only constraint being that at least one inert monomer has to separate two functional groups, in order to prevent trivial cross-links between monomers that are already bonded along the backbone.

We perform Langevin dynamics simulations at a fixed temperature of $T = \epsilon/k_B = 1$, with a time-step of $\Delta t = 0.01\sigma(m/\epsilon)^{1/2}$ and a friction coefficient of $\gamma = 0.5$. For details of the theory and implementation of the algorithm the reader is referred to Chapter 2.6.

The simulation protocol consists of the following steps which are schematically illustrated in Figure 3.2:

(a) First, the reactive precursors are constructed (here a chain, colored in purple). A fraction f of their monomers are randomly replaced by reactive groups (represented by yellow stars), but these cannot form cross-links yet.

(b) Next, in each independent run, two of these inactive precursors are placed in a box of fixed volume $V = L^3 = (100\sigma)^3$ together with inert, purely steric crowders of the
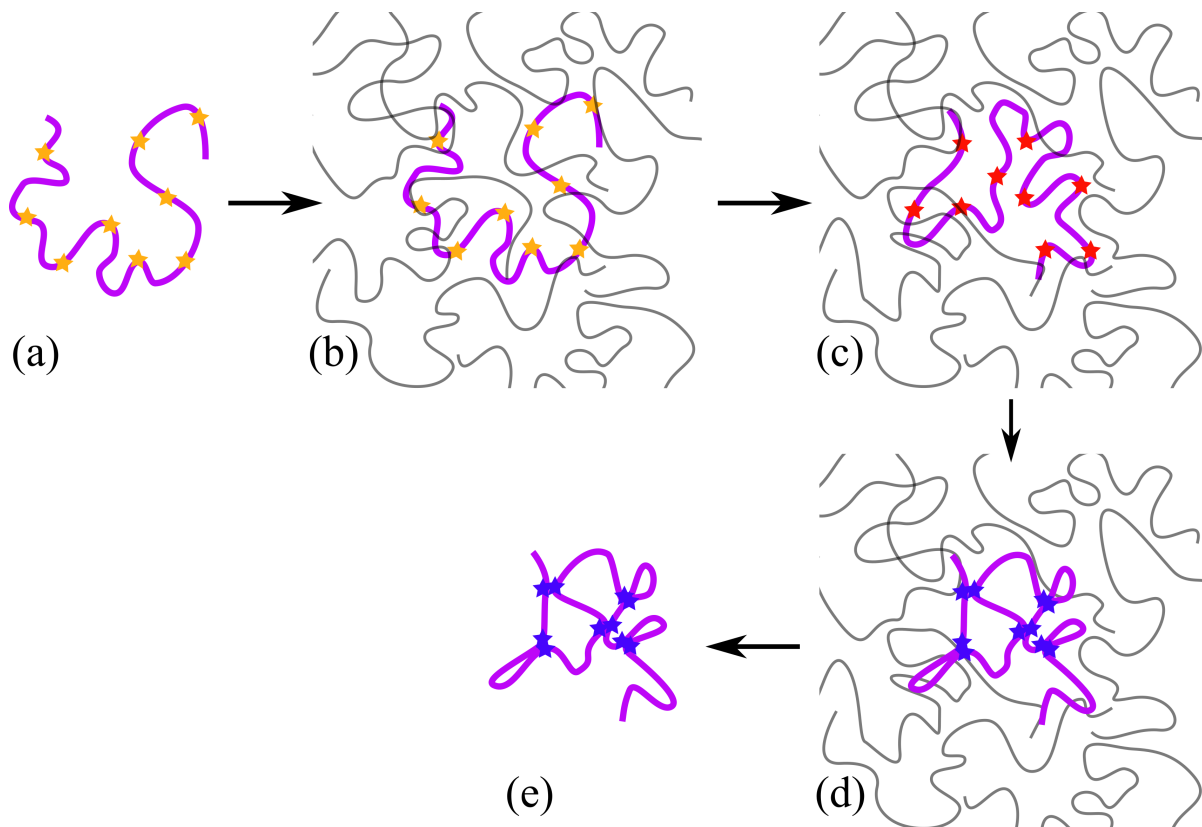
Figure 3.2: Schematic illustration outlining the simulation protocol of synthesizing SCNPs under crowding conditions. (a) The precursor molecule is decorated with reactive monomers. (b) The inactive precursor molecule is surrounded by a solution of purely steric crowders of the same architecture. (c-d) After equilibration, the cross-linking process starts. (e) After all cross-links are formed, the crowders are removed and the SCNP is equilibrated at high dilution.

same polymer architecture at the desired crowding density (here chains are depicted, but the protocol is identical for ring polymers). The concentration of precursor molecules is comparable to that used in the standard synthesis protocol. In the case of rings, we prevent concatenations by initially constructing them as planar objects and stacking them perpendicular to the plane of monomers comprising one ring.

(b-c) The mixture of inactive precursor molecules and crowders is now propagated in time according to Langevin dynamics for several million steps, while we monitor static properties such as the potential energy and the radius of gyration to ensure the system has reached equilibrium.

(c-d) After equilibration, the cross-linking process is started in the precursor molecules by activating the reactive groups (red stars). In experiments, this can be achieved, for example, via photo-activated Diehls-Alder click reaction [23]. The reactive groups are now able to form cross-links (blue stars) as described in Chapter 2.3. Briefly, these cross-links are monofunctional and irreversible and are formed whenever two unbonded reactive

monomers are separated by less than the capture distance $r_c = 1.3\sigma$. We monitor the number of cross-links present in the system over time and stop the simulation once all possible links have been formed.

(d-e) After the cross-linking procedure has completed, we remove the purely steric crowders and simulate the synthesized SCNPs at infinite dilution ($\rho \to 0$) in the "swollen" state. This is done in order to compare their structural properties to those SCNPs synthesized according to the standard protocol under high dilution. Furthermore, all synthesized SCNPs are simulated in the swollen state simultaneously by coupling them to the same Langevin thermostat to limit temperature fluctuations and provide efficient thermalization, but intermolecular interactions are switched off. After equilibration in the swollen state, the simulations are extended further over several million steps in order to accumulate configurations for the statistical time averages.

We simulate three monomer densities of crowding molecules, $\rho = NN_c/V = \{0.1, 0.2, 0.3\}$, where N is the number of monomers per polymer and N_c is the number of polymers present in the system. These values correspond to approximately 5, 10 and 15 times the overlap concentration for both polymer architectures, respectively. The overlap concentration ρ^* is defined as the point where the concentration of monomers in the system equals the concentration of monomers of a single polymer within the space occupied by it at $\rho \to 0$, estimated by a box whose side lengths are given by the diameter of gyration D_{g0} of the polymer, i.e. $\rho^* = N/\langle D_{g0}\rangle^3 \approx 0.02$.

We perform 100 independent simulation runs for each of the three crowding densities considered, leading to the synthesis of 200 SCNPs at each density. Intermolecular cross-links occurred, at most, in 2 of the 100 independent simulations, and can thus be seen as negligible in experiments. These aggregated SCNPs were excluded from the subsequent statistical analysis. Furthermore, it should be noted that in the case of ring polymers, despite being initially non-concatenated, it is possible that the formation of intramolecular cross-links results in concatenations between SCNPs and non-reactive rings (Figure 3.3 represents an example). This phenomena stems from the intrinsic behavior of semidilute ring polymer solutions, in which the rings still exhibit significant interpenetration albeit adopting compact crumpled globular conformations [22]. If a cross-link is formed while a reactive and a non-reactive ring are interpenetrating each other, a concatenation can develop. A few of these cases ($\sim 2\%$) were found by visual inspection of the crowder molecules in the vicinity of a synthesized SCNP and they were excluded from the statistical analysis as well.
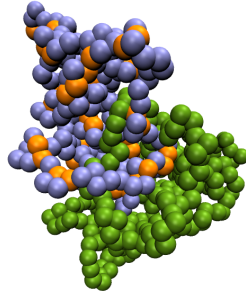
Figure 3.3: Example of a concatenation of a ring SCNP (blue, reactive monomers colored in orange) with a non-reactive ring polymer (green) due to the two rings interpenetrating each other in the region where a cross-link is formed.

3.3 Results and Discussion

3.3.1 Precursor solutions

We first characterize the conformations adopted by the mixture of precursors and crowding molecules after equilibration but before the cross-linking procedure has started (at this stage, SCNP precursors and crowders are equivalent). To this end we calculate their intramolecular form factor,

$$w(\mathbf{q}) = \left\langle \frac{1}{N} \sum_{j,k} \exp\left[i\mathbf{q} \cdot (\mathbf{r}_j - \mathbf{r}_k)\right] \right\rangle, \tag{3.1}$$

where $\mathbf{q}$ is the wave vector and the sum is restricted over monomers belonging to the same SCNP. For isotropic systems without a particular distinction between different directions, the form factor reduces to:

$$w(q) = \left\langle \frac{1}{N} \sum_{j,k} \frac{\sin(qr_{jk})}{qr_{jk}} \right\rangle, \tag{3.2}$$

where $r_{jk} = \| \mathbf{r}_j - \mathbf{r}_k \|$ is the euclidean distance between monomers j and k. For any fractal, and thus for any polymer, the form factor is expected to scale as [24]:

$$w(q) \sim q^{-1/\nu} \quad \text{for} \ \ 1/R_g \lesssim q \lesssim 1/b, \tag{3.3}$$

where b denotes the bond length. This scaling exponent coincides with the power-law scaling of a polymer's size with its polymerization degree and characterizes its fractal
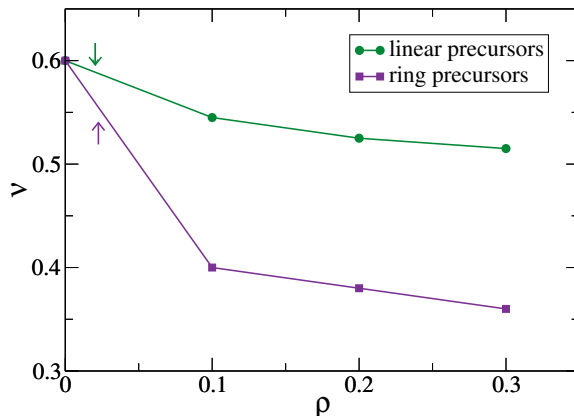
Figure 3.4: Scaling exponents of the two different polymer architectures at densities ranging from $\rho = 0$ to $\rho = 0.3$. Arrows indicate the overlap density $\rho^* = N/\langle D_{g0} \rangle^3$.

dimension. Smaller wavelengths $q < 1/R_g$ contain information about the size of the polymer, whereas bigger wavelengths $q > 1/b$ probe the fluctuations of bonds.

Figure 3.4 depicts the scaling exponents ν of the polymers at various densities, which are calculated from fits of the form factors according to Equation 3.3. At infinite dilution both the linear chains and the rings adopt the expected Flory exponent $\nu \approx \nu_{\mathrm{F}} \approx 0.59$ of self-avoiding polymers in good solvent conditions. At the highest density considered, $\rho = 0.3$, the linear chains approach the scaling exponent of Gaussian chains with $\nu = 0.5$ as expected for linear polymer melts [25, 24]. The ring polymers, on the other hand, reach a scaling exponent of $\nu = 0.36$, which is consistent with former simulations of ring polymer melts [22, 26, 27]. Thus, we can assume that the concentration of crowding molecules is high enough for the ring precursors to adopt highly collapsed conformations and form crumpled globules.

3.3.2 Size and shape parameters

After crosslinking the precursors under varying degrees of crowding conditions, we remove the crowders and simulate them in the swollen state. Following an equilibration period, we save the conformations every 50000 steps, a time during which two subsequent configurational states become completely uncorrelated, and use the accumulated conformations to calculate time averages of individual SCNP topologies (in the following always denoted by angular brackets, i.e $\langle \ldots \rangle$). To characterize the size and shape of the synthesized SCNPs in the swollen state, we calculate the gyration tensor [28],

$$G_{\alpha\beta} = \frac{1}{N^2} \sum_{i=1}^{N} (r_{i\alpha} - r_\alpha^{\mathrm{cm}})(r_{i\beta} - r_\beta^{\mathrm{cm}}) \quad \alpha, \beta = \{x, y, z\}, \tag{3.4}$$

where $r_{i\alpha}$ denotes the α-th Cartesian component of the position of monomer i, and r_α^{cm} is the same Cartesian component of the center-of-mass of the polymer. Diagonalization yields the eigenvalues $\lambda_1 \geq \lambda_2 \geq \lambda_3$ and eigenvectors $\boldsymbol{w}_1$, $\boldsymbol{w}_2$, $\boldsymbol{w}_3$ of the gyration tensor, which define a solid ellipsoid with the same inertial properties as the polymer. From these we calculate the radius of gyration, which corresponds to the square-root of the trace of the gyration tensor, i.e.:

$$R_g = \sqrt{\mathrm{Tr}(G)} = (\lambda_1 + \lambda_2 + \lambda_3)^{\frac{1}{2}} \ , \tag{3.5}$$

and the asphericity parameter, which is given by [29, 30, 31]

$$a = \frac{(\lambda_2 - \lambda_1)^2 + (\lambda_3 - \lambda_1)^2 + (\lambda_3 - \lambda_2)^2}{2(\lambda_1 + \lambda_2 + \lambda_3)^2} \ . \tag{3.6}$$

It ranges from 0 for objects with spherical symmetry to 1 for a 1-dimensional object ($\lambda_2 = \lambda_3 = 0$).

Our choice to use the asphericity as a way to characterize the changes in shape of the SCNPs is motivated by Ref. [19], in which the authors showed that the asphericity exhibits a strong correlation with the internal fluctuation of the SCNP, defined as:

$$\delta = \left(\frac{\langle R_{\mathrm{g}}^2 \rangle - \langle R_{\mathrm{g}} \rangle^2}{\langle R_{\mathrm{g}}^2 \rangle} \right)^{\frac{1}{2}} \ . \tag{3.7}$$

Since the internal mobility reflected by δ is relevant in the context of potential functionality, this correlation indicates a connection between shape and function. As can be clearly seen in Figure 3.5, we find such a correlation as well for SCNPs synthesized under crowding conditions from both linear chains and ring precursors. Furthermore, we find that SCNPs synthesized from ring polymer precursors are generally less deformable – i.e they exhibit smaller δ – than those synthesized from linear chains.

Ideally, we expect that the collapse of the precursors under crowding conditions, as evidenced by the decrease in the scaling exponents with increasing density of crowders (see Figure 3.4), leads to the synthesis of on average smaller and more spherical nanoparticles. Since the cross-linking procedure remains a stochastic process, however, the resulting SCNPs will still be topologically and structurally polydisperse. Thus, we calculate every characteristic for each individual SCNP separately as a time-average and we investigate the change in the distributions instead of calculating ensemble averages.
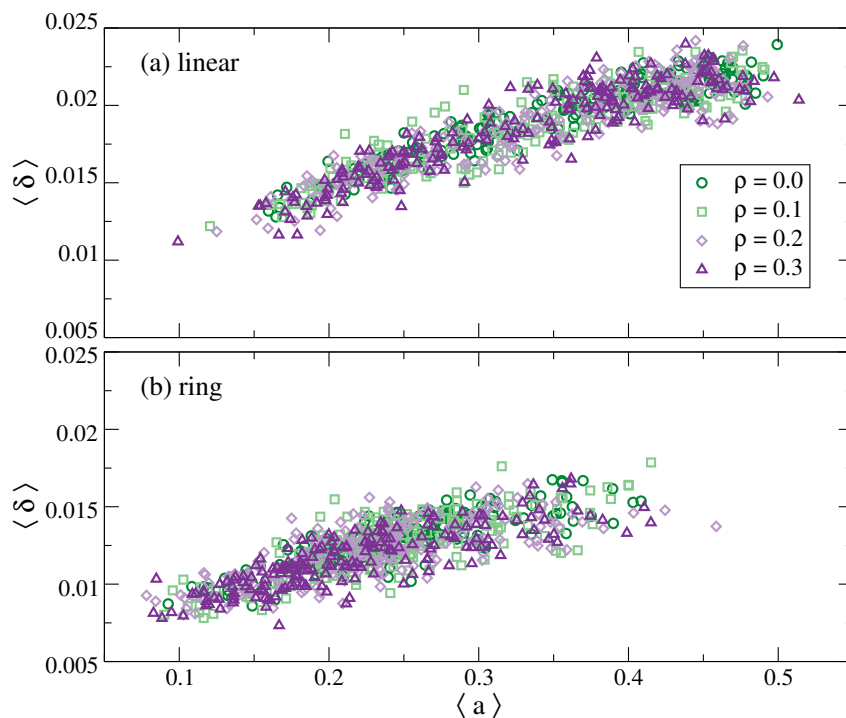
Figure 3.5: Relative fluctuation δ, at infinite dilution, of SCNPs versus their asphericity a, for SCNPs synthesized from linear (a) and ring (b) precursors at various densities.
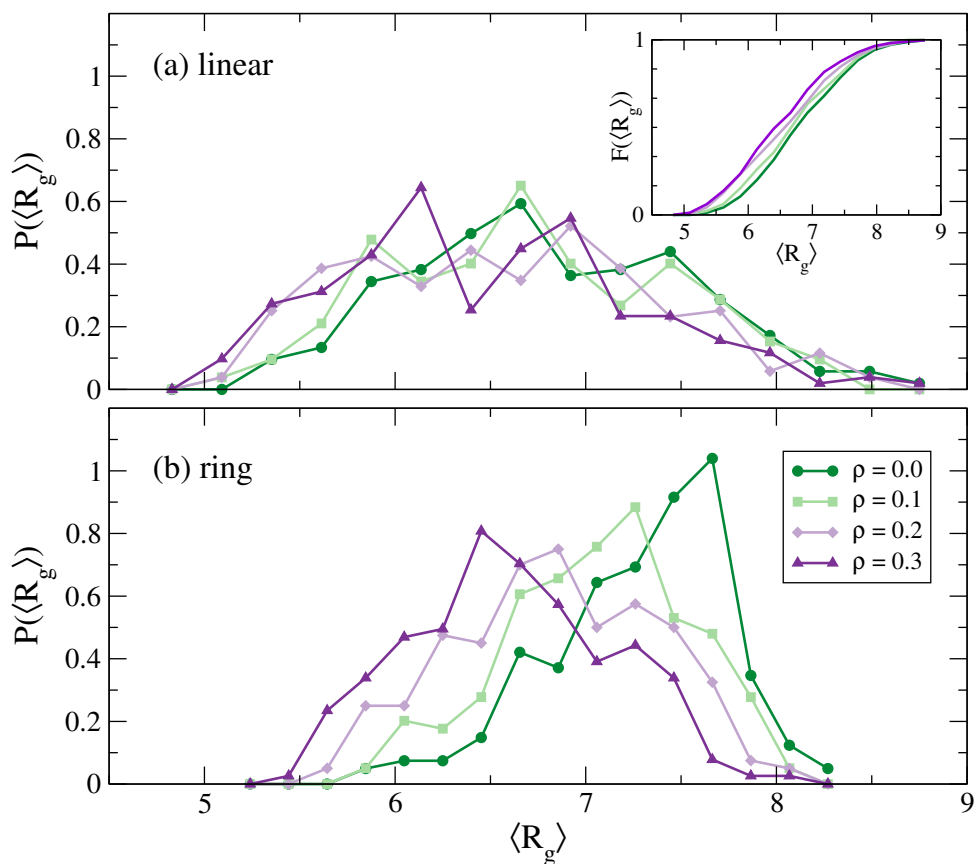

Figure 3.6: Distribution of radius of gyration R_g, at infinite dilution, for SCNPs synthesized from linear (a) and ring (b) precursors at various densities. The inset shows the cumulative distribution function for the linear case.

The resulting distribution of the radius of gyration $\langle R_g \rangle$ is depicted in Figure 3.6 for both SCNPs synthesized from linear or ring precursor molecules. In the case of the chains, no visible trend emerges from the distribution of sizes upon increasing the density of the synthesis conditions. However, when we represent the data as a cumulative distribution, a slight drift towards lower $\langle R_g \rangle$ becomes visible (Figure 3.6(a), inset). Looking at the case of ring polymer precursors, we are presented with a very different picture: The maximum of the distribution clearly shifts towards lower values of $\langle R_g \rangle$ and is accompanied by a reduction of the asymmetry of the distribution. Furthermore, comparing chain and ring precursors, we find that, independent of crowding density, using ring precursor yields a narrower size distribution with more pronounced maxima.
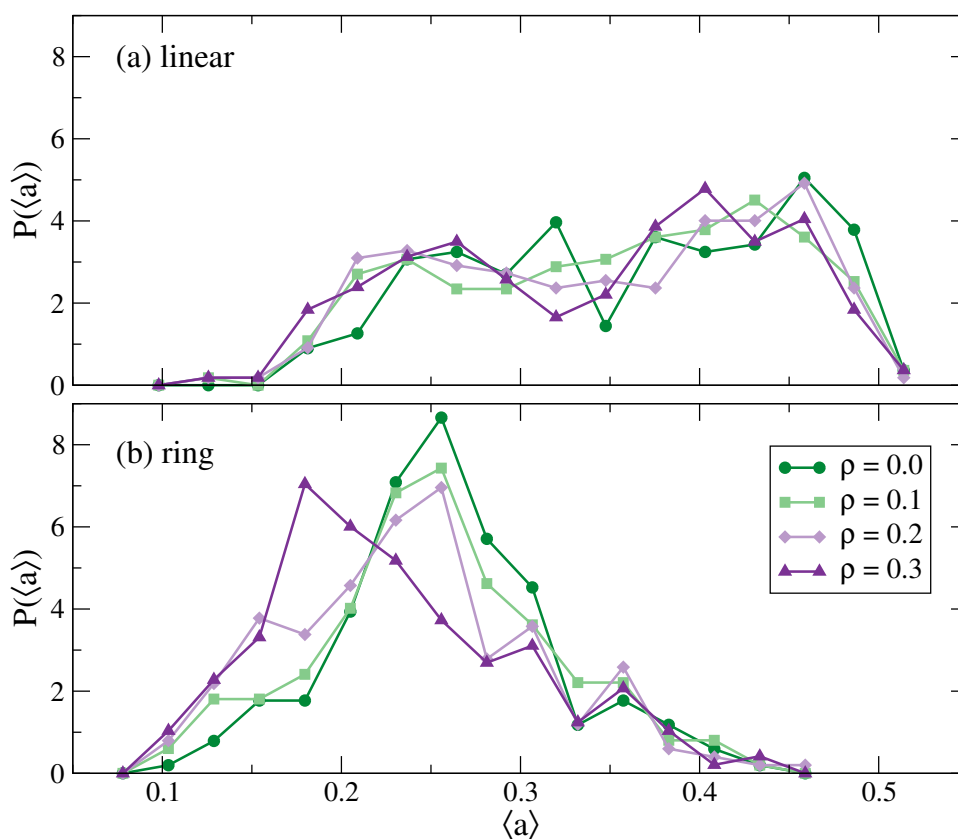

Figure 3.7: Distribution of asphericities a, at infinite dilution, for SCNPs synthesized from linear (a) and ring (b) precursors at various densities.

Figure 3.7 displays the distribution of asphericities for linear and ring SCNPs. We find that the reduction in size of the ring SCNPs is accompanied by a shift in the maximum of asphericity towards lower values, i.e. they adopt more spherical conformations. Surprisingly, this is only observed for the highest density ($\rho = 0.3$), while the shift in the $\langle R_g \rangle$ evolves more gradually. For the linear SCNPs, the distribution of asphericity exhibits no

significant change. It should be noted that both shape parameters, $\langle R_g \rangle$ and $\langle a \rangle$, exhibit a very broad distribution across all densities and for both precursor topologies, whose width is not significantly affected even when the maxima shift. This demonstrates clearly the intrinsic structural and topological polydispersity of SCNPs, which appears to be preserved when employing crowding conditions to carry out their synthesis. To illustrate this further, we include snapshots of representative conformations of SCNPs taken from the upper and lower end of the asphericity distribution (Fig. 3.8).
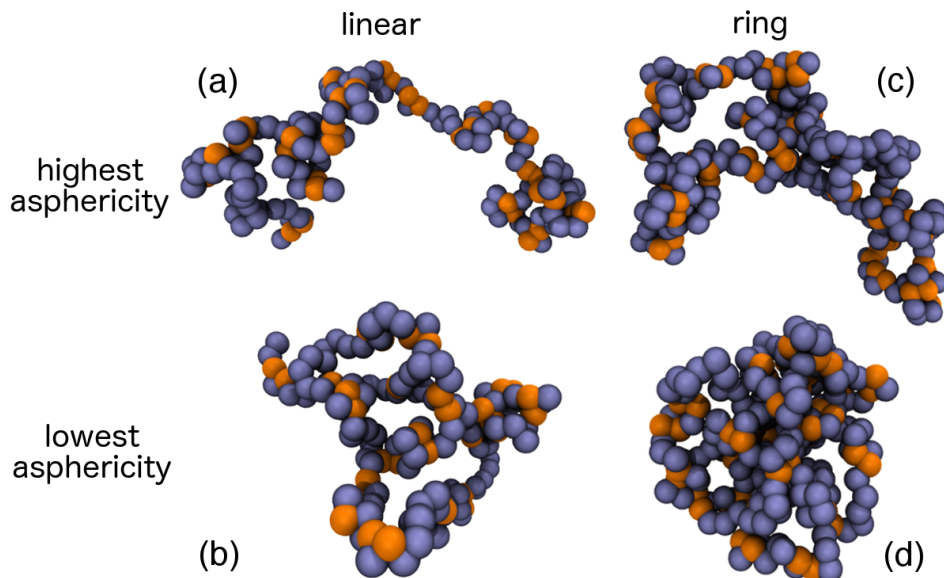

Figure 3.8: Representative snapshots, at infinite dilution, of SCNPs synthesized from linear (a, b) and ring precursors (c, d) at a density of $\rho = 0.3$. The selected SCNPs belong to the 10% with the highest (a, c) and the 10% with the lowest (b, d) asphericity. Cross-linked reactive monomers are coloured in orange.

3.3.3 Form factors and scaling behaviour

We further characterize the average structure of the synthesized SCNPs in the swollen state after removing the crowders by calculating their intramolecular form factors as introduced in Section 3.3.1, Equation 3.1. We fit these to a power law, according to $w(q) \sim q^{-1/\nu}$, in the fractal regime, $1/R_g \lesssim q \lesssim 1/b$. The obtained scaling exponents for linear and ring SCNPs are presented in Figure 3.9 as a function of density. Comparing these with those of the precursors (Figure 3.4), we would like to emphasize that the intramolecular structure of the SCNPs synthesized from different precursors differ already when employing the standard synthesis protocol, i.e. synthesizing at high dilution ($\rho \rightarrow 0$), even though their precursors exhibit the same self-avoiding scaling behavior with

the Flory exponent of $\nu \approx \nu_F = 0.59$. Furthermore, increasing the degree of crowding upon synthesis causes a significant decrease of the scaling exponents for both precursor topologies, albeit having a stronger effect on ring SCNPs. These decreasing values of ν signify that the internal structures of the synthesized SCNPs are on average more compact than those of traditionally synthesized SCNPs at $\rho \to 0$.
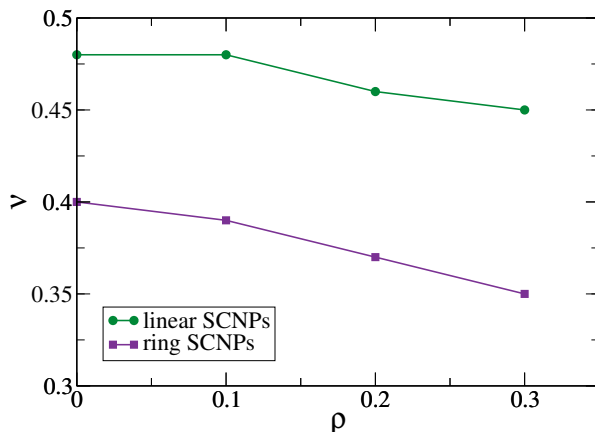

Figure 3.9: Scaling exponents of the whole ensemble of swollen ($\rho = 0$) SCNPs synthesized from either linear (green) or ring (purple) polymer precursors at densities ranging from $\rho = 0$ to $\rho = 0.3$.

The scaling exponent obtained for the linear SCNPs at $\rho \to 0$, $\nu = 0.48$, is comparable to that of linear polymers in melts or θ-solvents ($\nu = 1/2$). This result can be understood in terms of the self-avoiding character of the precursor chain in good solvent conditons and high dilution, which favors the formation of bonds across small contour distances. While leading to local compaction of the polymer, such bonds fail to collapse the chain on a bigger scale. As has been previously established in References [10, 12], long-range cross-links are necessary for an efficient global compaction of SCNPs. The formation of such bonds constitutes an infrequent event in linear SCNPs, occurring mostly towards the end of the simulation between some of the last as-of-yet unlinked reactive groups, which happen to be located at a great distance from each other. Large reorientations of the polymer are necessary to bring these last free reactive groups into contact, which also accounts for the long-time tail in the time-dependent number of unlinked reactive groups $C(t)$ discussed later (Figure 3.12).

Although good solvent conditions and high dilution lead to the same self-avoiding behavior for ring polymers, their intrinsic topology renders cross-linking over long contour distances much more likely. Consequently, SCNPs synthesized from ring polymers adopt a lower scaling exponent, $\nu \approx 0.4$, than their linear counterparts under the same conditions and for the same R_g of their precursors.

Upon increasing the density of crowder molecules present during synthesis, the resulting SCNPs of both precursor architectures undergo a small but persistent decrease in their scaling exponents. Taken together with the changes in the distributions of the radius of gyration and the asphericity, these results provide convincing evidence that employing crowding conditions leads to the synthesis of, on average, more compact and spherical SCNPs than can be achieved in high dilution. Interestingly, apart from the case of $\rho \to 0$, the ring SCNPs essentially retain, in the swollen state, the scaling exponents displayed by their ring precursors at the corresponding densities at which the synthesis took place (compare Figures 3.4 and 3.9). This surprising finding suggests an analogy between the crumpled globular state of ring polymers in a melt ($\nu \gtrsim 1/3$) and the cross-linked conformation of a ring SCNP in dilute conditions. The crumpled globular conformations exhibited by rings in concentrated solutions are characterized by each subchain of the ring condensing independently in itself, effectively reducing entanglements and interpenetrations [21, 32, 33]. One may argue that this collapse behavior allows the precursor to fully cross-link all reactive groups without the need for large reorientations as in the case of linear precursors. If this is the case, the establishment of permanent bonds in the SCNP would essentially "freeze" the polymer in a typical conformation of its precursor at the particular conditions present during the synthesis. Given that the total number of reactive groups is big enough, this would explain why the SCNP is able to retain the crumpled globular conformation even in the swollen state, after removing the crowders.

If this assumption holds true, the formation of cross-links involving groups separated by long contour distances is expected to happen throughout the whole simulation as opposed to primarily towards the end of the synthesis process, as is the case for linear SCNPs [10]. To test this expectation, we plot the probability $P(s)$ of bonded reactive groups being separated by a particular contour length $s = |i - j|$[1] at different times throughout the cross-linking process (Figure 3.10). At the latest time represented, all possible cross-links had been formed. While $P(s)$ is a monotonically decreasing function of s at all times for SCNPs synthesized from linear precursors, over time it evolves towards a plateau at large contour distances for ring SCNPs. For small $s \lesssim 10$, the time evolution of the bond probability exhibits qualitatively the same behavior for both precursor architectures and crowding densities. However, we observe large qualitative differences at large

---

[1]Note that for rings, the periodicity of the topology has to be taken into account and s is bounded by $N/2$. As such, for rings, the contour distance is given by:

$$s = \begin{cases} |i - j| & \text{if } |i - j| \leq N/2 \\ N - |i - j| & \text{else} \end{cases} \tag{3.8}$$
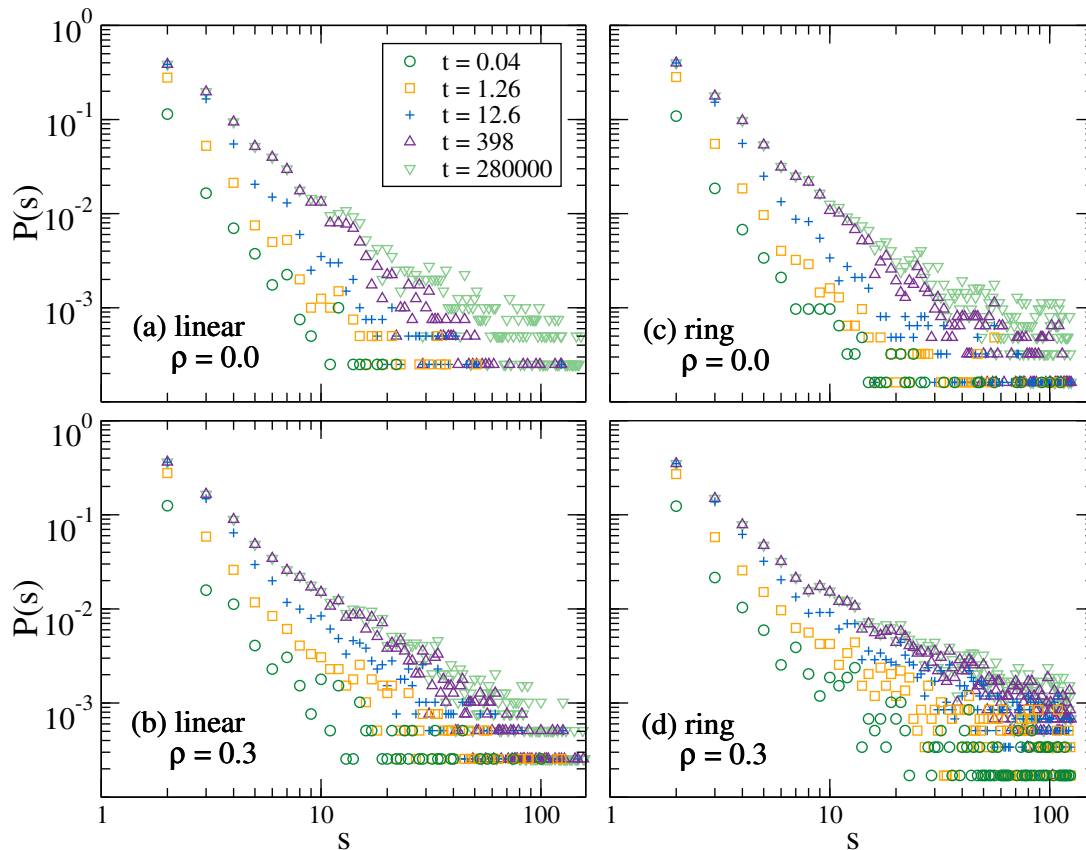
Figure 3.10: Time evolution of the histogram of contour distances s between bonded reactive groups, for the SCNPs synthesized from linear precursors at infinite dilution (a) and $\rho = 0.3$ (b), as well as of SCNPs synthesized from ring precursors at infinite dilution (c) and $\rho = 0.3$ (d). Different data sets correspond to different selected times (see legend). At the latest time (light green), all SCNPs were fully cross-linked.

contour distances between chain and ring precursors. In the linear precursors, bond formation beyond $s \gtrsim 40$ is only encountered in significant amounts after $t \sim 400$, whereas a small number of them can be detected in ring precursors right from the beginning of the cross-linking process. Their growth is strongest, however, during an intermediate regime $0.04 \lesssim t \lesssim 400$. These results support our theory that the collapse to crumpled globules of the ring precursors in the presence of purely steric crowders allows for the efficient formation of bonds across long contour distances and thus leads to the fully-formed ring SCNP retaining the structural characteristics of the crumpled globular state in high dilution.

Since the synthesized SCNPs display a high topological and structural polydispersity, in the following we divide them into subsets of similar asphericities to analyze their conformations separately and have a closer look at the structural features exhibited by the 10% most and 10% least globular SCNPs.

In Figure 3.11, we compare the form factors of these two subsets for linear (left column) and ring (right column) SCNPs, synthesized at infinite dilution (top row) and the
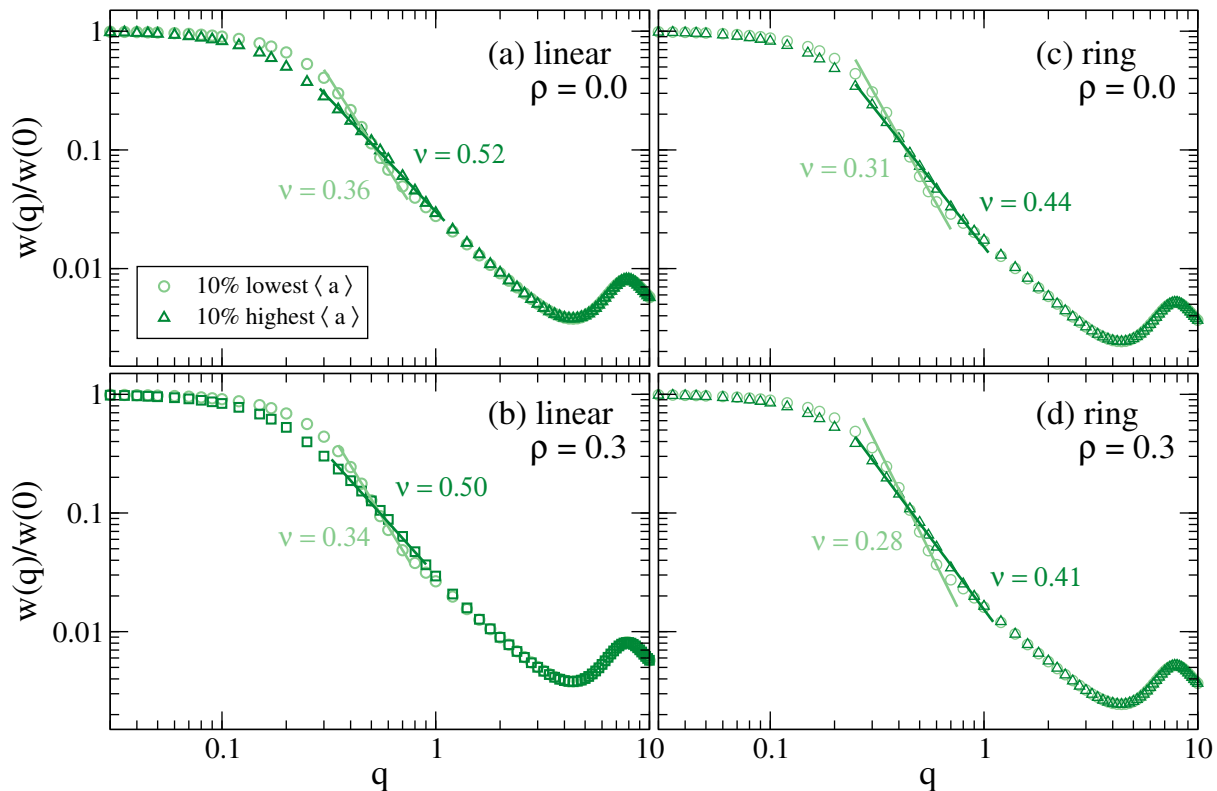
Figure 3.11: Normalized form factors, at infinite dilution, for the 10% with the lowest and 10% with the highest asphericity a of SCNPs synthesized from linear precursors at infinite dilution (a) and $\rho = 0.3$ (b), as well as of SCNPs synthesized from ring precursors at infinite dilution (c) and $\rho = 0.3$ (d). Solid lines are fits to power-laws, $w(q) \sim q^{-1/\nu}$, in the fractal regime. Each fitted line is annotated with its scaling exponent ν.

highest crowding density considered, $\rho = 0.3$ (bottom row). We observe that the difference in asphericity of the two subsets is accompanied by a different scaling behavior of their form factors in the fractal regimes and thus a different degree of compactness. The most spherical 10% of SCNPs exhibit a consistently lower scaling exponent than the least spherical 10% across all crowding densities considered and for both precursor architectures. When increasing the crowding density from infinite dilution to $\rho = 0.3$ at synthesis, we find that the exponents ν decrease by an amount comparable to those of the whole ensemble average (Figure 3.9). We would like to highlight that the most globular 10% of ring SCNPs adopt an even smaller scaling exponent than that expected for compact globular objects, $\nu = 1/3$. Especially those synthesized at a high crowding density ($\rho = 0.3$) appear to approach the limit of Porod scattering (with an effective exponent of $\nu = 1/4$) that is characteristic for dense particles with a smooth surface, such as hard spheres [24, 34, 35]. As such, this observation relates to the dense, highly impenetrable character of these SCNPs.
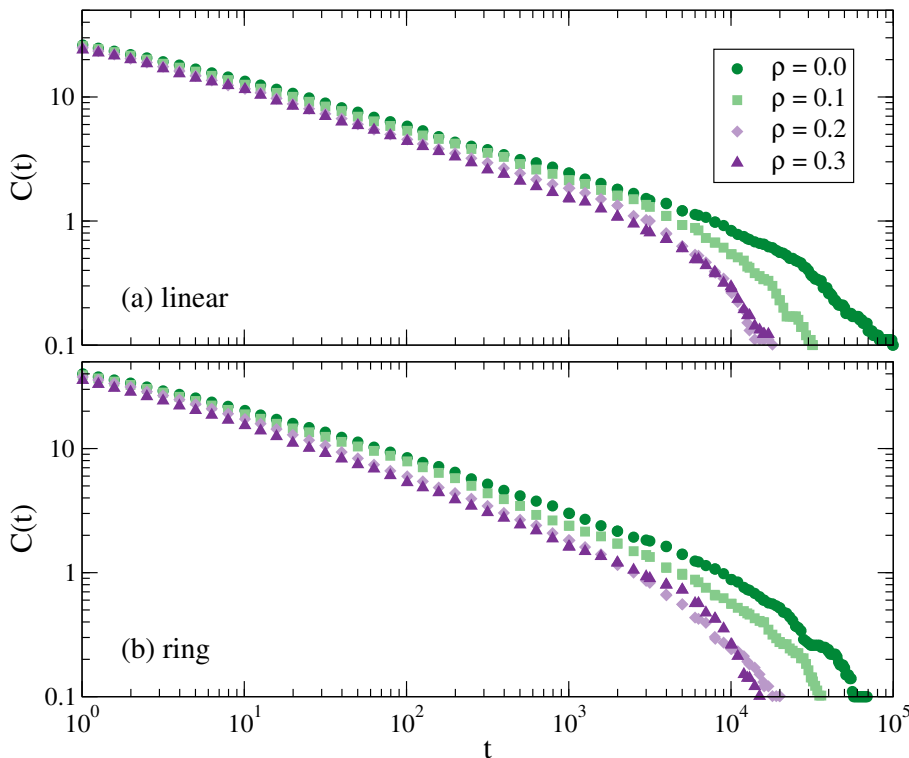
3.3.4 Cross-linking rate

Figure 3.12: Number of unlinked reactive monomers per reactive molecule $C(t)$ versus time t for SCNPs synthesized from linear (a) and ring (b) precursors at various densities. Symbol codes have the same meaning in both panels.

Finally, we investigate the dynamics of the cross-linking process by studying the effect crowding has on the rate of cross-link formation during the synthesis. Figure 3.12 displays the number of free reactive monomers which remain unbonded as a function of time. Note that $C(t)$ represents an ensemble average over all SCNPs. A first surprising result is that the time it takes to fully cross-link all reactive monomers is shorter for the ring precursors than the linear chains, even though their total number of reactive groups is higher due to their higher molecular weight. Increasing the density during synthesis accelerates the formation of bonds in both precursor architectures, which might be due to parts of the precursor separated by large contour distances being closer in space than in high dilution. However, we expect a reversal of this trend upon increasing the density further, especially when surpassing the entanglement density in the case of linear precursors, $\rho_{\mathrm{e}} = (N_{\mathrm{e}}/N)^{3\nu_{\mathrm{F}}-1} \approx 0.5$ [24], where $N_{\mathrm{e}} \approx 65$ is the entanglement length of our particular model [36]. The overlap of the curves for $\rho = 0.2$ and $\rho = 0.3$ suggest that the system is approaching this crossover. Entanglements confine the polymer chain to reptate along its primitive path, which increases the relaxation time of the chain on length scales larger than the tube diameter substantially. According to the reptation model it scales

as $\tau_{\mathrm{rep}} \sim \rho^{3(1-\nu_{\mathrm{F}})/(3\nu_{\mathrm{F}}-1)} N^3 \sim \rho^{1.6} N^3$ [24], which signifies a much stronger dependence on N than the Rouse scaling $\tau_{\mathrm{Rouse}} \sim N^2$ of unentangled polymers. This slowing down of the dynamics should eventually lead to a simultaneous slowing down of the cross-linking process. Furthermore, for ring polymer precursors, we expect concatenations such as illustrated in Figure 3.3 to happen more frequently at higher density due to a stronger interpenetration of neighboring polymers. These considerations, along with the associated increased computational cost, have led us to the decision of not investigating crowder concentrations beyond $\rho = 0.3$.

3.4 Conclusion

We have investigated the separate and combined effects of precursor topology and the presence of purely steric crowders at synthesis on the structural characteristics of single-chain nanoparticles. By means of molecular dynamics simulations, we carried out the cross-linking process of highly dilute ring or linear polymeric precursors decorated with randomly distributed functional groups in the presence of inert polymers of the same architecture (linear chains or rings). The range of crowding densities considered, $\rho = 0.1 - 0.3$, lies well beyond the overlap concentration but below the entanglement concentration and is typical of cellular environments [37]. We were able to show that ring polymers constitute promising new candidates as SCNP precursors for the design of compact, globular SCNPs. So far, this goal has remained elusive in single-chain technology, as the conventional synthesis route has proven to result in SCNP ensembles dominated by open sparse morphologies [11, 10, 12].

While crowding the solution in which synthesis takes place only has minor effects on the resulting SCNP size and shape if linear precursors are used, we find both a compaction and a trend towards more spherical conformations in the case of ring polymer precursors. The resulting ring SCNPs essentially retain, in the swollen state at high dilution, the scaling behavior observed for their precursor molecules at the corresponding density at which synthesis took place. We conclude that the intrinsic topology of ring polymers, which leads to a collapse to crumpled globules under crowding conditions, facilitates the formation of long-range loops and enables the SCNP to freeze its topology in a typical conformation of the precursor.

The findings of this chapter constitute a relevant contribution to the array of novel synthesis routes suggested by molecular dynamics simulations. While most single-chain

nanoparticles synthesized so far have been limited to linear precursors with bulky side groups or branches [9, 38, 39, 40, 41], our study suggests that ring polymers are better suited for the design of soft globular nanoparticles for biomedical and industrial applications. A drawback of our proposed route is that the synthesis and purification of monodisperse, unknotted and non-concatenated rings without linear contaminants poses a major challenge to chemists and engineers. However, recent advances in isolation of rings from linear polymers of equal molecular weight [42, 43, 44, 45, 46, 47, 48] make our protocol seem within reach of nanotechnology in the near future. Indeed, only recently, the first experimental realization of so-called "single-ring nanoparticles" (SRNPs) has been achieved by Rubio-Cervilla *et al.* via a stepwise folding-activation-collapse process [15]. The compaction degree, as determined by size-exclusion chromatography, was found to be significantly higher for SRNPs than their linear counterparts, validating our results.

References

[1] I. Perez-Baena, I. Loinaz, D. Padro, I. García, H. J. Grande, and I. Odriozola, "Single-chain polyacrylic nanoparticles with multiple gd(iii) centres as potential mri contrast agents," *J. Mater. Chem.*, vol. 20, pp. 6916–6922, 2010.

[2] Y. Bai, H. Xing, G. A. Vincil, J. Lee, E. J. Henderson, Y. Lu, N. G. Lemcoff, and S. C. Zimmerman, "Practical synthesis of water-soluble organic nanoparticles with a single reactive group and a functional carrier scaffold," *Chem. Sci.*, vol. 5, pp. 2862–2868, 2014.

[3] S. K. Hamilton and E. Harth, "Molecular dendritic transporter nanoparticle vectors provide efficient intracellular delivery of peptides," *ACS Nano*, vol. 3, no. 2, pp. 402–410, 2009. PMID: 19236078.

[4] A. Sanchez-Sanchez, S. Akbari, A. J. Moreno, F. L. Verso, A. Arbe, J. Colmenero, and J. A. Pomposo, "Design and preparation of single-chain nanocarriers mimicking disordered proteins for combined delivery of dermal bioactive cargos," *Macromolecular Rapid Communications*, vol. 34, no. 21, pp. 1681–1686, 2013.

[5] T. Terashima, T. Mes, T. F. A. De Greef, M. A. J. Gillissen, P. Besenius, A. R. A. Palmans, and E. W. Meijer, "Single-chain folding of polymers for catalytic systems in water," *Journal of the American Chemical Society*, vol. 133, no. 13, pp. 4742–4745, 2011. PMID: 21405022.

[6] I. Perez-Baena, F. Barroso-Bujans, U. Gasser, A. Arbe, A. J. Moreno, J. Colmenero, and J. A. Pomposo, "Endowing single-chain polymer nanoparticles with enzyme-mimetic activity," *ACS Macro Letters*, vol. 2, no. 9, pp. 775–779, 2013.

[7] E. Huerta, P. J. M. Stals, E. W. Meijer, and A. R. A. Palmans, "Consequences of folding a water-soluble polymer around an organocatalyst," *Angewandte Chemie International Edition*, vol. 52, no. 10, pp. 2906–2910, 2013.

[8] C. A. Tooley, S. Pazicni, and E. B. Berda, "Toward a tunable synthetic [fefe] hydrogenase mimic: single-chain nanoparticles functionalized with a single diiron cluster," *Polym. Chem.*, vol. 6, pp. 7646–7651, 2015.

[9] A. Sanchez-Sanchez, S. Akbari, A. Etxeberria, A. Arbe, U. Gasser, A. J. Moreno, J. Colmenero, and J. A. Pomposo, ""michael" nanocarriers mimicking transient-binding disordered proteins," *ACS Macro Letters*, vol. 2, no. 6, pp. 491–495, 2013.

[10] A. J. Moreno, F. Lo Verso, A. Sanchez-Sanchez, A. Arbe, J. Colmenero, and J. A. Pomposo, "Advantages of orthogonal folding of single polymer chains to soft nanoparticles," *Macromolecules*, vol. 46, no. 24, pp. 9748–9759, 2013.

[11] J. A. Pomposo, I. Perez-Baena, F. Lo Verso, A. J. Moreno, A. Arbe, and J. Colmenero, "How far are single-chain polymer nanoparticles in solution from the globular state?," *ACS Macro Letters*, vol. 3, no. 8, pp. 767–772, 2014.

[12] F. Lo Verso, J. A. Pomposo, J. Colmenero, and A. J. Moreno, "Multi-orthogonal folding of single polymer chains into soft nanoparticles," *Soft Matter*, vol. 10, pp. 4813–4821, 2014.

[13] I. Perez-Baena, I. Asenjo-Sanz, A. Arbe, A. J. Moreno, F. Lo Verso, J. Colmenero, and J. A. Pomposo, "Efficient route to compact single-chain nanoparticles: Photoactivated synthesis via thiol–yne coupling reaction," *Macromolecules*, vol. 47, no. 23, pp. 8270–8280, 2014.

[14] F. Lo Verso, J. A. Pomposo, J. Colmenero, and A. J. Moreno, "Simulation guided design of globular single-chain nanoparticles by tuning the solvent quality," *Soft Matter*, vol. 11, pp. 1369–1375, 2015.

[15] J. Rubio-Cervilla, H. Frisch, C. Barner-Kowollik, and J. A. Pomposo, "Synthesis of single-ring nanoparticles mimicking natural cyclotides by a stepwise folding-activation-collapse process," *Macromolecular Rapid Communications*, vol. 40, no. 1, p. 1800491, 2019.

[16] D. Chao, X. Jia, B. Tuten, C. Wang, and E. B. Berda, "Controlled folding of a novel electroactive polyolefin via multiple sequential orthogonal intra-chain interactions," *Chem. Commun.*, vol. 49, pp. 4178–4180, 2013.

[17] R. Merrifield, "Solid-phase peptide synthesis," *Advances in enzymology and related areas of molecular biology*, vol. 32, pp. 221–296, 1969.

[18] S. Basasoro, M. Gonzalez-Burgos, A. J. Moreno, F. L. Verso, A. Arbe, J. Colmenero, and J. A. Pomposo, "A solvent-based strategy for tuning the internal structure of metallo-folded single-chain nanoparticles," *Macromolecular Rapid Communications*, vol. 37, no. 13, pp. 1060–1065, 2016.

[19] A. J. Moreno, F. Lo Verso, A. Arbe, J. A. Pomposo, and J. Colmenero, "Concentrated solutions of single-chain nanoparticles: A simple model for intrinsically disordered

proteins under crowding conditions," *J. Phys. Chem. Lett.*, vol. 7, no. 5, pp. 838–844, 2016.

[20] M. Gonzalez-Burgos, A. Arbe, A. J. Moreno, J. A. Pomposo, A. Radulescu, and J. Colmenero, "Crowding the environment of single-chain nanoparticles: A combined study by sans and simulations," *Macromolecules*, vol. 51, no. 4, pp. 1573–1585, 2018.

[21] A. Y. Grosberg, S. K. Nechaev, and E. I. Shakhnovich, "The role of topological constraints in the kinetics of collapse of macromolecules," *J. Phys. (Paris)*, vol. 49, no. 12, pp. 2095–2100, 1988.

[22] J. D. Halverson, W. B. Lee, G. S. Grest, A. Y. Grosberg, and K. Kremer, "Molecular dynamics simulation study of nonconcatenated ring polymers in a melt. i. statics," *J. Chem. Phys.*, vol. 134, no. 20, p. 204904, 2011.

[23] K. K. Oehlenschlaeger, J. O. Mueller, N. B. Heine, M. Glassner, N. K. Guimard, G. Delaittre, F. G. Schmidt, and C. Barner-Kowollik, "Light-induced modular ligation of conventional raft polymers," *Angewandte Chemie International Edition*, vol. 52, no. 2, pp. 762–766, 2013.

[24] M. Rubinstein and R. H. Colby, *Polymer Physics*, vol. 23. Oxford University Press: Oxford, U.K., 2003.

[25] M. Doi and S. F. Edwards, *The theory of polymer dynamics.* Oxford University Press: Oxford, U.K., 1986.

[26] S. Y. Reigh and D. Y. Yoon, "Concentration dependence of ring polymer conformations from monte carlo simulations," *ACS Macro Lett.*, vol. 2, no. 4, pp. 296–300, 2013.

[27] S. Gooßen, A. R. Brás, M. Krutyeva, M. Sharp, P. Falus, A. Feoktystov, U. Gasser, W. Pyckhout-Hintzen, A. Wischnewski, and D. Richter, "Molecular scale dynamics of large ring polymers," *Phys. Rev. Lett.*, vol. 113, p. 168302, Oct 2014.

[28] K. Šolc and W. Stockmayer, "Statistical mechanics of random-flight chains. iv. size and shape parameters of cyclic, star-like, and comb-like chains," *Macromolecules*, vol. 6, no. 3, pp. 378–385, 1973.

[29] D. N. Theodorou and U. W. Suter, "Shape of unperturbed linear polymers: polypropylene," *Macromolecules*, vol. 18, no. 6, pp. 1206–1214, 1985.

[30] J. Rudnick and G. Gaspari, "The asperity of random walks," *Journal of Physics A: Mathematical and General*, vol. 19, no. 4, p. L191, 1986.

[31] J. Rudnick and G. Gaspari, "The shapes of random walks," *Science*, vol. 237, no. 4813, pp. 384–389, 1987.

[32] R. Lua, A. L. Borovinskiy, and A. Y. Grosberg, "Fractal and statistical properties of large compact polymers: a computational study," *Polymer*, vol. 45, no. 2, pp. 717 – 731, 2004. Conformational Protein Conformations.

[33] M. Bohn, D. W. Heermann, O. Lourenço, and C. Cordeiro, "On the influence of topological catenation and bonding constraints on ring polymers," *Macromolecules*, vol. 43, no. 5, pp. 2564–2573, 2010.

[34] G. S. Grest, K. Kremer, and T. A. Witten, "Structure of many arm star polymers: a molecular dynamics simulation," *Macromolecules*, vol. 20, no. 6, pp. 1376–1383, 1987.

[35] G. S. Grest, K. Kremer, S. T. Milner, and T. A. Witten, "Relaxation of self-entangled many-arm star polymers," *Macromolecules*, vol. 22, no. 4, pp. 1904–1910, 1989.

[36] S. K. Sukumaran, G. S. Grest, K. Kremer, and R. Everaers, "Identifying the primitive path mesh in entangled polymer liquids," *Journal of Polymer Science Part B: Polymer Physics*, vol. 43, no. 8, pp. 917–933, 2005.

[37] F.-X. Theillet, A. Binolfi, T. Frembgen-Kesner, K. Hingorani, M. Sarkar, C. Kyne, C. Li, P. B. Crowley, L. Gierasch, G. J. Pielak, A. H. Elcock, A. Gershenson, and P. Selenko, "Physicochemical properties of cells and their effects on intrinsically disordered proteins (idps)," *Chemical Reviews*, vol. 114, no. 13, pp. 6661–6714, 2014.

[38] E. Harth, B. V. Horn, V. Y. Lee, D. S. Germack, C. P. Gonzales, R. D. Miller, and C. J. Hawker, "A facile approach to architecturally defined nanoparticles via intramolecular chain collapse," *Journal of the American Chemical Society*, vol. 124, no. 29, pp. 8653–8660, 2002. PMID: 12121107.

[39] J. Jiang and S. Thayumanavan, "Synthesis and characterization of amine-functionalized polystyrene nanoparticles," *Macromolecules*, vol. 38, no. 14, pp. 5886–5891, 2005.

[40] T. A. Croce, S. K. Hamilton, M. L. Chen, H. Muchalski, and E. Harth, "Alternative o-quinodimethane cross-linking precursors for intramolecular chain collapse nanoparticles," *Macromolecules*, vol. 40, no. 17, pp. 6028–6031, 2007.

[41] A. Ruiz de Luzuriaga, I. Perez-Baena, S. Montes, I. Loinaz, I. Odriozola, I. García, and J. A. Pomposo, "New route to polymeric nanoparticles by click chemistry using bifunctional cross-linkers," *Macromolecular Symposia*, vol. 296, no. 1, pp. 303–310, 2010.

[42] H. Pasch and B. Trathnigg, *HPLC of Polymers.* Springer, Berlin, 1999.

[43] H. C. Lee, H. Lee, W. Lee, T. Chang, and J. Roovers, "Fractionation of cyclic polystyrene from linear precursor by hplc at the chromatographic critical condition," *Macromolecules*, vol. 33, no. 22, pp. 8119–8121, 2000.

[44] W. Lee, H. Lee, H. C. Lee, D. Cho, T. Chang, A. A. Gorbunov, and J. Roovers, "Retention behavior of linear and ring polystyrene at the chromatographic critical condition," *Macromolecules*, vol. 35, no. 2, pp. 529–538, 2002.

[45] Y. Tezuka, K. Mori, and H. Oike, "Efficient synthesis of cyclic poly(oxyethylene) by electrostatic self-assembly and covalent fixation with telechelic precursor having cyclic ammonium salt groups," *Macromolecules*, vol. 35, no. 14, pp. 5707–5711, 2002.

[46] J. R. Montenegro-Burke, J. M. Bennett, J. A. McLean, and D. M. Hercules, "Novel behavior of the chromatographic separation of linear and cyclic polymers," *Analytical and Bioanalytical Chemistry*, vol. 408, pp. 677–681, Jan 2016.

[47] F. Barroso-Bujans and A. Alegria, "Kinetic differences in the intercalation of linear and cyclic penta(ethylene oxide)s into graphite oxide leading to separation by topology," *Phys. Chem. Chem. Phys.*, 2017.

[48] L. B. Weiss, A. Nikoubashman, and C. N. Likos, "Topology-sensitive microfluidic filter for polymers of varying stiffness," *ACS Macro Letters*, vol. 6, no. 12, pp. 1426–1431, 2017.

Chapter 4

Single-Chain Nanoparticles under Homogeneous Shear Flow

4.1   Introduction

Non-equilibrium situations, especially complex flows, are ubiquitous in many of the potential applications of SCNPs, such as biomedicine and industry. For example, strong shearing forces can arise in blood flow through thin arteries, microfluidic devices and extrusion processes. Homogeneous shear flow represents the special case of a non-equilibrium stationary state, which makes it an ideal first test case for elucidating the dynamic behavior of macromolecules such as colloids and polymers. In order to connect the large-scale material properties of a solution to the underlying microscopical dynamics, it is imperative to study the behavior of individual polymers in high dilution before tackling the more complex response of semildilute and crowded solutions, where entanglements, jamming and reptation become relevant. Recent advances in fluorescent imaging techniques combined with complex microfluidic devices have enabled scientists to directly measure the reorientation dynamics of large molecules on the μm-scale and above. These methods could confirm two interesting complex cyclic motions in shear flows, which were first predicted by theoretical calculations: DNA, a long semiflexible linear polymer, undergoes tumbling, characterized by alternating stretching and collapse [1, 2, 3, 4]; Red blood cells, essentially empty ellipsoidal vesicles, exhibit tank-treading, characterized by a rotation of their membrane constituents along their contour [5, 6, 7, 8]. Although the small size of most polymers precludes the study of their orientational dynamics under flow via imaging techniques, meso-scale computer simulations including hydrodynamic interactions have been successfully employed to observe similar behaviors in a variety of polymer architectures, such as rings, stars or dendrimers. The complex topology of SCNPs is expected to yield a rich variety of dynamical behaviors under flow, possibly showing a mixture of tumbling and tank-treading, depending on the specific connectivity of an individual SCNP.

In semidilute and crowded solutions, the rheological properties of polymers are of broad interest, because they often display non-linear phenomena that give rise to surprising effects. Contrary to simple Newtonian liquids, which possess a constant viscosity for all shear rates, polymer solutions usually exhibit shear thickening or shear thinning. We might even encounter both in a single polymer, depending on the concentration, the shear rate or the solvent conditions [9]. The emergence of such non-linear rheology stems from the interplay of two counteracting processes: First, the high malleability of polymers gives them the ability to adapt to and align with a particular flow field, reducing the viscosity with increasing shear rate (shear thinning). On the other hand, especially at high concentrations, intermolecular interactions can lead to entanglements, knots, association

and jamming, which hinder the alignment and increase the friction between layers of the solution, thus resulting in an increased viscosity (shear thickening).

In this chapter, we investigate in detail the flow properties of (i) single SCNPs of different topologies and (ii) semi-dilute solutions of SCNPs, at a wide range of experimentally relevant shear rates including hydrodynamic interactions. We will show that, to our own surprise, in infinite dilution, we find scaling laws for various conformational and rheological observables that do not depend on the specific topology, but arise purely from the cross-linked network-like intramolecular architecture of SCNPs. Furthermore, their set of exponents differs considerably from those observed for other polymer architectures (linear, ring, star), such that SCNPs emerge as a separate class of nanoparticles defined by their distinct flow properties. At the same time, we encounter a very rich underlying dynamical behavior including a superposition of tumbling and tank-treading motions, whose specifics are in fact dependent on the particular topology of a given SCNP.

When considering semi-dilute and concentrated solutions, we find complex dependence of their structural characteristics on the density of the solution. Contrary to simpler polymer architectures, such as linear chains and star polymers, two distinct scaling regimes appear, with a cross-over around the overlap concentration. We will show that this novel phenomenon is not related to the topological polydispersity of the solution, but qualitatively persists in monodisperse solutions of globular, sparse or intermediate SCNPs. These findings are related to the inherent impenetrability of SCNPs, conferred by the presence of loops and clusters and their transition to crumpled globules under crowding conditions.

4.2 Simulation Details

We perform multi-scale simulations that consist of a hybrid combination of Molecular Dynamics (MD) for the SCNPs and Multi-particle Collision Dynamics for the solvent. Both algorithms are described in detail in Chapters 2.5 and 2.7. The coupling between the two techniques is achieved by including the solute molecules in the stochastic rotation step of the MPCD algorithm. The SCNPs are modeled according to the bead-spring model introduced in Chapter 2.2. As such, chain segments cannot cross each other, excluded volume interactions are taken into account and the extension of bonds is limited. Furthermore, the choice of potential mimics implicit good solvent conditions, as the MPCD

method does not include any specific interactions between solvent and solute except for the momentum exchange during the stochastic rotation.

Our simulation protocol consists of two steps. First, we synthesize the SCNPs following the standard procedure of employing highly dilute conditions. For this, we neglect hydrodynamic interactions and instead perform Langevin dynamics simulations [10], since this has shown to suffice for obtaining semi-quantitative agreement of the structural properties of the resulting SCNPs between experiments and simulations. The linear precursor chains are comprised of $N = 200$ monomers, of which a fraction $f = N_r/N = 0.25$ are reactive species randomly distributed along the polymer backbone. During the synthesis, they form irreversible and monovalent cross-links as described in Chapter 2.3.

In the following step, we perform hybrid MD+MPCD simulations for either a single SCNP topology or a solution of SCNPs. How we chose the particular topologies employed is explained in detail later. The simulations under shear are carried out on two different time scales with two different algorithms. The solvent is modeled via MPCD [11, 12] as N_s point-like particles of mass m, whose motion is governed by two alternating steps:

i) A *streaming* step of size $h = 0.1\sqrt{ma^2/k_BT}$, at which the solvent positions are updated according to ballistic motion:

$$\mathbf{r}_i(t + \Delta t) = \mathbf{r}_i(t) + h\mathbf{v}_i(t), \qquad (4.1)$$

with $\mathbf{r}_i$ and $\mathbf{v}_i$ the position and velocity of the solvent particle i. ii) A *collision* step, in which the solvent particles exchange linear momentum to propagate the hydrodynamic information. Here, the particles are sorted into cubic cells of lattice constant a and rotated around a random axis by an angle α with respect to the center-of-mass velocity of the cell $\mathbf{v}_{\mathrm{cm}}$, i.e.

$$\mathbf{v}_i(t + \Delta t) = \mathbf{v}_{\mathrm{cm}}(t) + \mathbf{R}(\alpha)\left(\mathbf{v}_i(t) - \mathbf{v}_{\mathrm{cm}}(t)\right), \qquad (4.2)$$

with $\mathbf{R}(\alpha)$ the rotation matrix. We employ a grid shift at every step to ensure Galilean invariance (see Chapter 2.7.2)[13, 14] and a cell-level canonical Maxwell-Boltzmann scaling thermostat to keep the system at a constant temperature T (see Chapter 2.7.3).

The coupling between solvent and solute is achieved by including the latter in the stochastic rotation of the collision step. Between successive MPCD steps, the monomers of the SCNPs are simulated via Molecular Dynamics with the Velocity Verlet scheme and a time-step of $\Delta t = 0.01\sqrt{ma^2/k_BT}$.
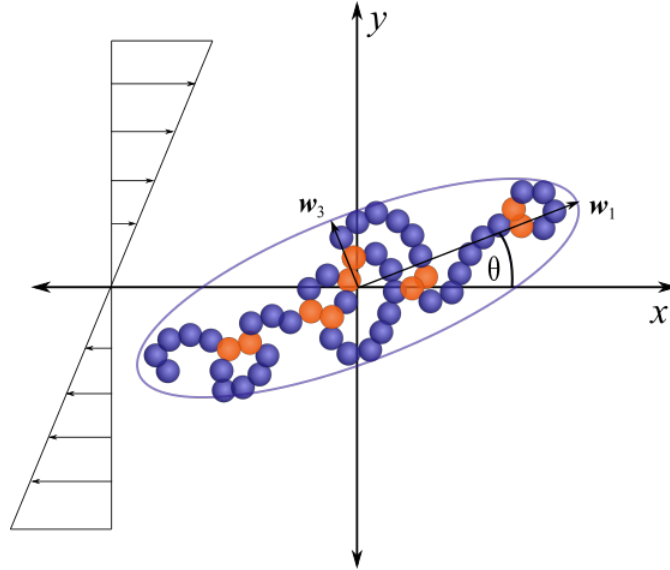
Figure 4.1: Schematic representation of the simulation setup. The fluid velocity profile is indicated on the left. Throughout this work, x is the flow direction, y the gradient direction and z – pointing out of the plane – is the vorticity direction. The angle θ lies between the principal vector of the gyration tensor, $\boldsymbol{w_1}$, and the x-axis. Reactive monomers that have formed cross-links are colored in orange, non-reactive monomers are colored in blue.

A linear shear profile

$$\langle v_x(y) \rangle = \dot{\gamma} y \tag{4.3}$$

is imposed on the system by Lees-Edwards boundary conditions (see Chapter 2.7.4)[15]. In Equation 4.3 $\dot{\gamma}$ denotes the shear rate and v_x the x-component of the velocity. As such, it defines x as the flow, y as the gradient and z as the vorticity direction. The simulation setup is schematically illustrated in Figure 4.1.

The parameters employed in the hybrid simulations are as follows: The average number of solvent particles per cell of size $a = \sigma = 1$ is $\rho = 5$. The mass of the solvent particles is $m = 1$, while that of the solute monomers is $M = \rho m = 5$. The angle of the stochastic rotation is fixed at $\alpha = 130°$. Finally, the volume of the simulation box $V = L_x L_y L_z$ is chosen based on the size of the SCNPs in equilibrium. For the single molecule simulations, we ensure that each side length of the box is greater than four times the radius of gyration of any SCNP at $\dot{\gamma} = 0$, i.e. $L_\mu = 50\sigma \geq 4R_\mathrm{g}$ for $\mu \in \{y, z\}$. Due to the strong stretching of the SCNPs in the flow direction at high shear rates, the extension of the box in the x-direction is adapted for increasing shear rates and ranges from $L_x = 50\sigma$ to $L_x = 100\sigma$. For the semi-dilute and concentrated solutions, the box volume is kept constant at $V = 32 * (2R_\mathrm{g})^3$, while we change the number of SCNPs in the system between $8 \leq N_\mathrm{c} \leq 200$. As such, at low shear rates $V = (47\sigma)^3$ for the topologically polydisperse solution and $V = (40\sigma)^3, (47\sigma)^3$ and $(56\sigma)^3$ for the monodisperse solutions

of low, intermediate and high asphericity, respectively. Upon increasing the shear rate, the box is extended in the x-direction and compressed in the y and z-directions, while keeping the volume constant. We perform between 5 and 20 independent simulation runs for each shear rate, concentration and SCNP topology (the lower the density, the higher the number of independent runs in order to sample a sufficient number of SCNPs). Each of these is started from different initial conformations and velocities and consists of 10^5 equilibration steps and 10^7 production steps.

Since comparison with a linear reference system had proven elusive due to different models and polymerization degrees used throughout the literature, we performed additional simulations of linear chains of the same number of monomers $N = 200$ to complement the literature data for shorter chains ($N \leq 60$) [16, 17], and for long semiflexible chains (DNA, combining experiments and numerical modeling) [18]. Despite the different models and implementations, our results are in quantitative agreement with the literature.

4.3   Results and Discussion

4.3.1   Single molecule simulations

We begin our study by investigating in detail the influence a particular topology has on the properties of the SCNPs under homogeneous shear flow. The stochasticity of the cross-linking process leads to a high structural and topological polydispersity of the resulting SCNPs. Therefore, we sort the synthesized SCNPs into six equally sized groups based on their asphericity (see Equation 3.6). To get an accurate picture of the different
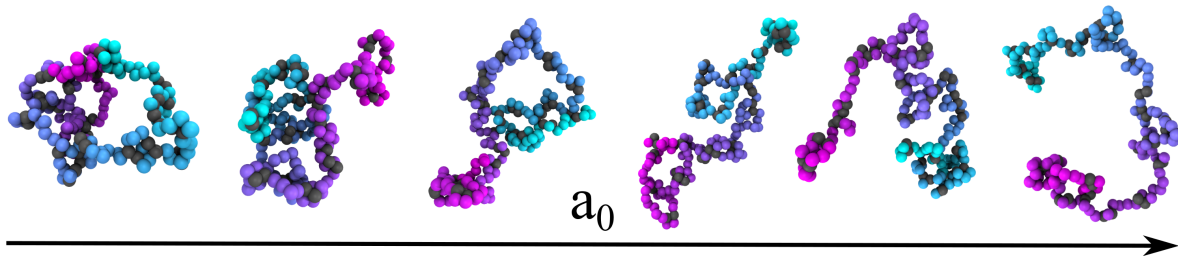

Figure 4.2: Representative snapshots of SCNPs at $\dot{\gamma} = 0$ with different values of the equilibrium asphericity a_0 (increasing from left to right). The respective equilibrium asphericities are, from left to right, $a_0 = 0.172, 0.224, 0.335, 0.412, 0.465$ and 0.495. Grey beads are cross-linked monomers. The rest of the monomers are colored, from magenta to cyan, according to their position in the backbone of the linear precursor.
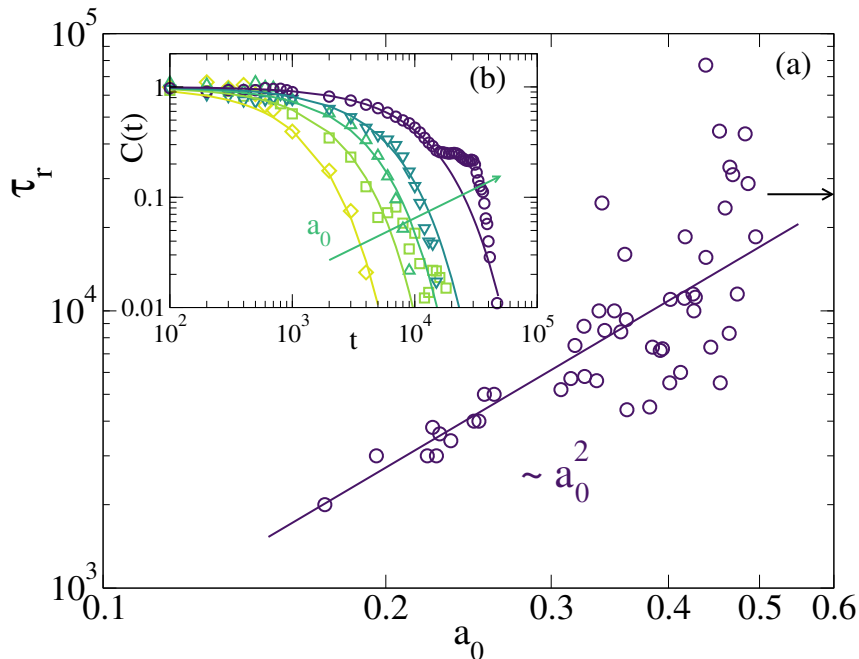
Figure 4.3: (a) Equilibrium relaxation times τ_r vs. asphericity parameters a_0 of 50 topologically distinct SCNPs. The arrow indicates the relaxation time of a linear chain of the same molecular weight. The inset (b) shows the autocorrelation function $C(t)$ of the radius of gyration R_g used to determine the relaxation times for five typical SCNPs. Solid lines indicate fits to exponential decays. The arrow indicates increasing equilibrium asphericity a_0.

behavior under shear for representative SCNP topologies over the whole range of their distribution, we choose one from each of the asphericity groups randomly. In the following step, we perform individual hybrid MD+MPCD simulations for the six chosen SCNPs. Their specific architectures are depicted in Figure 4.2. Our main observables studied are based on the gyration tensor $G_{\alpha\beta}$, which was already introduced in Chapter 3, Equation 3.4. We determine its eigenvalues $\lambda_1 \geq \lambda_2 \geq \lambda_3$ and corresponding eigenvectors $\boldsymbol{w}_1$, $\boldsymbol{w}_2$, $\boldsymbol{w}_3$, from which we can calculate the radius of gyration R_g (Equation 3.5) and the asphericity a (Equation 3.6).

SCNPs of different topologies undergo conformational changes on different time scales, as is reflected in their relaxation times τ_r. These are calculated from the decay of the autocorrelation function of the radius of gyration at zero shear rate,

$$C(t) = \frac{\langle R_g(t) R_g(0) \rangle - \langle R_g \rangle^2}{\langle R_g^2 \rangle - \langle R_g \rangle^2} , \tag{4.4}$$

to a value of 0.2. Figure 4.3 depicts the correlation between the asphericity of an individual SCNP and its relaxation time. We would like to highlight that the relaxation times spread over 1.5 orders of magnitude and exhibit a weak correlation with the asphericity as $\tau_r \sim a_0^2$. This should not be misinterpreted as a strict scaling law, but rather as an observed trend.
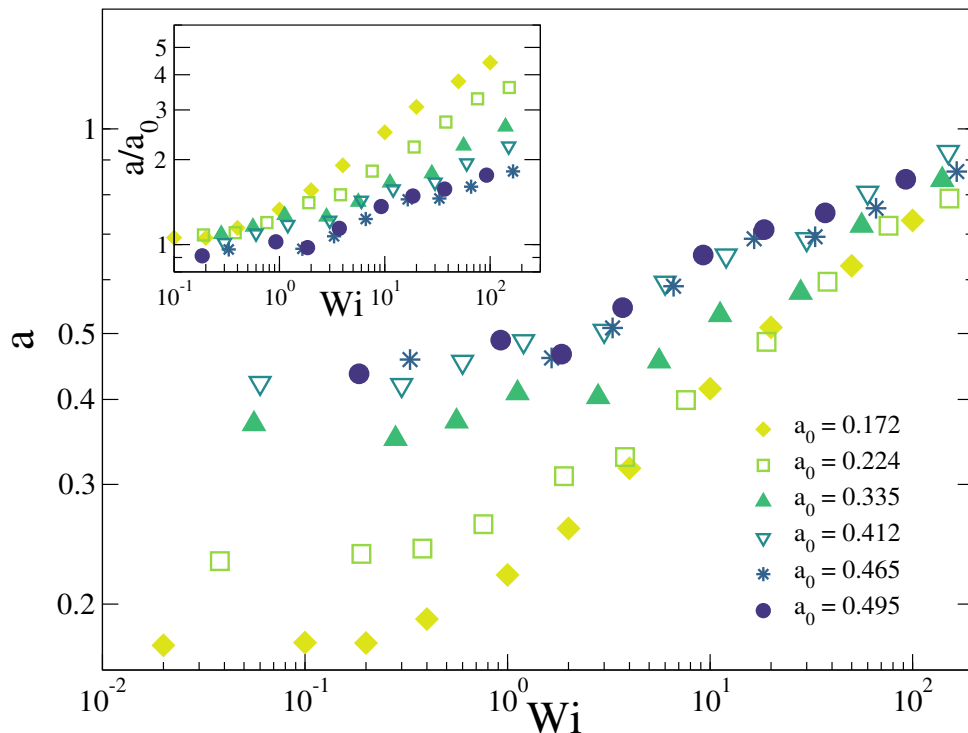
Figure 4.4: Main panel: asphericity a for various SCNP topologies as a function of the Weissenberg number Wi. The inset shows the same data normalized by the respective equilibrium ($\dot{\gamma} = 0$) asphericities a_0 (values given in the legend).

The inset 4.3(b) displays the autocorrelation function $C(t)$ for five representative SCNPs of very different asphericities to demonstrate the good agreement of $C(t)$ with a fit to an exponential decay. We use the relaxation time to define the dimensionless Weissenberg number $\text{Wi} = \dot{\gamma}\tau_r$ as the ratio between the relaxation time τ_r of the polymer at equilibrium and the characteristic time $\dot{\gamma}^{-1}$ of the shear flow. The Weissenberg number will be used in the following to scale the shear rate for a particular SCNP topology to compare between different SCNPs.

Structural properties

As a first measure of how the shape of the SCNPs is affected by the shear flow, in Figure 4.4 we plot the asphericity a as a function of the Weissenberg number Wi for the six different SCNPs. Upon increasing the shear rate, we encounter two distinct regimes: For small shear rates corresponding to $\text{Wi} \ll 1$, the average shape of the SCNP remains essentially unperturbed, because the polymer is able to relax faster than the flow can elongate it. Once $\text{Wi} \gg 1$, however – i.e. once the longest relaxation time of the polymer τ_r exceeds the characteristic time of the flow $\dot{\gamma}^{-1}$ –, the SCNPs stretch and adopt less
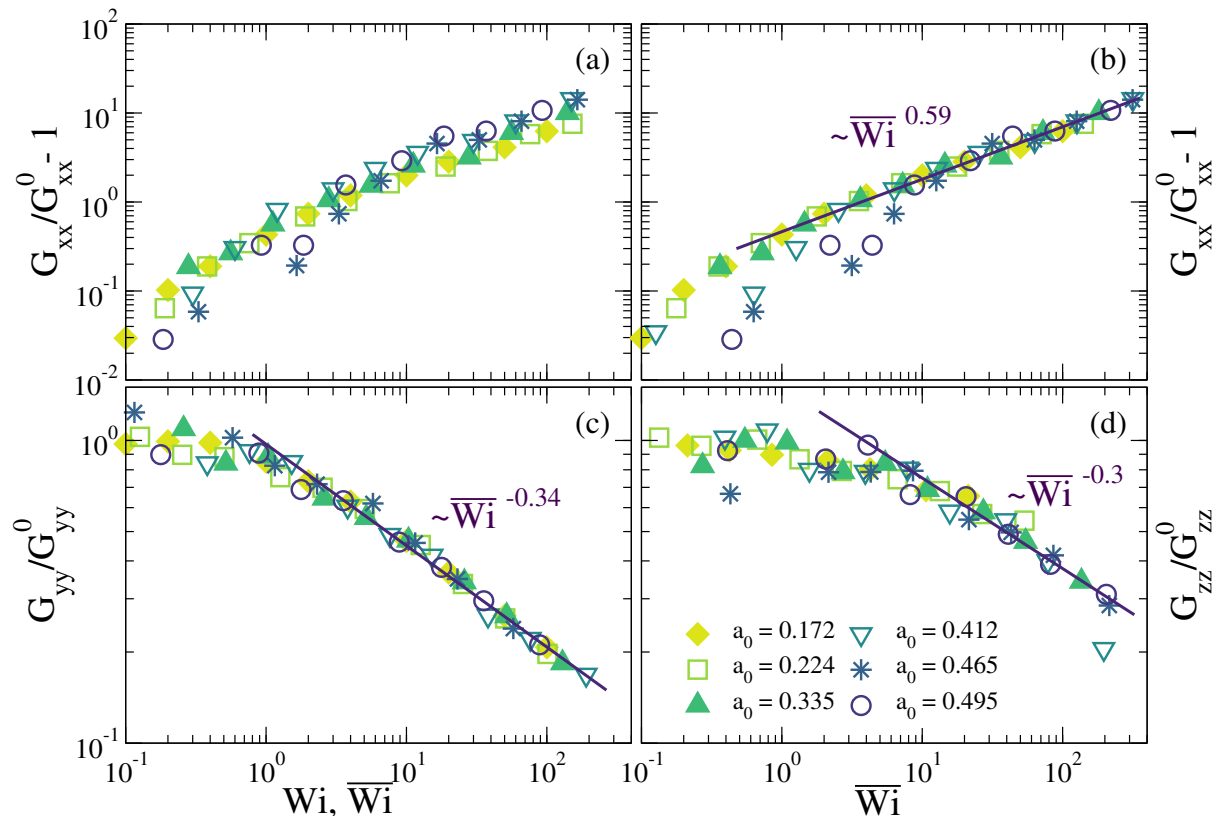
Figure 4.5: Normalized diagonal components of the gyration tensor $G_{\alpha\alpha}$ as a function of (a) Weissenberg number Wi and (b-d) rescaled Weissenberg number $\overline{\text{Wi}}$ for various SCNP topologies of distinct equilibrium asphericities. Results are given for: (a,b) flow direction, G_{xx}; (c) gradient direction, G_{yy}; (d) vorticity direction, G_{zz}. Lines are fits to power laws.

spherical conformations. The cross-over between the two response regimes coincides with Wi ≈ 1 for all SCNPs, which supports our choice of method to determine the relaxation time. The different responses for different SCNP topologies at high shear rates can be explained by their different equilibrium asphericities and the fact that they all approach the rod limit ($a = 1$) at the highest shear rates considered.

We now take a deeper look into the structural changes induced by the shear flow by considering the elongations in different directions as described by the diagonal components of the gyration tensor, $G_{\alpha\alpha}$. The elements G_{xx}, G_{yy}, and G_{zz}, representing the extension of the polymer in the flow, gradient and vorticity directions, respectively, are displayed in Figure 4.5, normalized by their values at equilibrium $G_{\alpha\alpha}^0$. Panels (a) and (b) depict the same data for G_{xx}, but in panel (b) the Weissenberg number is rescaled by a topology dependent multiplicative factor of the order of unity. Applying such a rescaling of the Weissenberg number $\overline{\text{Wi}} = \phi_i \text{Wi}$, we observe that the data for different SCNPs collapse onto a master curve in the high shear regime. This procedure of rescaling the Weissenberg number by a topology dependent factor is inspired by former work on star polymers,

	Linear $N = 200$	Linear (DNA)	Linear $N \leq 60$	Ring $N \leq 120$	G4D $N = 62$	Star $2N_a \leq 80$	SCNP $N = 200$
$G_{xx}/G_{xx}^0 - 1$	**0.63**		0.63* [17]	0.65 [21] 0.72* [17]	0.86 [22]	1.0 ($f \leq 50$) [19] 0.90* ($f = 18$) [23]	**0.59**
G_{yy}/G_{yy}^0	**-0.48**	-0.50 [18]	-0.42 [17]	-0.41 [24, 21] -0.43 [17]	-0.30* [22]	-0.42 ($f \leq 10$) [20] -0.32* ($f = 18$) [23]	**-0.34**
G_{zz}/G_{zz}^0	**-0.34**	-0.34 [18]	-0.33 [17]	-0.32 [24, 21] non-monotonic [17]	$\approx 0^\star$ [22]	-0.29 ($f \leq 10$) [20] -0.14* ($f = 18$) [23]	**-0.30**
m_G	**0.53**	0.57 [18]	0.54 [16]	0.60 [25, 24]	0.49 [22]	0.63 ($f \leq 10$) [20] 0.65 ($f \leq 50$) [19, 23]	**0.67**
$\omega_z/\dot{\gamma}$	**-1.0**			-0.38 [25, 24]		-0.52 ($f \leq 10$) [20] -1.0 ($f \leq 50$) [19]	**-0.75**
η_p/η_p^0	**-0.66**	-0.61 [18]	-0.59 [16]	-0.43 [24, 21] -0.64 [17]		-0.40 ($f \leq 10$) [20]	**-0.48**
Φ_1/Φ_1^0	**-1.2**	-1.37 [18]	-1.2 [16]	-0.97 [21]		-1.1 ($f \leq 10$) [20]	**-1.2**

Table 4.1: Scaling exponents for the Wi-dependence (at Wi > 1) of different static and dynamic observables in various molecular architectures at infinite dilution (G4D: 4th generation dendrimers). The polymerization degree is given by N. For stars, f is the number of arms and N_a the number of monomers per arm. Results from this work are highlighted by bold fonts, the rest are literature values. Star superscripts indicate exponents which were not reported in the original references. We obtained them by sampling and fitting the literature data. Data on DNA was obtained through a combination of simulations and experiments [18].

in which the authors found a similar universal power-law scaling of various structural properties for different numbers of arms (or functionality) f after rescaling by an f-dependent factor [19, 20]. However, since the stochastic topologies of SCNP cannot be numerically 'ordered' as the functionality f of star polymers, it is difficult to theoretically connect a specific topology to its multiplicative factor ϕ. We can only observe a systematic dependence on the asphericity. Given the interesting emergence of a master curve not only for G_{xx}, but also for G_{yy} and G_{zz} (Panels (c-d)), we will report most of the results as a function of $\overline{\text{Wi}}$ for the remainder of this chapter. While the SCNPs stretch in the flow direction, scaling as $G_{xx} \sim \text{Wi}^\mu$ with $\mu = 0.59$, they compress in the gradient and vorticity directions with very similar scaling exponents: $\mu = -0.34$ and -0.30, respectively.

Power laws such as those reported here have also been observed in various other molecular architectures. In Table 4.1 we compile results for linear chains, rings, dendrimers and star polymers from the literature, preferentially from sources employing the same methodology, but also including data from experiments on DNA. The relative extension of SCNPs in the flow direction is comparable to that of linear and ring polymers, albeit showing a weaker dependence on the shear rate ($\mu = 0.59$ vs. 0.63 and 0.65 for linear chains

and rings, respectively). This is consistent with the sparse, but still highly connected "rings-on-a-chain" topology of most SCNPs, which prevents elongation to some degree.

In the gradient direction, however, the compression exhibits a weaker dependence on the Weissenberg number in SCNPs than in chains and rings. G_{yy} shows more similarities with dendrimers and high-functionality star polymers. An explanation for this might lie in the analogy between the cross-links of SCNPs, the branch points of dendrimers and the entanglements of different arms of a star polymer, which all give rise to denser structures and jamming close to the center-of-mass of the polymers, which limits compression in any direction. Finally, in the vorticity direction, the highly malleable architectures (linear chains, rings, low-f stars) exhibit a very similar scaling of $\mu \sim 0.3$, while denser structures such as high-functionality stars and dendrimers show a weak or marginal dependence on the Weissenberg number. SCNPs, with their very similar scaling exponents in the gradient and vorticity direction ($\mu = -0.34$ and -0.30) present a novel behavior in this regard, which results from their combination of high global malleability and locally compact structures.

We would like to point out that, although we investigate a broad range Wi-values, we cannot reach the highest Weissenberg numbers accessible by experiments. This is due to an inherent limitation of the MPCD algorithm. As it is designed for incompressible fluids, once the Mach number (i.e. the ratio between fluid velocity and the speed of sound) exceeds one, accurate resolution of hydrodynamic interactions is not guaranteed any longer. Given that in experiments Weissenberg numbers can easily lie on the order of 10^3, the exponents we observe in our simulations might just be effective intermediate values in a crossover regime to the limit of Wi $\gg 100$. For example, such an intermediate scaling is predicted for linear chains, where $G_{yy} \sim \text{Wi}^{-1/2}$ prior to the final crossover to $G_{yy} \sim \text{Wi}^{-2/3}$ in the high Wi limit [26, 27].

The average alignment of a molecule along the flow direction can be conveniently measured by its orientational resistance [28],

$$m_{\text{G}} = \text{Wi} \tan(2\theta) = \text{Wi} \frac{2G_{xy}}{G_{xx} - G_{yy}} \,, \tag{4.5}$$

which depends on the angle θ between the eigenvector $\boldsymbol{w}_1$ corresponding to the largest eigenvalue λ_1 and the flow direction x, as illustrated in Figure 4.1. It has been shown theoretically that for rodlike molecules and linear polymers, $G_{xy} \sim \dot{\gamma}$ and $(G_{xx} - G_{yy}) \sim \dot{\gamma}^2$ at low shear rates [29, 30, 16], which leads to m_{G} becoming independent of Wi in the low-Wi regime. This result was later reproduced in MPCD simulation of star polymers
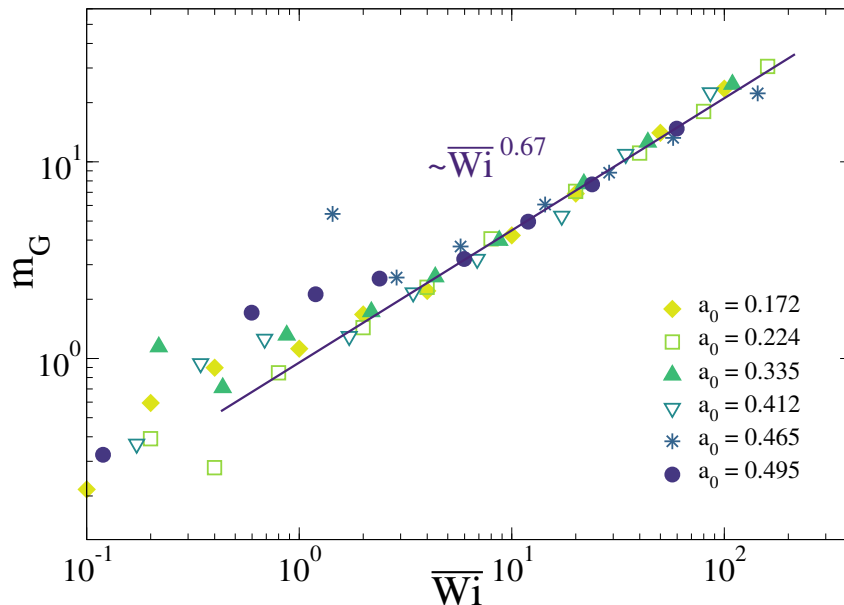
Figure 4.6: Orientational resistance m_{G} as a function of the rescaled Weissenberg number $\overline{\mathrm{Wi}}$ for SCNPs with different equilibrium asphericities.

[19]. Such a plateau is absent in the data for SCNPs (Figure 4.6), which might be due to the poor statistics. At low shear rates, the denominator $G_{xx} - G_{yy}$ in 4.5 is close to zero, because the extension of the polymer in the flow and gradient directions experience only a weak perturbation from equilibrium, where $G_{xx}^0 = G_{yy}^0$ due to symmetry considerations. This problem was also encountered in computational studies of dendrimers [22].

At high Wi, the results for m_{G} for the six SCNPs collapse onto a universal curve governed by $m_{\mathrm{G}} \sim \mathrm{Wi}^{\mu}$ with exponent $\mu = 0.67$ nonetheless. This scaling is reminiscent of that for star polymers, $\mu = 0.65$ [19, 23], while linear chains and dendrimers adopt significantly lower exponents of $\mu \sim 0.55$ [16, 18] and $\mu = 0.49$ [22], respectively. The particularly strong resistance to alignment with the flow direction of star polymers stems from jamming in the two oppositely oriented bundles of arms and is augmented by increasing the number of arms (see Table 4.1). In the SCNPs, similar strong repulsive forces arise from the compression of permanent loops and clusters when the SCNP tries to align with the flow.

Rheological properties

We now turn our discussion to the rheological properties of a solution containing such single-chain nanoparticles in the limit of very high dilution. We neglect the collisional viscosity stemming from the MPCD fluid and focus only on the polymer contribution to
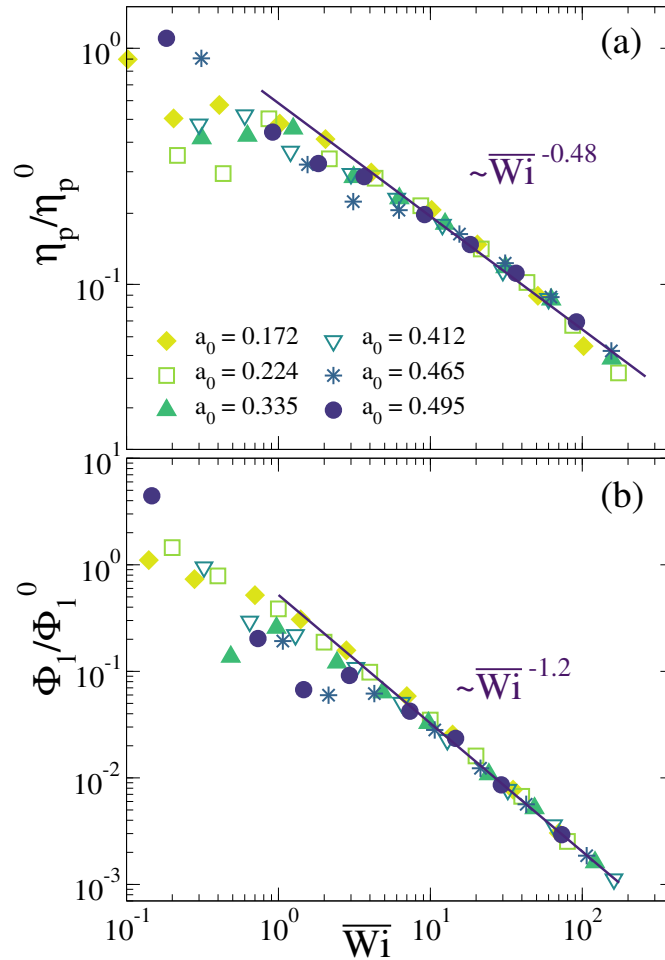
Figure 4.7: Normalized (a) polymer viscosity η_p and (b) first normal stress coefficient Φ_1 as a function of the rescaled Weissenberg number $\overline{\mathrm{Wi}}$ for SCNPs with different equilibrium asphericities.

the viscosity, which we derive from the Kramers-Kirkwood formula for the stress tensor [31],

$$\sigma_{\mu\nu} = -\sum_{i=1}^{N}\langle r_{i,\mu} F_{i,\nu}\rangle\,, \tag{4.6}$$

where $\boldsymbol{F}_i$ denotes the total force exerted on monomer i by the other monomers [32, 17]. From this, the viscosity is then calculated as

$$\eta_\mathrm{p} = \frac{\sigma_{xy}}{\dot\gamma}\,. \tag{4.7}$$

In Figure 4.7(a), we plot the polymer contribution to the viscosity as a function of Weissenberg number. The data are normalized by their zero-shear value η_p^0, which is traditionally defined through the Newtonian plateau of η_p at low shear rates Wi $\ll 1$. However, not all SCNPs, especially sparse ones with a long relaxation time, exhibit a well-defined plateau. Therefore, we first normalize the viscosities of the globular SCNPs and rescale those of the rest in such a way to obtain the best overlap of the different curves.

As expected for very dilute solutions, the polymers exhibit shear-thinning behavior, i.e. the intrinsic viscosity decreases upon increasing the shear rate. The resulting scaling law $\eta_{\mathrm{p}}/\eta_{\mathrm{p}}^0 \sim \mathrm{Wi}^\mu$ with $\mu = -0.48$ is comparable to that of star and ring polymers (see 4.1) and shows a considerably weaker dependence on the shear rate than linear chains ($\mu \sim -0.6$; $\mu = -2/3$ in the limit of high Weissenberg numbers [26, 27]). The higher exponents found for linear chains can be understood in terms of their higher flexibility and their self-avoiding character, which allows them to be stronger aligned with the flow and leads to a higher concentration of solvent around each monomer.

In the absence of hydrodynamic interactions, such as in some semi-dilute or concentrated solutions, where hydrodynamic interactions are effectively screened by the surrounding molecules, the formula for the stress tensor reduces to the Giesekus approximation [9]

$$\eta_{\mathrm{p}} = \sum_{i=1}^{N} \left\langle \frac{r_{i,y}r_{i,y}}{2} \right\rangle \sim G_{yy}. \tag{4.8}$$

Thus, agreement between η_{p} and G_{yy} can be understood as a proxy for the importance of hydrodynamics in the accurate description of the system. For example, linear chains in the free-draining limit [33, 18] and semi-dilute solutions of linear polymers [34] follow this prediction ($\eta_{\mathrm{p}} \sim G_{yy}$). While there is also some similarity in the scaling exponents of η_{p} and G_{yy} for low-functionality stars and rings (see 4.1), the Giesekus approximation clearly fails in the case of SCNPs, where $G_{yy} \sim \mathrm{Wi}^{-0.34}$, but $\eta_{\mathrm{p}} \sim \mathrm{Wi}^{-0.48}$, demonstrating the relevance of hydrodynamic interactions in their rheological properties.

We further calculate the first normal stress coefficient, which is given by different components of the stress tensor,

$$\Phi_1 = \frac{\sigma_{xx} - \sigma_{yy}}{\dot{\gamma}^2}, \tag{4.9}$$

and should, similar to the viscosity, show a crossover to a plateau at low Weissenberg number, where $\sigma_{xx} - \sigma_{yy} \sim \dot{\gamma}^2$. However, we encounter the same difficulties in determining the low-shear plateau as for the viscosity data and thus rescale Φ_1 in a similar manner in order to collapse the data onto a master curve at high Wi. We find that the scaling exponents adopted by the SCNPs ($\mu = -1.2$) represent an intermediate case between that of linear chains ($\mu \sim -1.3$; $\mu = -4/3$ according to scaling arguments) [16, 34, 27] and low-f stars or rings ($\mu = -1.1$ and -0.97) [21].

Dynamic behavior

Finally, we would like to discuss the dynamic behavior the different SCNP topologies adopt in response to homogeneous shear flows. Different molecular architectures [27, 20, 35, 36]

exhibit a rich variety of reorientation dynamics under flow, which furthermore depend on the specific type of bonding potential [37, 24], excluded volume interactions [38] and the inclusion or exclusion of hydrodynamics [19, 37, 17].

The most commonly observed ordered motions of macromolecules under strong shear forces are tumbling and tank treading. The former presents a cycle of stretching in the flow followed by a collapse to a globule, during which the polymer flips its 'head' over its 'tail'. Tank treading, on the other hand, is characterized by the overall shape of the molecule remaining unchanged, while the individual monomers perform a rotation around its center-of-mass along its contour. The archetypal example of a tumbling polymer is the flexible linear chain, whose behaviour has been predicted theoretically [39, 40], extensively studied computationally [33, 41, 18, 42, 43] and confirmed experimentally by fluorescence imaging of large polymers such as DNA [1, 2, 3, 4]. Tank-treading can be observed in weakly deformable soft objects such as fluid droplets and vesicles [5, 6, 7, 8], but also in stiff ring polymers [24].

To determine whether SCNPs undergo tumbling or tank-treading motions, or a combination of both, we calculate two correlators, which are designed to uncover periodic conformational reorientations. The first of these is the cross-correlation of the diagonal elements of the gyration tensor in the flow and gradient directions [3, 44, 24, 21]

$$C_{xy}(t) = \frac{\langle \delta G_{xx}(0) \delta G_{yy}(t) \rangle}{\sqrt{\langle \delta G_{xx}^2(0) \rangle \langle \delta G_{yy}^2(0) \rangle}} \,, \tag{4.10}$$

where $\delta G_{\alpha\beta} = G_{\alpha\beta} - \langle G_{\alpha\beta} \rangle$ is the deviation of a component of G around its mean value. To understand why this correlator is typically used as a measure for tumbling, imagine one full tumbling cycle: Strong shear forces acting on the polymer lead to its extension in and alignment with the flow direction for large parts of the simulation. Entropically, this is unfavorable, as it decreases the conformational degrees of freedom and is in opposition to the polymer's tendency to adopt an isotropic shape. Thus, for $T > 0$, thermal fluctuations work against the shear forces and stochastically produce protrusions of parts of the polymer, especially the flexible ends, in the gradient direction. These unaligned protrusions are now pulled along the positive or negative flow direction by increased drag forces. This gives the polymer angular momentum, upon which it contracts to a coil, performs a quick 'head' over 'tail' rotation and subsequently extends in the flow direction again, completing the cycle.

As such, an extension (contraction) in the gradient direction (positive δG_{yy}) is followed by an extension (contraction) in the flow direction (positive δG_{xx}), producing a positive

correlation peak at $t_- = -\tau_{\text{tumbling}}/2$. On the contrary, an extension (contraction) in the flow direction leads to a contraction (extension) in the gradient direction, evidenced by a negative correlation peak at $t_+ = +\tau_{\text{tumbling}}/2$. The time between these two peaks, $\tau_{\text{tumbling}} = t_+ - t_-$, defines the tumbling frequency $f_{\text{tumbling}} = \tau_{\text{tumbling}}^{-1}$.
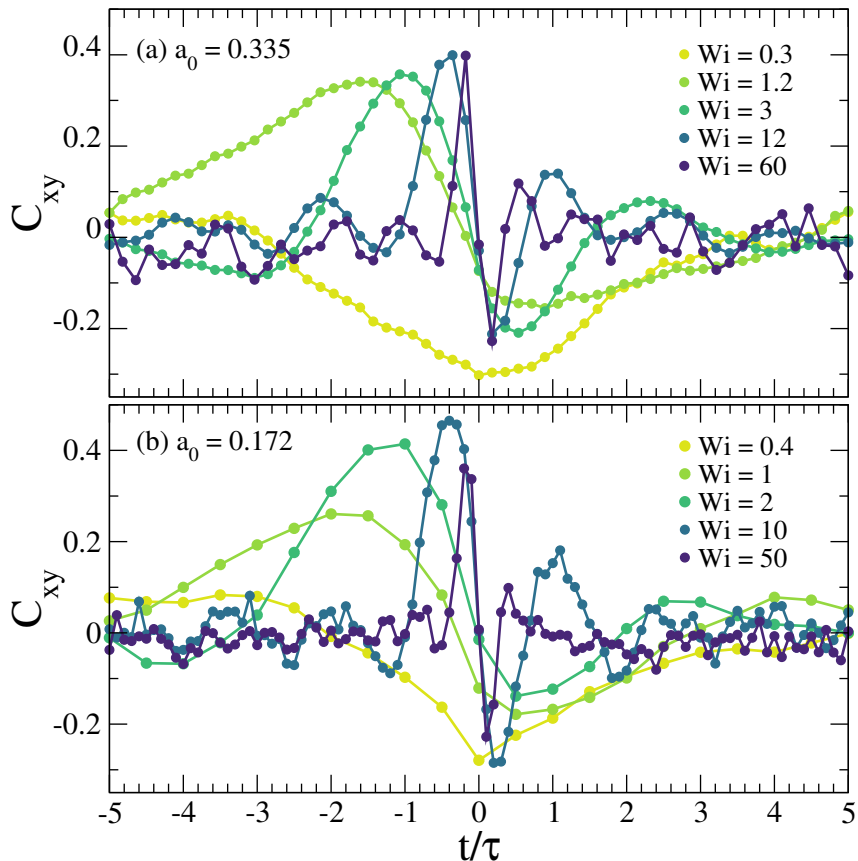

Figure 4.8: Flow-gradient extensional cross-correlation function $C_{xy}(t)$ for a SCNP of (a) intermediate and (b) low equilibrium asphericity. Times are rescaled by the longest relaxation time of the SCNP, τ_{r}.

To detect tank-treading, we need an approach that takes into account individual monomers instead of the extension or compression of the polymer as a whole, as tank-treading is defined by a pronounced lack of the latter. In a study of ring polymers, Chen *et al.* [24] introduced a monomer-based angular auto-correlation function for this purpose:

$$C_{\text{angle}}(t) = \frac{\langle A(0)A(t)\rangle}{\langle A^2(0)\rangle} \tag{4.11}$$

where $A(t) = \sin(2\beta)$ and β denotes the angle between the vector connecting a particular monomer to the center-of-mass and the largest eigenvector of the gyration tensor. These are instantaneous values at a given time and the average is performed over all monomers of the polymer. During tank-treading, the first principal component of the gyration tensor fluctuates very little, while the individual monomers steadily rotate around the

center-of-mass, producing a damped (by thermal noise) oscillatory signal in the angular auto-correlation function.
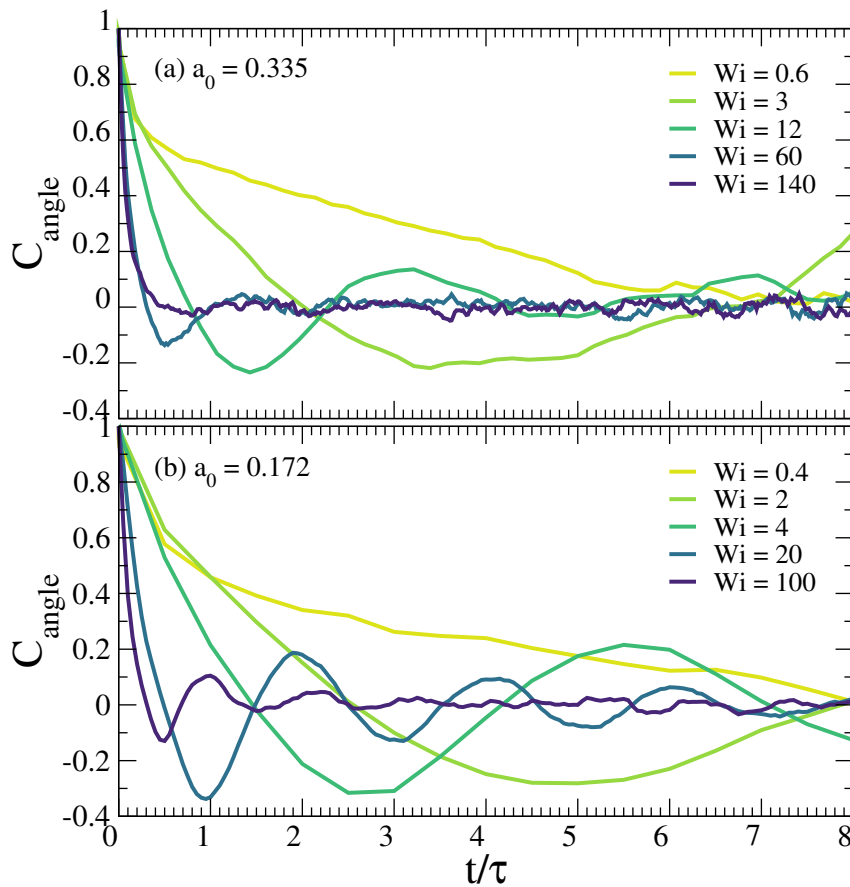

Figure 4.9: Angular auto-correlation function $C_{\mathrm{angle}}(t)$ for a SCNP of (a) intermediate and (b) low equilibrium asphericity. Times are rescaled by the longest relaxation time of the SCNP, τ_{r}.

We compare both the flow-gradient extensional cross-correlation function $C_{xy}(t)$ (Figure 4.8) as well as the angular auto-correlation function $C_{\mathrm{angle}}(t)$ (Figure 4.9) for a SCNP of intermediate (Panels (a)) and low equilibrium asphericity (Panels (b)). SCNPs of high asphericity qualitatively behave the same as those of intermediate asphericity (albeit producing more noise in the correlators) and are thus excluded from the discussion. We find coexistence of both tumbling and tank-treading signatures in the correlators $C_{xy}(t)$ and $C_{\mathrm{angle}}(t)$ in the range of low to intermediate Weissenberg numbers. At high Wi, a slightly different picture emerges: the SCNP of intermediate a_0 ceases to show any sign of tank-treading and instead shows a transition to pure tumbling cycles. For the low asphericity SCNP, tank-treading and tumbling motion continue to coexist up to the highest shear rate simulated. It should be noted that the high amount of noise present in the correlation functions is an effect of including hydrodynamic interactions. Performing the same simulation without hydrodynamics produces more well-defined, less damped oscillatory
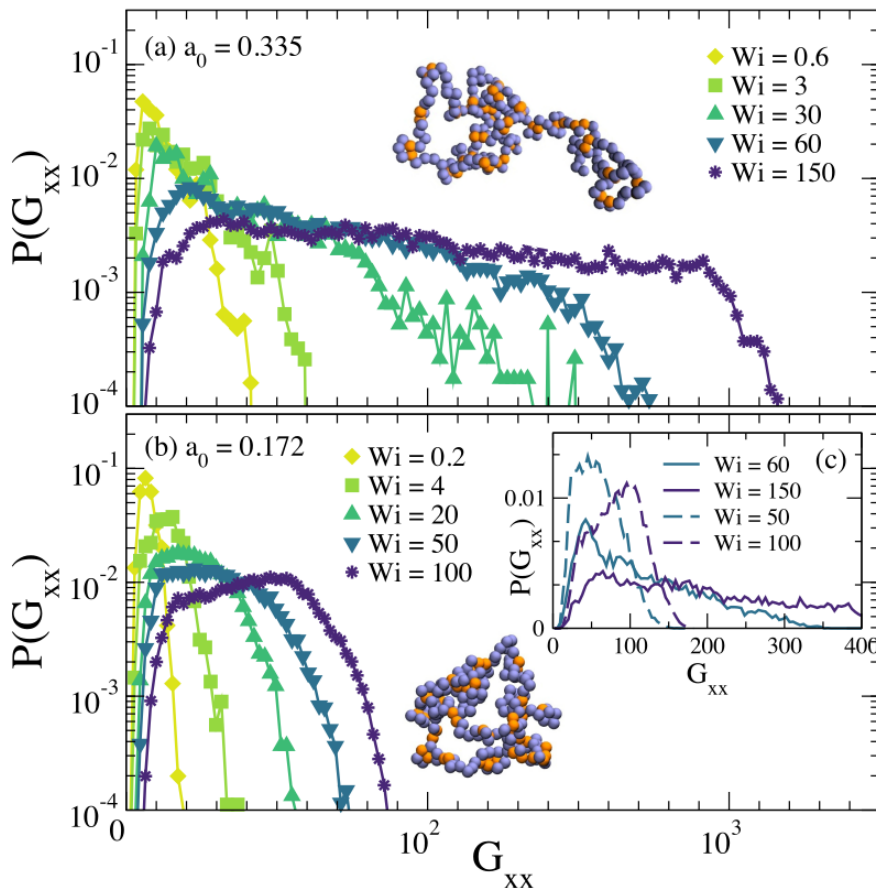
Figure 4.10: Probability distribution of G_{xx} as a function of the Weissenberg number Wi for a SCNP of (a) intermediate and (b) low equilibrium asphericity (log-lin scale). The inset (c) compares $P(G_{xx})$ of the two topologies (full lines: $a_0 = 0.335$, dashed lines: $a_0 = 0.172$) at intermediate and high Weissenberg numbers on a lin-lin scale. Snapshots of typical equilibrium conformations are included.

signals (not shown).

Since the correlators $C_{xy}(t)$ and $C_{\text{angle}}(t)$ do not provide any information about the relative importance of tumbling and tank-treading in a specific SCNP, we also include histograms of the instantaneous diagonal components of the gyration tensor in the flow direction, $P(G_{xx})$ (Figure 4.10). The distributions are both substantially broader and exhibit less pronounced maxima for the SCNP of intermediate asphericity at all Wi. For this SCNP, an increased shear rate has the predominant effect of an extreme broadening of the distribution, while leaving the position of the maximum relatively unaffected. The opposite is observed for the SCNP of low equilibrium asphericity: Its maximum shifts towards higher values of $P(G_{xx})$, even reversing the asymmetry of the distribution. These results confirm our interpretation that tumbling dominates the dynamics of the highly malleable SCNPs of high a_0, whereas tank-treading is the preferred motion for low a_0 SCNP.
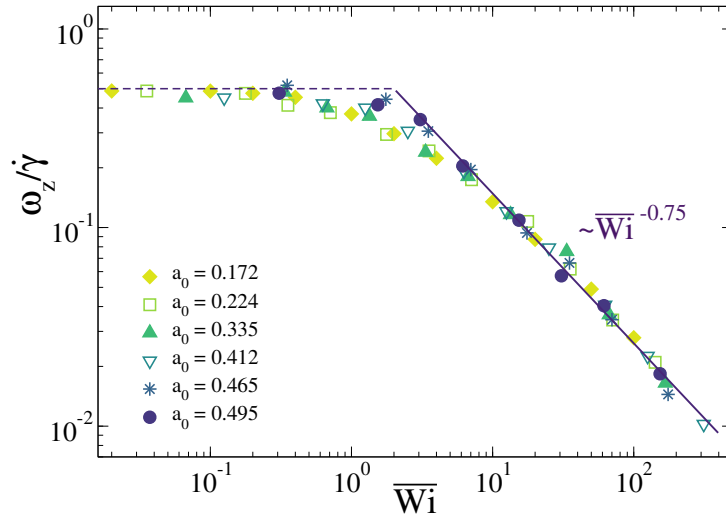
Figure 4.11: Rotational frequency ω_z as a function of the rescaled Weissenberg number $\overline{\text{Wi}}$ for SCNPs with different equilibrium asphericities.

In light of this, the tumbling signatures observed in the low a_0 SCNP should perhaps be interpreted in terms of the 'breathing' cycles of star polymers [37, 45]. As pointed out by Sablić *et al.* [37], the anti-correlation peaks in the flow-gradient extensional cross-correlation function $C_{xy}(t)$ do not necessarily indicate any rotational movement of the polymer, but can also be related to so-called 'breathing' modes, during which a polymer periodically expands and retracts without reversing its orientation with respect to the flow field. To analyze the rotational motion of SCNPs under flow, we calculate the rotational frequency in the vorticity direction according to the geometrical approximation [46, 47]

$$\omega_z/\dot{\gamma} = \frac{\langle G_{yy} \rangle}{\langle G_{xx} \rangle + \langle G_{yy} \rangle} \,. \tag{4.12}$$

Note that this formula is based on the relation $\boldsymbol{L} = \mathbf{J}\boldsymbol{\omega_L}$ between the angular momentum $\boldsymbol{L}$ and the inertia tensor $\mathbf{J}$ and thus treats the polymer as a rigid body of the average shape of the given polymer. Interpretation of ω_z further suffers from the inclusion of rotational vibrations, which should be treated separately to accurately determine a molecule's long-term rotation. Recent studies [45, 36] have tackled this shortcoming by using a co-rotating Eckart frame [48] to decouple angular vibrations and persistent rotations. Taking a similar approach is beyond the scope of this work, but we believe that an in-depth analysis of the rotational dynamics employing the Eckart frame formalism could deepen our understanding of the complex dynamics of SCNPs in future studies.

Theoretical arguments predict the rotational frequency of soft objects to scale linearly with the shear rate for low Wi and therefore we represent our results in terms of a reduced

rotational frequency $\omega_z/\dot{\gamma}$ versus $\overline{\mathrm{Wi}}$ in Figure 4.11. The expected plateau at small $\overline{\mathrm{Wi}}$ is exhibited by all SCNP topologies, whereas a universal scaling law emerges at high Wi, following $\omega_z/\dot{\gamma} \sim \mathrm{Wi}^{-0.75}$. Given the different dynamic signatures present in $C_{xy}(t)$ and $C_{\mathrm{angle}}(t)$ for low and high asphericity SCNPs at high shear rates, the common scaling found is rather surprising. Together with the strong dispersion of scaling exponents in different polymer topologies seen in Table 4.1, this might be taken as further evidence for the problematic interpretation of ω_z as a steady rotation.

4.3.2 Semi-dilute poly- and monodisperse solutions

Having established the universal power laws governing the structural changes SCNPs of different topologies undergo when subjected to shear flows, we now turn our focus to the investigation of semi-dilute and concentrated solutions. Since the stochastic cross-linking process leads to the synthesis of a set of structurally and topologically polydisperse nanoparticles, we are interested in distinguishing between the effect of the intrinsic poly-dispersity of SCNP solutions and the effect of the randomly cross-linked topology itself. Therefore, we run simulations on four different systems: The first is a polydisperse solution of SCNPs chosen randomly from the whole range of topologies. The other three are monodisperse solutions made up of replicas of one particular SCNP topology of either low, medium or high asphericity. For the remainder of this chapter, the concentration of the solution, $\rho = N_\mathrm{m}/V$, will be reported in reduced units, $\rho/\rho^\star$, where $\rho^\star$ is the overlap concentration. It is defined as the number density of monomers of a single polymer within a cube of side length $2R_\mathrm{g}$ (the radius of gyration at infinite dilution), i.e. $\rho^\star = N(2R_\mathrm{g})^{-3}$. For concentrations beyond the overlap concentration, monomers of different polymers start to enter the same space, possibly distorting each other's conformations with respect to dilute conditions. In equilibrium, most polymer architectures undergo a crossover to a different size scaling regime beyond the overlap concentration. For example, linear chains transition from self-avoiding to Gaussian chains, while SCNPs have been shown to collapse to crumpled globules [49, 50]. In this chapter, we explore concentrations in the range of $0.25 \le \rho/\rho^\star \le 6.24$, the highest of which corresponds to a monomer concentration of $\rho = 0.38$, or about 300-400 mg/mL [49]. We expect the SCNPs to be unentangled up to the highest concentration considered. The reasoning behind this lies in a quick estimation for linear chains of the same polymerization degree ($N = 200$): In good solvent conditions their entanglement concentration is given by $\rho_\mathrm{e} \approx (N_\mathrm{e}/N)^{3\nu_\mathrm{F}-1}$ where N_e denotes the entanglement length in the melt and $\nu_\mathrm{F} = 0.59$ the Flory exponent [51]. The entanglement length depends on the polymer model and is $N_\mathrm{e} \gtrsim 65$ for the bead-spring model employed here [52, 53]. This leads to an entanglement concentration of $\rho_\mathrm{e} \gtrsim 0.42$, which lies above the highest monomer concentration investigated here. Since the permanent loops render SCNPs less penetrable, their effective entanglement length will be higher than that of linear polymers, further increasing their entanglement concentration ρ_e [54].

We explored shear rates in the range of $5 \times 10^{-5} \le \dot{\gamma} \le 2 \times 10^{-2}$. As in the previous section on single-molecule simulations, we scale the shear rate by the relaxation time τ_r and represent all results as a function of dimensionless Weissenberg number $\mathrm{Wi} = \dot{\gamma}\tau_\mathrm{r}$.

For the polydisperse solutions, we compute a mean relaxation time over all 200 SCNP topologies, $\tau_{\mathrm{r,poly}} \approx 10^4 \sqrt{ma^2/k_B T}$.
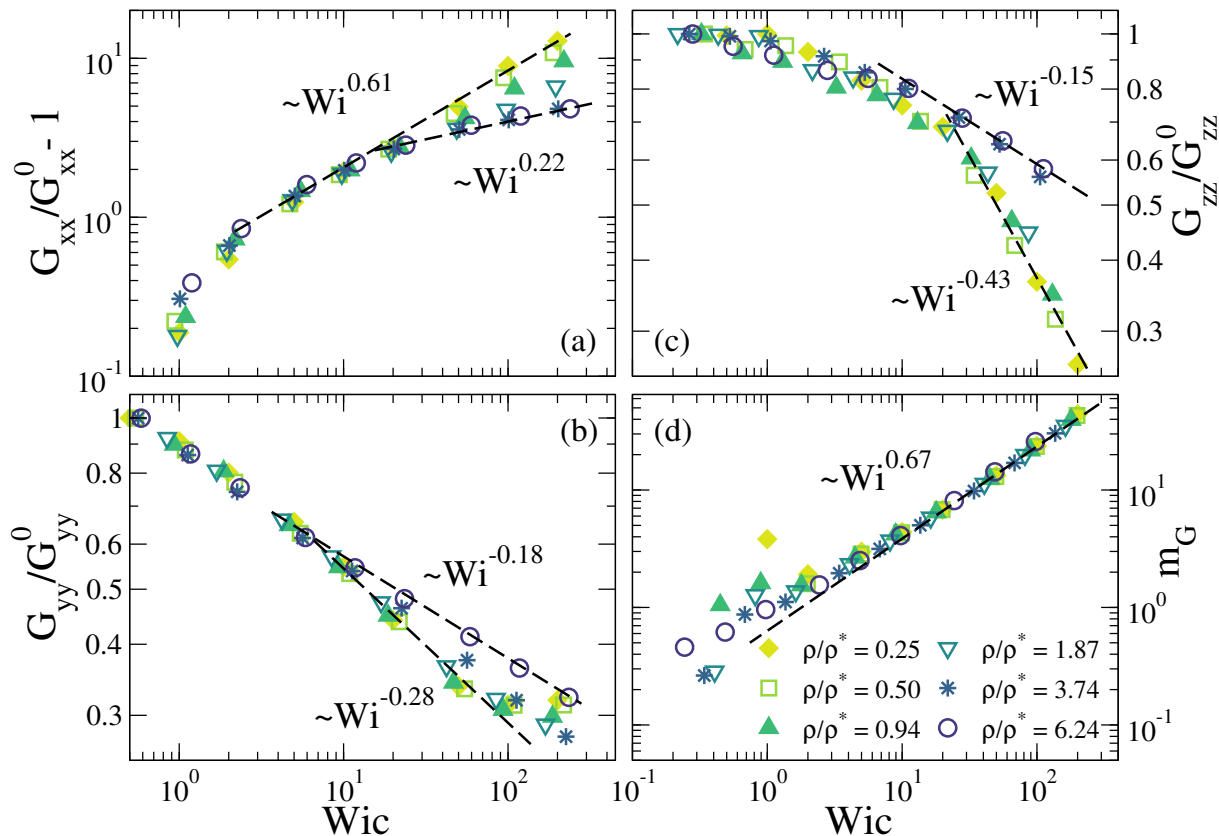
Structural properties

Figure 4.12: Normalized diagonal components of the inertia tensor (a-c) and orientational resistance (d) vs. density-dependent Weissenberg number for the polydisperse solutions. Dashed lines represent power laws.

We begin our analysis by characterizing the structural changes the SCNPs undergo in different directions of the shear flow geometry. Panels (a-c) of Figure 4.12 depict the diagonal components of the gyration tensor in the flow (G_{xx} (a)), gradient (G_{yy}, (b)) and vorticity (G_{zz} (c)) directions, respectively. Data are shown for the polydisperse solutions and are normalized by their values at the lowest shear rate explored, $G_{\mu\mu}^0$. We rescale the Weissenberg number by a density-dependent factor to obtain the best overlap with the data set at the lowest concentration $\rho/\rho^\star = 0.25$, similar to the topology-dependent factor we employed in the previous chapter. This rescaling is inspired by computational studies on semi-dilute solutions of linear chains and star polymers [55, 56, 47], which found master curves for the components of the gyration tensor, independent of density, after rescaling data with such a density-dependent factor. For the remainder of this

chapter, representations of observables as a function of shear rate will always be reported as a function of density-dependent Weissenberg number Wic.

Contrary to linear chains and star polymers, we find two distinct scaling regimes, one at low and one at high concentration, for all components of the gyration tensor, which emerge at high shear rates Wi $\gg$ 1 after a prior universal scaling at low shear rates Wi $\lesssim$ 10. The cross-over between the two limiting scaling regimes takes place around the overlap concentration, albeit at a slightly different concentration for each component of G. These differences can be explained by the asymmetric change in shape under shear flow, which leads to the polymers effectively overlapping at different concentrations in different directions. The second scaling regime found for concentrations well beyond the overlap concentration is characterized by a weaker perturbation of the polymers' structure by the flow, as evidenced by the smaller scaling exponent compared to the one obtained below the overlap concentration. As such, it appears that the interactions with the surrounding molecules effectively shield the SCNPs from the frictional forces between different fluid layers. Remarkably, these changes in extension and compression of the shape of SCNPs upon increasing the concentration of the solution do not affect the average orientation in the flow-gradient plane, as can be seen from the orientational resistance (Equation 4.5) depicted in Figure 4.12(d). Indeed, we find a power law $m_{\mathrm{G}} \sim \mathrm{Wic}^{\mu}$ with the exact same scaling exponent $\mu = 0.67$ reported earlier in infinite dilution (see Figure 4.6).

To further highlight the pronouncedly different response to shear flow between dilute and concentrated SCNP solutions, we show the Wi-dependence of the rotational frequency ω_z and the polymer contribution to the viscosity η_{p} (Equation 4.7) for the polydisperse solution in Figure 4.13. The rotational frequency is calculated via the angular momentum $\boldsymbol{L}$ and the inertia tensor $\mathbf{J}$ according to the relation $\boldsymbol{L} = \mathbf{J}\boldsymbol{\omega}$. The observables ω_z and η_{p} exhibit the same qualitative behavior as the diagonal components of the gyration tensor, displaying a universal scaling at low Wic, which transitions into two distinct scaling regimes for low and high concentrations at high Wic. We plot the rotational frequency normalized by the shear rate $\dot{\gamma}$ as in Figure 4.11, because of the linear scaling $\omega_z \sim \dot{\gamma}$ expected at low shear rates and indeed found for individual SCNPs at Wi $\ll$ 1. Interestingly, while the scaling exponent for the normalized rotational frequency below the overlap concentration coincided with the one found for individual SCNPs at Wi $\gg$ 1, it is increased from $\mu = -0.75$ to $\mu = -0.34$ upon increasing the concentration to $\rho/\rho^{\star} = 3.74$, indicating that the rotation of the SCNPs is less hindered (compared to small shear rates) at high concentrations than at low concentrations. The opposite effect is found for the viscosity: shearing at high densities leads to a stronger reduction of η_{p} than at low
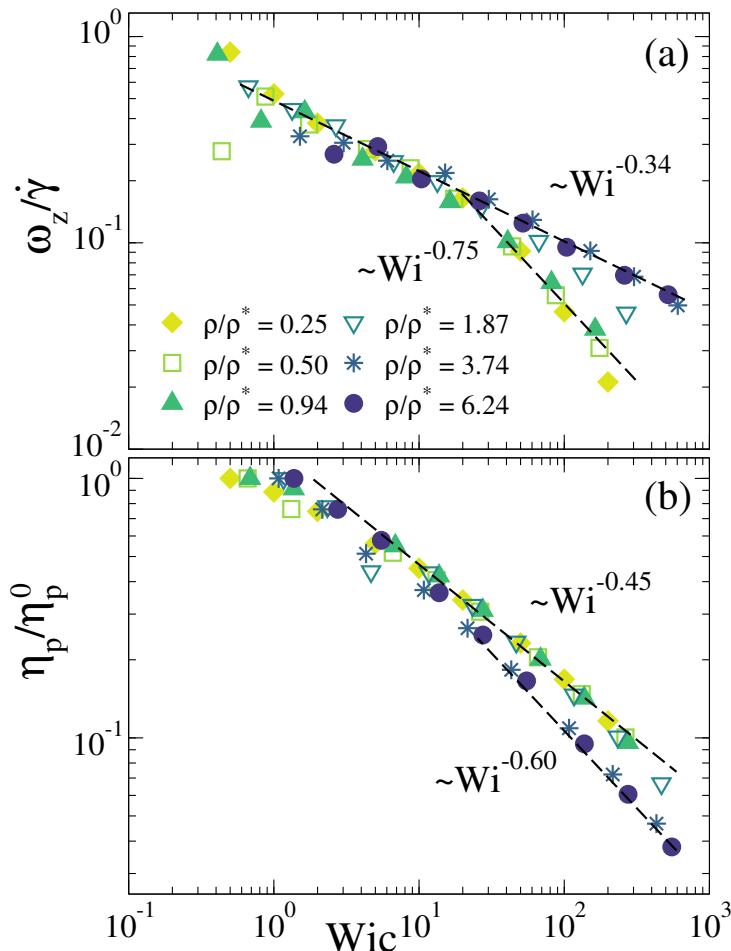
Figure 4.13: As 4.12 for the rotational frecuency scaled by $\dot{\gamma}^{-1}$ (a) and the polymer contribution to the viscosity (b).

densities. This is most likely due to the high number of monomer contacts and the strong steric repulsion experienced by SCNPs in concentrated solutions, such that stretching in the flow direction leads to a more efficient packing of the SCNPs and thus a stronger decrease in excluded volume interaction.

So far, we have only discussed the behavior of the polydisperse solutions, since they are experimentally more relevant. This is due to the fact that an efficient procedure for separating SCNPs of different topologies has not been reported yet, even though some of the techniques proposed for segregating linear and ring polymers [57, 58, 59, 60, 61, 62, 63] might be worth exploring for SCNPs. However, comparing polydisperse and monodisperse solutions helps discerning between the effect of polydispersity and the effect of the universal characteristics of SCNPs as a separate class of nanoparticles (see discussion of Chapter 4.3.1). For all the characteristics discussed so far, we observe qualitatively the same behavior in the monodisperse solutions, even though the specific exponents differ slightly. Thus, to rationalize the density-dependent response in the high-Wi regime, we

show representative snapshots of the monodisperse solutions consisting of either a low or a high equilibrium asphericity SCNP in Figures 4.14 and 4.15, respectively.
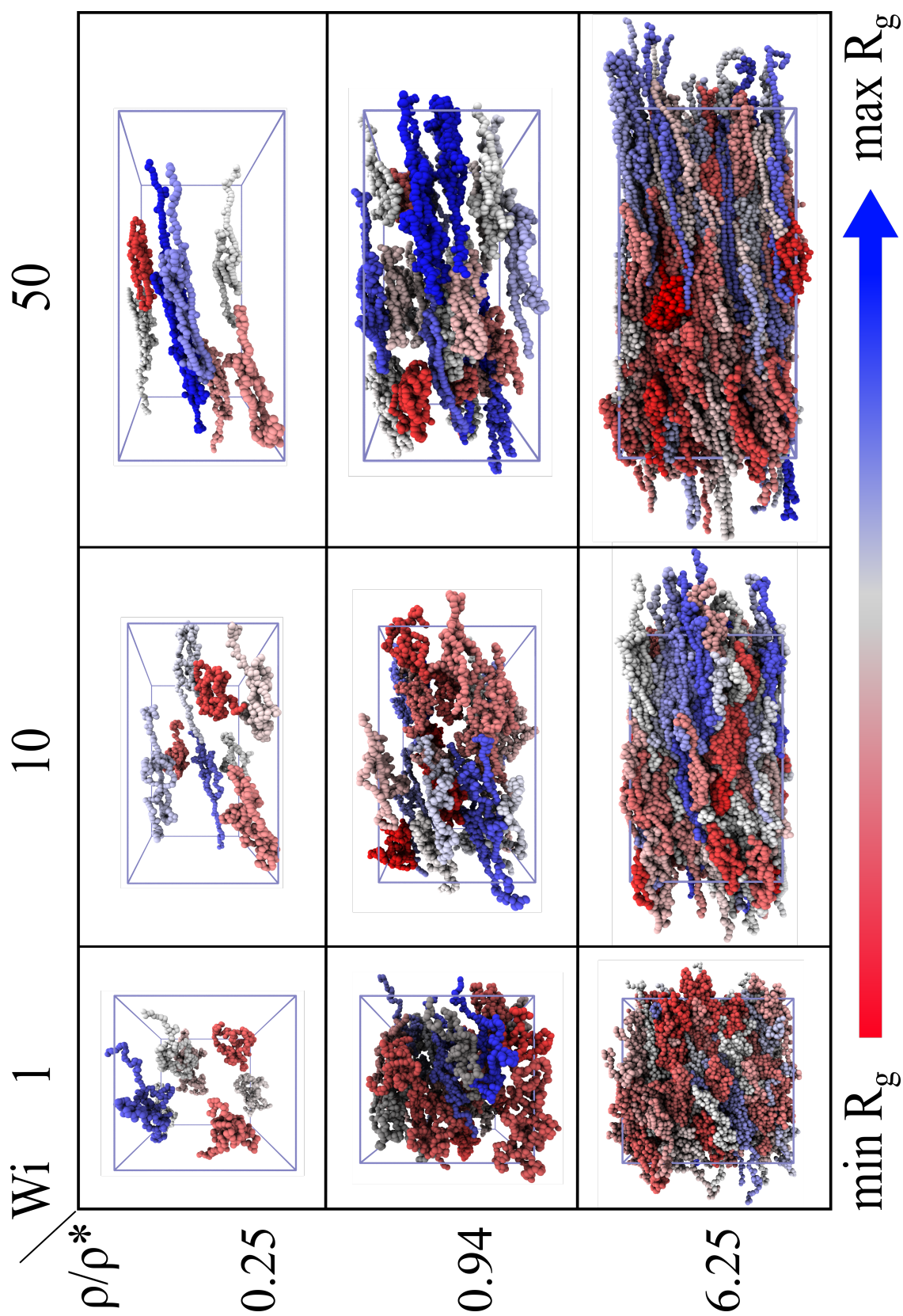
Figure 4.14: Snapshots of the simulation box for the monodisperse solution of SCNPs of low equilibrium asphericity $a_0 = 0.18$, at different values of the Weissenberg number and the concentration. Individual SCNPs are colored according to their instantaneous radius of gyration (dark red to dark blue from lower to higher R_g).
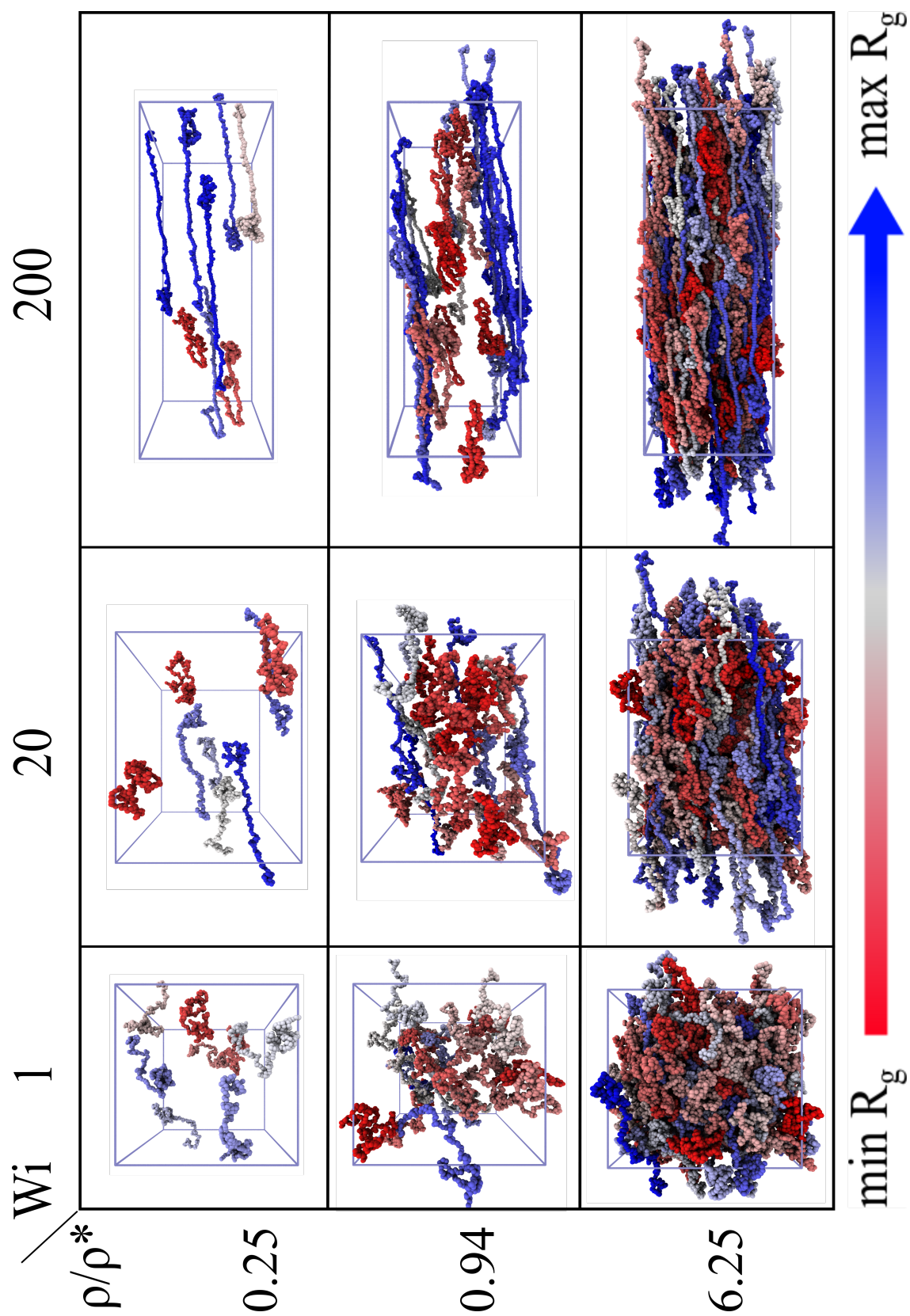
Figure 4.15: As Figure 4.14 for the monodisperse solution of SCNPs of high equilibrium asphericity $a_0 = 0.47$.

Each SCNP is colored according to its instantaneous radius of gyration on a scale from dark red (corresponding to the minimum R_{g} at a particular Wi, $\rho/\rho^{\star}$-combination) to dark blue (corresponding to the maximum R_{g}). The snapshots highlight the segregation and impenetrability of individual SCNPs due to their topological interactions at all shear rates and densities. Furthermore, we observe a weak transient demixing of elongated and compressed SCNPs at intermediate and high shear rates. We especially find elongated SCNPs to be often aligned with other simultaneously elongated SCNPs, which might stem from an effective depletion interaction between instantaneously stretched SCNPs conveyed by the smaller collapsed SCNPs. We believe the intrinsic impenetrability of SCNPs is the driving force behind their density-dependent response, as it hinders the strong elongation in the flow direction observed in high dilution.

To gain deeper insight into how density affects the SCNPs' response to shear, we choose to discuss certain observables in the equivalent, but conceptually different manner, of plotting them as a function of density instead of Wi. In Figure 4.16, we plot the radius of gyration and the orientational resistance in this fashion, where each data set corresponds to a fixed Weissenberg number and is normalized by its value at $\rho/\rho^* = 0.25$. For any given Wi, increasing the concentration leads to a reduction of the orientational resistance m_{G}, indicating that the SCNPs tend to be more aligned with the flow as the solution becomes more crowded.

Representing R_{g} as a function of density reveals a much more complex behavior. We include data for equilibrium conditions (Wi = 0), where an increase in density collapses the SCNPs to crumpled globules [49]. Shrinking continues in weakly sheared solutions for which Wi $\leq$ 1, but stops at intermediate shear rates $1 \leq$ Wi ≤ 20, where adding more SCNPs to the solution, even up to $\rho/\rho^{\star} \sim 6$ does not affect their mean size, since they are sufficiently elongated to fill the space without significant contacts between neighboring molecules. Further increasing the shear rate leads to a partial reversal of this trend. For Wi > 20, we observe a non-monotonic ρ-dependence of the molecular size: Increasing the concentration shrinks the SCNPs up to $\rho/\rho^{\star} \sim 4$, beyond which they start to swell again. To highlight the novelty of this behaviour, in Figure 4.23(a) we include data sampled from studies of linear chains under homogeneous shear flows employing the same computational methods we use here [34]. While showing the same qualitative trends at low to intermediate shear rates, i.e. shrinking upon increased density for low shear rates and swelling for intermediate shear rates, linear chains never re-enter a regime in which they shrink in size, even for such high shear flows as Wi = 2400, a lot higher than the highest in our study. Furthermore, the swelling under mildly sheared flows is a lot stronger
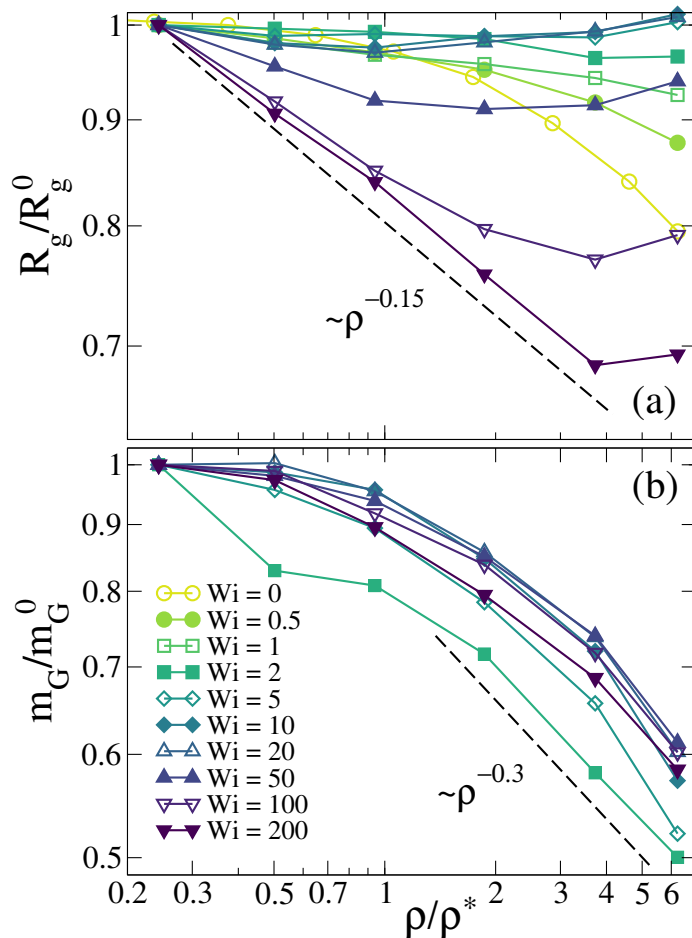
Figure 4.16: For the SCNPs in the polydisperse solutions, gyration radius (a) and orientational resistance (b) vs. concentration. Each data set corresponds to a fixed Weissenberg number (see legend) and is normalized by the value (R_g^0, m_G^0) at its corresponding Wi and concentration $\rho/\rho^* = 0.25$. Dashed lines represent power laws.

in linear chains and is only less pronounced at higher shear rates because the chains are already close to the rod-limit in dilute conditions. It appears that a 'pseudonematic' ordering is more favorable in the more flexible linear polymers as they can compensate the loss of conformational entropy with a gain in vibrational and translational entropy.

Since the radius of gyration is given by $R_g^2 = G_{xx} + G_{yy} + G_{zz}$, we report the diagonalized components G_{xx} of the gyration tensor in the same manner as R_g in Figure 4.17. We observe that the trends in $R_g(\rho/\rho^\star)$ are primarily driven by the dominant contribution of G_{xx}, which follows the same qualitative trend. The extension in the gradient direction, G_{yy}, on the other hand, exhibits no re-entrant behavior, but is, as in other architectures, a monotonically decreasing function of density, for all Weissenberg numbers. Finally, we note that G_{xx} and G_{zz} qualitatively follow opposite trends in their dependence on concentration, reflecting the intrinsic elasticity of SCNPs due to their permanent cross-
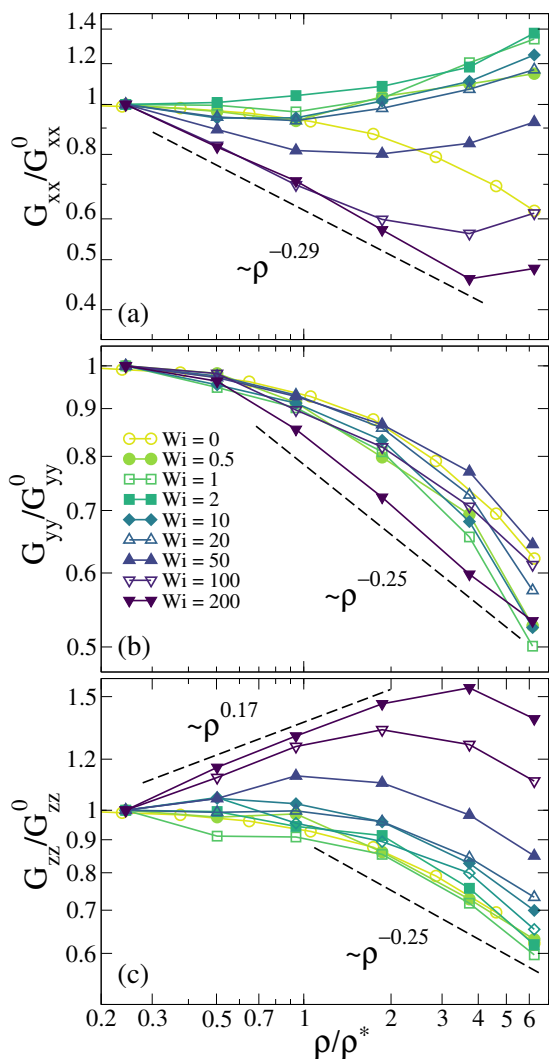
Figure 4.17: Normalized diagonalized components of the gyration tensor vs. concentration for the polydisperse solution. Representation as in Figure 4.16
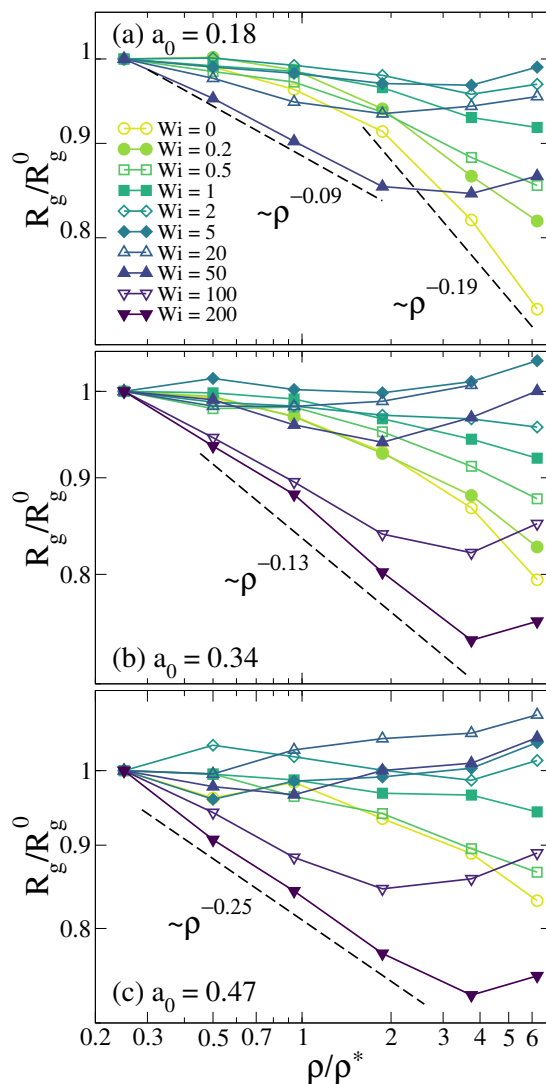
.

Figure 4.18: Radius of gyration vs. concentration for monodisperse solutions of equilibrium asphericities $a_0 = 0.18$ (a), 0.34 (b) and 0.47 (c). Representation as in Figure 4.16

links.

As mentioned earlier, the characteristic behavior exhibited by SCNPs is not related to a complex interplay of the various time-scales present in the system due to its topological polydispersity. This is demonstrated in Figure 4.18, where we present the same results as in Figure 4.16a, but for the three different monodisperse solutions. They all experience qualitatively the same non-monotonic change in average molecular size as a function of $\rho/\rho^\star$ and Wi. Quantitatively, the SCNPs of highest asphericity are also the most deformable, showing the greatest response to increased crowding, both in terms of swelling and shrinking, as evidenced by the highest exponent in the approximate scaling $R_{\mathrm{g}} \sim \rho^{-\alpha}$
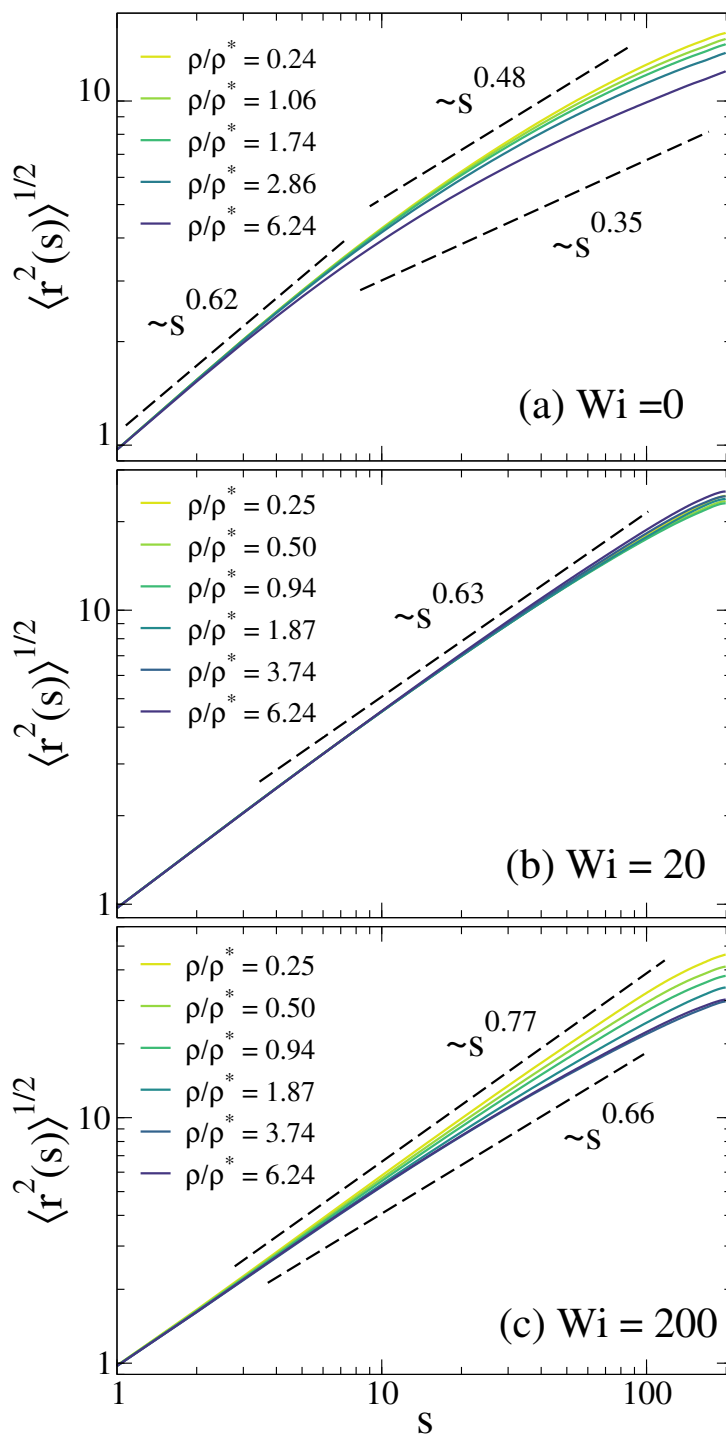
at Wi = 200.

Figure 4.19: For the SCNPs in polydisperse solutions, contour distance vs. euclidean distance at fixed Weissenberg numbers Wi = 0 (a), Wi = 20 (b) and Wi = 200 (c). Dashed lines represent approximate power laws.

The microscopic origin of the complex dependence of the SCNP size on concentration and shear rate can be elucidated by analyzing their intramolecular structure. In Figure 4.19 we plot the average Euclidean distance between any two given monomers i, j, $r =$

$\langle (\boldsymbol{r}_j - \boldsymbol{r}_i)^2 \rangle^{1/2}$, as a function of their contour distance s at three different shear rates: In equilibrium Wi = 0 [50], for Wi = 20 and Wi = 200. The contour distance is defined as the distance between two monomers that an observer walking along the backbone of the linear precursor polymer would measure. If we label the monomers in ascending order according to their position in the linear backbone $i = 1, 2, ..., N$, this amounts to $s = |i - j|\sigma$. The observable $r(s)$ provides information about the intramolecular monomer distributions and correlations. It generally follows a scaling law $r(s) \sim s^\nu$ with exponent ν, which is related to the scaling of the form factor in the fractal regime.

For SCNPs in equilibrium (Wi = 0, Panel (a)), $r(s)$ displays three regimes: At short scales ($s < 10$), it is indistinguishable from that of linear polymers in good-solvent conditions, following a scaling law with exponent $\nu = 0.6$ similar to the Flory exponent of self-avoiding walks. Beyond that, the effect of permanent loops becomes evident, making small distances between monomers separated by a large contour distance more likely. In dilute conditions, this results in a second scaling regime with $\nu \sim 0.5$, similar to linear chains in a θ-solvent [51], reflecting the local compaction but overall sparse character of the majority of SCNPs. Increasing the concentration above the overlap density leads to a transition to a smaller exponent of $\nu \sim 0.35$, consistent with their crumpled globular conformations (discussed in detail in Chapter 3). Finally, the Euclidean distance converges to a plateau at large s due to the existence of a small amount of long-range loops in the SCNPs. One should keep in mind that the polymerization degree N of the SCNPs affects the range of contour distances for which the second scaling regime can be observed and possibly also the effective exponents.

The intramolecular correlations cease to be affected by density at intermediate shear rates (Wi = 20 in Figure 4.19(b)), which is consistent with the marginal effect density has on R_g in the range of $2 \lesssim \mathrm{Wi} \lesssim 50$ (see Figure 4.16(a)). The elongation in the flow direction is reflected in a larger scaling exponent $\nu = 0.63$ than in equilibrium, but remains very far from the straight rod limit ($\nu_\mathrm{R} = 1$). Such conformations are only approached at very high Weissenberg numbers and high dilution (Wi = 200, Figure 4.19(c)), where $\nu \sim 0.8$. However, changes in concentration have a strong effect at high shear rates: Consistent with the decrease in R_g, we find a transition to a significantly lower exponent of $\nu \gtrsim 0.6$ at the highest density considered.

As can be seen in Figure 4.20(a), we find that the rotational frequency as a function of the concentration shows a strong correlation with the z-component of the gyration tensor (see Figure 4.17). It appears that swelling along the vorticity direction in combination with
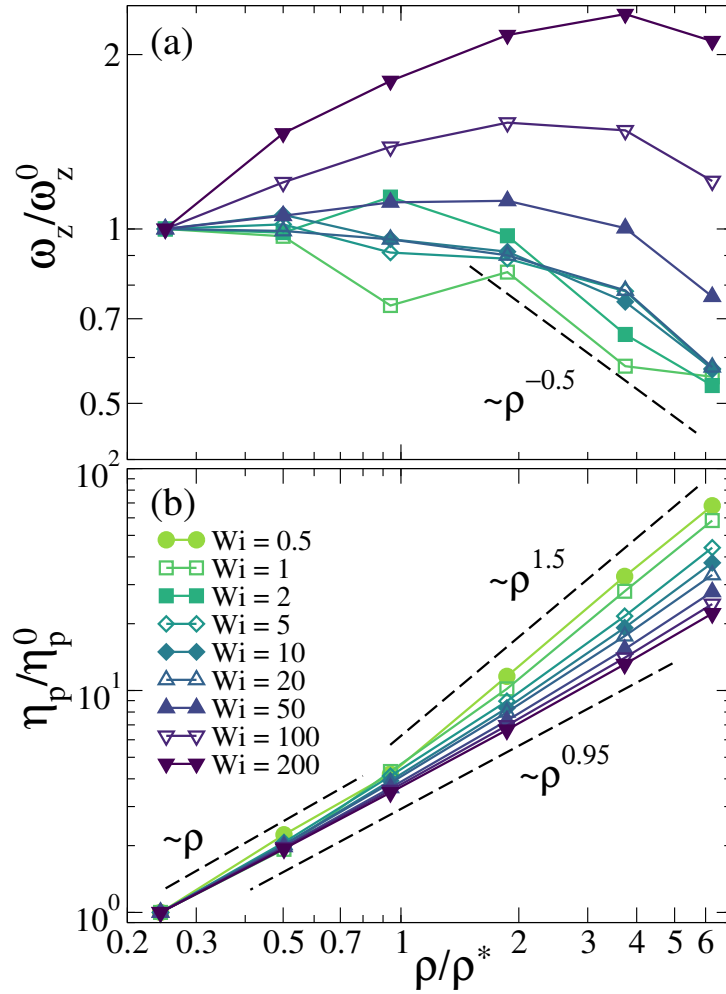
Figure 4.20: As Figure 4.16 for the rotational frequency (a) and the polymer contribution to the viscosity (b).

compression in the flow-gradient plane facilitates rotations around the vorticity directions. This can be rationalized very intuitively as the rotational energy is given by $E_{\mathrm{rot}} = \frac{1}{2}\mathbf{J}\boldsymbol{\omega}^2$, which explicitly amounts to $E_{\mathrm{rot},z} = \frac{1}{2}\sum_{i=1}^N m_i \left(x_i^2 + y_i^2 - x_i z_i - y_i z_i\right)\omega_z^2$ for a rotation around the z-axis. Thus, an increase in either G_{xx} or G_{yy} increases the energy for a rotation around the z-direction substantially.

Rheological Properties

We now turn our discussion to the viscosity as a function of density, reported in Figure 4.20(b). We find two regimes, a single scaling for all Weissenberg numbers below the overlap concentration and a Weissenberg dependent power law $\eta_{\mathrm{p}} \sim \rho^x$ above $\rho^\star$. For $\rho \ll \rho^*$, the polymer contribution to the viscosity increases linearly with the concentration, as expected for dilute conditions. Beyond the overlap concentrations the exponents range

between $x = 0.95$ for Wi $\gtrsim 100$ and $x = 1.5$ for Wi $\lesssim 1$. The latter lies in between the values for semidilute solutions of linear chains in good ($x = 1.3$) and θ-solvent ($x = 2$) conditions in equilibrium [51]. The regime of shear rate dependent power laws with $\eta_{\mathrm{p}} \sim \rho^x$ can be explained by a simple scaling argument. In unentangled semi-dilute solutions of fractal objects whose size scales as $R \sim N^\nu$, the overlap concentration should follow

$$\rho^* \sim N R^{-3} \sim N^{1-3\nu} \,, \tag{4.13}$$

where R and N is the object's size and number of monomers, respectively. We find for our system that $\eta_{\mathrm{p}} \sim (\rho/\rho^*)^x$, so that if we insert Equation 4.13, we arrive at

$$\eta_{\mathrm{p}} \sim \rho^x N^{(3\nu-1)x} \,. \tag{4.14}$$

If we assume that in semi-dilute solutions, hydrodynamic interactions are screened on length-scales bigger than the mesh-size, the viscosity would furthermore scale linearly with the molecular mass,

$$\eta_{\mathrm{p}} \sim N \,. \tag{4.15}$$

Equating 4.14 and 4.15, we finally arrive at the following relation between the scaling exponents x and ν:

$$(3\nu - 1)x = 1 \,. \tag{4.16}$$

According to this relation, the exponents we find for the viscosity $x = 1.5, 1.1, 0.95$ at the representative values Wi $= 1, 20, 200$ should originate from exponents for the intramolecular structure $\nu = 0.56, 0.64$ and 0.68, respectively. We can check the validity of this scaling argument by comparing these values to the scaling exponents expressed in $r(s)$, whose values at the given Weissenberg numbers, $\nu = 0.52, 0.63$ and 0.66 are in good agreement with the theoretical calculation (taking into consideration the error in the estimation of ν due to the relatively small N of the SCNPs). We further test our scaling argument on data sampled from linear chains [34] (see Figure 4.23, whose viscosity shows a weaker dependence on Weissenberg number. Following the same relation as SCNPs (see Equation 4.16), the observed exponents $x = 1.2$ (low concentration, low Wi) and 0.8 (high concentration, high Wi) should stem from a scaling of the intramolecular structure $R \sim N^\nu$ with exponents $\nu = 0.61$ and 0.75, respectively, which is consistent with the limits of self-avoiding random walks ($\nu_{\mathrm{F}} = 0.59$) and almost rod-like conformations ($\nu_{\mathrm{R}} = 1$), respectively.
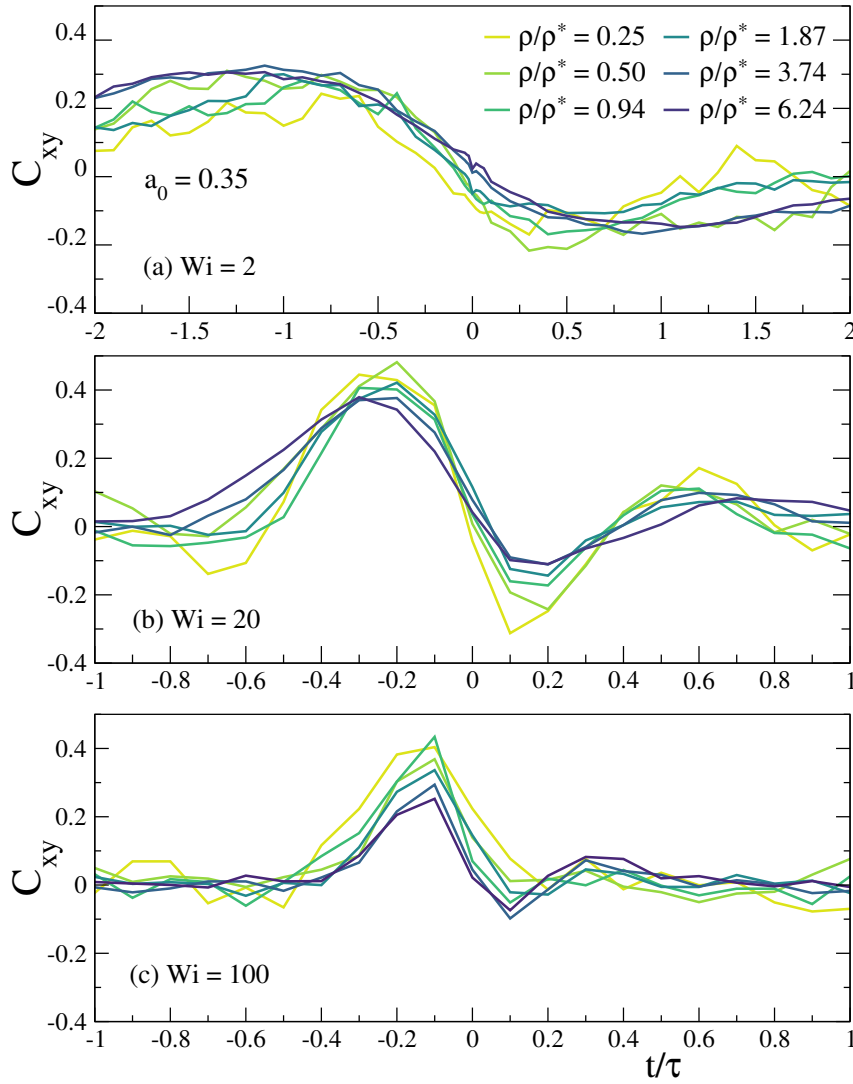
Figure 4.21: Cross-correlator $C_{xy}(t)$ for the monodisperse solutions of SCNPs of intermediate equilibrium asphericity $a_0 = 0.34$, at Weissenberg numbers Wi $= 2, 20$ and 100 (panels (a), (b) and (c), respectively). Each data set corresponds to a fixed value of the concentration (see legend).

Dynamic behaviour

Further insight into the structural changes upon increasing the density at different shear rates might be gained from investigating the dynamical behaviors underlying these changes. Especially, we would like to know if tumbling is reduced or prevails in solutions beyond the overlap density, since the interplay between steric interactions hindering tumbling and the conformational entropy gained from it makes a prediction difficult. We characterize tumbling via the flow-gradient cross-correlation of the gyration tensor $C_{xy}(t)$ as defined in Equation 4.10 of Chapter 4.3.1. The different relaxation times – and thus different tumbling frequencies – of the SCNPs in the polydisperse solutions complicate an interpretation of the average $C_{xy}(t)$, so we report results for the monodisperse solutions instead in
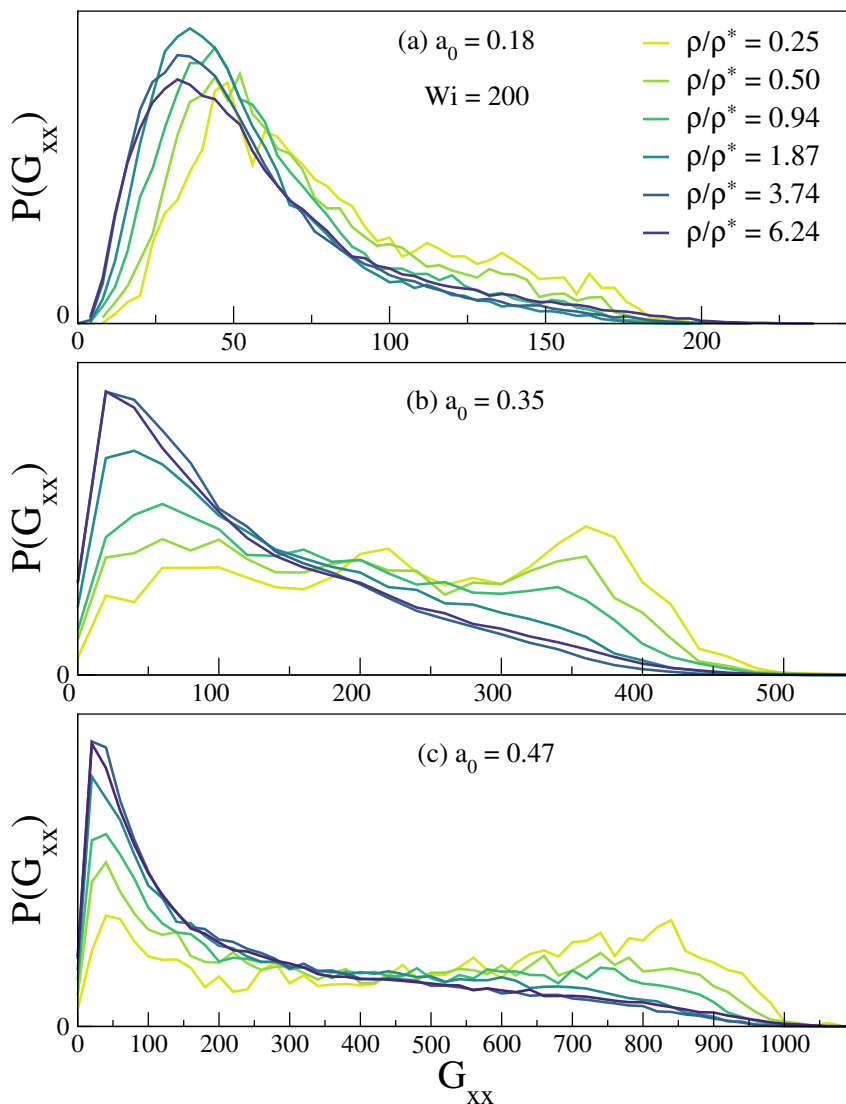
Figure 4.22: Distribution of instantaneous x-components of the inertia tensor for the monodisperse solutions, at high Weissenberg number (Wi = 200), of SCNPs with equilibrium asphericities $a_0 = 0.18$ (a), 0.34 (b) and 0.47 (c). Each data set corresponds to a value of the concentration (see legend).

Figure 4.21, since we have shown that the qualitative behavior of both monodisperse and polydisperse solutions is the same for all static observables. All monodisperse solutions exhibit the characteristic anti-correlation peaks in $C_{xy}(t)$ at a high Weissenberg number of Wi = 200 even up to the highest density. The amplitudes of the peaks decay systematically upon increasing the density of the solution, which does not necessarily mean that the SCNPs tumble less, but could also be interpreted as their tumbling motion being less well defined.

Investigating the distribution of instantaneous values of the gyration tensor in the flow direction (G_{xx}) should help elucidate the change in tumbling dynamics, since a tumbling cycle is characterized by a strong fluctuation of G_{xx} over its course. Figure 4.22 shows

the histograms of G_{xx} for the monodisperse solutions, (a-c) corresponding to the same state points as in Figure 4.21. Interestingly, crowding strongly decreases the prevalence of highly elongated (high G_{xx}) conformations, while it increases the amount of time SCNPs spend in more collapsed (low G_{xx}) conformations. During a tumbling cycle, the polymer has to flip its tail over its head while it is in a collapsed state. Unlike a linear chain, which can achieve this by sliding one segment over the other without significantly growing in the gradient direction, the cross-links of SCNPs necessitate a greater extension in the y-direction during this rotation. The presence of other molecules crowding the solution would thus hinder the tail-over-head flip, leading to the SCNPs remaining in the collapsed phase of the tumbling cycle for longer than in dilute conditions. Simultaneously, the impenetrability of SCNPs limits the elongation in the stretched phase of the tumbling motion. Combined, these two effects could explain the decrease in average size as a function of density at high shear rates, which is not encountered in solutions of linear polymers.
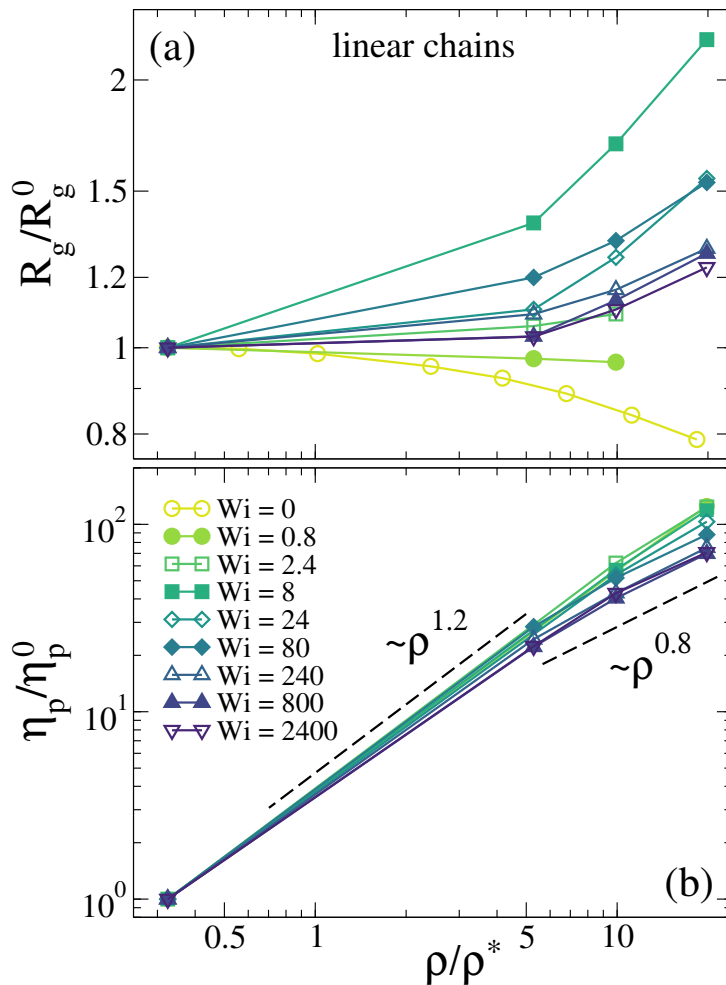
Figure 4.23: Radius of gyration (a) and polymer contribution to the viscosity (b) vs. concentration in solutions of linear chains (data are sampled from Ref. [34]). Each data set corresponds to a fixed value of the Weissenberg number Wi (see legends), and is normalized by the value for that Wi at the lowest concentration $\rho/\rho^\star \approx 0.3$. It must be noted that our definition of the overlap concentration is $\pi/6$ times the one used in Ref. [34], so we have rescaled the data there by such a factor.

4.4   Conclusion

In this chapter, we have investigated the response of single-chain nanoparticles to homogeneous shear flow in high dilution and semi-dilute systems. We employed Molecular Dynamics for the polymers coupled to a solvent modeled via Multi-particle Collision Dynamics in order to include hydrodynamic interactions. By focusing first on the effect of different polymer topologies (sparse to globular) resulting from the stochastic character of the cross-linking process, we showed that SCNPs exhibit universal scaling laws independent of their specific architecture for several of their static and dynamic observables. The set of exponents we found for the Wi-scaling of the gyration tensor, the orientational resistance, the rotational frequency and the viscosity is clearly distinct from other

polymer architectures such as linear chains, stars or ring polymers. We thus conclude that SCNPs constitute a separate class of polymeric nanoparticles, that is defined not by the specific connectivity, but by the average sparse network-like character. Despite their universal response to shear, the underlying dynamics of different SCNP topologies in shear flows present a complex interplay of both tumbling and tank-treading motions. While signatures of both behaviors are visible in the characteristic correlation functions C_{xy} and C_{angle} at intermediate Weissenberg numbers, the response of SCNPs of different equilibrium asphericities diverge at high shear rates: tumbling dominates the dynamics of sparse SCNPs and tank-treading is prevalent in globular topologies.

In semi-dilute and crowded solutions, SCNPs exhibit a novel density dependent response to shear at intermediate to high Weissenberg numbers. Contrary to simpler polymer architectures, like linear chains or stars, for which the Wi-scaling of various static observables depend at most marginally on the concentration, we find two distinct limiting scaling exponents in SCNPs solutions with a cross-over around the overlap concentration. Furthermore, increasing the density of SCNPs at a fixed shear rate leads to a complex re-entrance phenomenon for the molecular size, with mild swelling at low to intermediate shear rates and shrinking at high shear rates, the latter of which is never observed in linear chains. We believe this behavior originates from the intrinsic impenetrable character of the SCNPs, which hinders formation of entanglements and leads to the transition to crumpled globular conformations in equilibrium. While linear chains achieve a better packing through alignment and elongation in the flow direction, SCNPs need to adopt more collapsed conformations to accommodate neighboring molecules. A comparison between polydisperse and monodisperse solutions of three different SCNP topologies (globular, intermediate, sparse) shows that the complex response of SCNPs to shear does not originate from a complex interplay of various time-scales, but is intrinsic to the randomly cross-linked architecture of these nanoparticles. While the specific scaling exponents found in monodisperse solutions below and above the overlap concentration differ slightly, they exhibit the same qualitative behavior in all static observables as the polydisperse mixtures.

We believe that our results shed light on the role of topology in the response of polymeric nanoparticles to shear flows, which are important in many of their potential applications, such as drug delivery or bio-imaging. Furthermore, in light of the structural similarities between SCNPs and intrinsically disordered proteins (IDPs) [49, 64], we hope that our findings can help to understand the effects strong shear flows have on IDPs. We expect that SCNPs serve as an even better non-specific model for IDPs in such scenarios,

as shearing forces are able to break some of the ordered domains of IDPs stabilized by weak physical interactions [65], such as hydrogen bonds, electrostatic attraction and self-assembly of hydrophobic patches, while the stronger chemical bonds, such as disulfide bonds, reminiscent of the SCNPs' cross-links prevail.

References

[1] D. E. Smith, H. P. Babcock, and S. Chu, "Single-polymer dynamics in steady shear flow," *Science*, vol. 283, no. 5408, pp. 1724–1727, 1999.

[2] J. S. Hur, E. S. G. Shaqfeh, H. P. Babcock, D. E. Smith, and S. Chu, "Dynamics of dilute and semidilute dna solutions in the start-up of shear flow," *Journal of Rheology*, vol. 45, no. 2, pp. 421–450, 2001.

[3] R. E. Teixeira, H. P. Babcock, E. S. G. Shaqfeh, and S. Chu, "Shear thinning and tumbling dynamics of single polymers in the flow-gradient plane," *Macromolecules*, vol. 38, no. 2, pp. 581–592, 2005.

[4] S. Gerashchenko and V. Steinberg, "Statistics of tumbling of a single polymer molecule in shear flow," *Phys. Rev. Lett.*, vol. 96, p. 038304, Jan 2006.

[5] J. M. Skotheim and T. W. Secomb, "Red blood cells and other nonspherical capsules in shear flow: Oscillatory dynamics and the tank-treading-to-tumbling transition," *Phys. Rev. Lett.*, vol. 98, p. 078301, Feb 2007.

[6] M. Abkarian, M. Faivre, and A. Viallat, "Swinging of red blood cells under shear flow," *Phys. Rev. Lett.*, vol. 98, p. 188302, Apr 2007.

[7] W. Dodson and P. Dimitrakopoulos, "Tank-treading of erythrocytes in strong shear flows via a nonstiff cytoskeleton-based continuum computational modeling," *Biophysical Journal*, vol. 99, no. 9, pp. 2906 – 2916, 2010.

[8] A. Z. K. Yazdani and P. Bagchi, "Phase diagram and breathing dynamics of a single red blood cell and a biconcave capsule in dilute shear flow," *Phys. Rev. E*, vol. 84, p. 026314, Aug 2011.

[9] R. G. Larson, *The structure and rheology of complex fluids*, vol. 150. Oxford university press New York, 1999.

[10] J. A. Izaguirre, D. P. Catarello, J. M. Wozniak, and R. D. Skeel, "Langevin stabilization of molecular dynamics," *J Chem. Phys.*, vol. 114, no. 5, pp. 2090–2098, 2001.

[11] A. Malevanets and R. Kapral, "Mesoscopic model for solvent dynamics," *J. Chem. Phys.*, vol. 110, no. 17, pp. 8605–8613, 1999.

[12] A. Malevanets and R. Kapral, "Solute molecular dynamics in a mesoscale solvent," *J. Chem. Phys.*, vol. 112, no. 16, pp. 7260–7269, 2000.

[13] T. Ihle and D. Kroll, "Stochastic rotation dynamics: a galilean-invariant mesoscopic model for fluid flow," *Phys. Rev. E*, vol. 63, no. 2, p. 020201, 2001.

[14] T. Ihle and D. M. Kroll, "Stochastic rotation dynamics. i. formalism, galilean invariance, and green-kubo relations," *Phys. Rev. E*, vol. 67, p. 066705, Jun 2003.

[15] A. Lees and S. Edwards, "The computer study of transport processes under extreme conditions," *J. Phys. C*, vol. 5, no. 15, p. 1921, 1972.

[16] C. Aust, M. Kröger, and S. Hess, "Structure and dynamics of dilute polymer solutions under shear flow via nonequilibrium molecular dynamics," *Macromolecules*, vol. 32, no. 17, pp. 5660–5672, 1999.

[17] M. Liebetreu, M. Ripoll, and C. N. Likos, "Trefoil knot hydrodynamic delocalization on sheared ring polymers," *ACS Macro Letters*, vol. 7, no. 4, pp. 447–452, 2018.

[18] C. M. Schroeder, R. E. Teixeira, E. S. G. Shaqfeh, and S. Chu, "Dynamics of dna in the flow-gradient plane of steady shear flow: Observations and simulations," *Macromolecules*, vol. 38, no. 5, pp. 1967–1978, 2005.

[19] M. Ripoll, R. G. Winkler, and G. Gompper, "Star polymers in shear flow," *Phys. Rev. Lett.*, vol. 96, p. 188302, May 2006.

[20] W. Chen, K. Zhang, L. Liu, J. Chen, Y. Li, and L. An, "Conformation and dynamics of individual star in shear flow and comparison with linear and ring polymers," *Macromolecules*, vol. 50, no. 3, pp. 1236–1244, 2017.

[21] W. Chen, Y. Li, H. Zhao, L. Liu, J. Chen, and L. An, "Conformations and dynamics of single flexible ring polymers in simple shear flow," *Polymer*, vol. 64, pp. 93 – 99, 2015. New application of Organic Reactions for Controlling Polymer Architectures (ORCP).

[22] A. Nikoubashman and C. N. Likos, "Branched polymers under shear," *Macromolecules*, vol. 43, no. 3, pp. 1610–1620, 2010.

[23] D. Jaramillo-Cano, M. Formanek, C. N. Likos, and M. Camargo, "Star block-copolymers in shear flow," *The Journal of Physical Chemistry B*, vol. 122, no. 14, pp. 4149–4158, 2018. PMID: 29547293.

[24] W. Chen, J. Chen, L. Liu, X. Xu, and L. An, "Effects of chain stiffness on conformational and dynamical properties of individual ring polymers in shear flow," *Macromolecules*, vol. 46, no. 18, pp. 7542–7549, 2013.

[25] W. Chen, J. Chen, and L. An, "Tumbling and tank-treading dynamics of individual ring polymers in shear flow," *Soft Matter*, vol. 9, pp. 4312–4318, 2013.

[26] R. G. Winkler, "Conformational and rheological properties of semiflexible polymers in shear flow," *The Journal of Chemical Physics*, vol. 133, no. 16, p. 164905, 2010.

[27] R. G. Winkler, D. A. Fedosov, and G. Gompper, "Dynamical and rheological properties of soft colloid suspensions," *Current Opinion in Colloid & Interface Science*, vol. 19, no. 6, pp. 594 – 610, 2014.

[28] J. Bossart and H. C. Oettinger, "Orientation of polymer coils in dilute solutions undergoing shear flow: Birefringence and light scattering," *Macromolecules*, vol. 28, no. 17, pp. 5852–5860, 1995.

[29] M. Doi and S. F. Edwards, *The theory of polymer dynamics.* Oxford University Press: Oxford, U.K., 1986.

[30] A. Link and J. Springer, "Light scattering from dilute polymer solutions in shear flow," *Macromolecules*, vol. 26, no. 3, pp. 464–471, 1993.

[31] R. Bird, C. Curtiss, R. Armstrong, and O. Hassager, *Dynamics of Polymer Liquids Vol. 2 Kinetic Theory.* Wiley, 1987.

[32] J. S. Myung, R. G. Winkler, and G. Gompper, "Self-organization in suspensions of end-functionalized semiflexible polymers under shear flow," *The Journal of Chemical Physics*, vol. 143, no. 24, p. 243117, 2015.

[33] P. S. Doyle, E. S. G. Shaqfeh, and A. P. Gast, "Dynamic simulation of freely draining flexible polymers in steady linear flows," *Journal of Fluid Mechanics*, vol. 334, p. 251–291, 1997.

[34] C. Huang, A. Chatterji, G. Sutmann, G. Gompper, and R. Winkler, "Cell-level canonical sampling by velocity scaling for multiparticle collision dynamics simulations," *J. Comp. Phys.*, vol. 229, no. 1, pp. 168 – 177, 2010.

[35] S. H. Jeong, J. M. Kim, and C. Baig, "Rheological influence of short-chain branching for polymeric materials under shear with variable branch density and branching architecture," *Macromolecules*, vol. 50, no. 11, pp. 4491–4500, 2017.

[36] D. Jaramillo-Cano, C. N. Likos, and M. Camargo, "Rotation dynamics of star block copolymers under shear flow," *Polymers*, vol. 10, no. 8, 2018.

[37] J. Sablić, M. Praprotnik, and R. Delgado-Buscalioni, "Deciphering the dynamics of star molecules in shear flow," *Soft Matter*, vol. 13, pp. 4971–4987, 2017.

[38] W. Chen, H. Zhao, L. Liu, J. Chen, Y. Li, and L. An, "Effects of excluded volume and hydrodynamic interaction on the deformation, orientation and motion of ring polymers in shear flow," *Soft Matter*, vol. 11, pp. 5265–5273, 2015.

[39] A. Puliafito and K. Turitsyn, "Numerical study of polymer tumbling in linear shear flows," *Physica D: Nonlinear Phenomena*, vol. 211, no. 1, pp. 9 – 22, 2005.

[40] R. G. Winkler, "Semiflexible polymers in shear flow," *Phys. Rev. Lett.*, vol. 97, p. 128301, Sep 2006.

[41] J. S. Hur, E. S. G. Shaqfeh, and R. G. Larson, "Brownian dynamics simulations of single dna molecules in shear flow," *Journal of Rheology*, vol. 44, no. 4, pp. 713–742, 2000.

[42] S. I. Dalal, A. Albaugh, N. Hoda, and R. G. Larson, "Tumbling and deformation of isolated polymer chains in shearing flow," *Macromolecules*, vol. 45, no. 23, pp. 9493–9499, 2012.

[43] P. S. Lang, B. Obermayer, and E. Frey, "Dynamics of a semiflexible polymer or polymer ring in shear flow," *Phys. Rev. E*, vol. 89, p. 022606, Feb 2014.

[44] C.-C. Huang, G. Sutmann, G. Gompper, and R. G. Winkler, "Tumbling of polymers in semidilute solution under shear flow," *EPL (Europhysics Letters)*, vol. 93, no. 5, p. 54004, 2011.

[45] J. Sablić, R. Delgado-Buscalioni, and M. Praprotnik, "Application of the eckart frame to soft matter: rotation of star polymers under shear flow," *Soft Matter*, vol. 13, pp. 6988–7000, 2017.

[46] C. Aust, S. Hess, and M. Kröger, "Rotation and deformation of a finitely extendable flexible polymer molecule in a steady shear flow," *Macromolecules*, vol. 35, no. 22, pp. 8621–8630, 2002.

[47] S. P. Singh, D. A. Fedosov, A. Chatterji, R. G. Winkler, and G. Gompper, "Conformational and dynamical properties of ultra-soft colloids in semi-dilute solutions under shear flow," *Journal of Physics: Condensed Matter*, vol. 24, no. 46, p. 464103, 2012.

[48] C. Eckart, "Some studies concerning rotating axes and polyatomic molecules," *Phys. Rev.*, vol. 47, pp. 552–558, Apr 1935.

[49] A. J. Moreno, F. Lo Verso, A. Arbe, J. A. Pomposo, and J. Colmenero, "Concentrated solutions of single-chain nanoparticles: A simple model for intrinsically disordered proteins under crowding conditions," *J. Phys. Chem. Lett.*, vol. 7, no. 5, pp. 838–844, 2016.

[50] M. Gonzalez-Burgos, A. Arbe, A. J. Moreno, J. A. Pomposo, A. Radulescu, and J. Colmenero, "Crowding the environment of single-chain nanoparticles: A combined study by sans and simulations," *Macromolecules*, vol. 51, no. 4, pp. 1573–1585, 2018.

[51] M. Rubinstein and R. H. Colby, *Polymer Physics*, vol. 23. Oxford University Press: Oxford, U.K., 2003.

[52] R. Everaers, S. K. Sukumaran, G. S. Grest, C. Svaneborg, A. Sivasubramanian, and K. Kremer, "Rheology and microscopic topology of entangled polymeric liquids," *Science*, vol. 303, no. 5659, pp. 823–826, 2004.

[53] R. S. Hoy, K. Foteinopoulou, and M. Kröger, "Topological analysis of polymeric melts: Chain-length effects and fast-converging estimators for entanglement length," *Phys. Rev. E*, vol. 80, p. 031803, Sep 2009.

[54] A. Arbe, J. Rubio-Cervilla, A. Alegría, A. J. Moreno, J. A. Pomposo, B. Robles-Hernández, P. Malo de Molina, P. Fouquet, F. Juranyi, and J. Colmenero, "Mesoscale dynamics in melts of single-chain polymeric nanoparticles," *Macromolecules*, vol. 52, no. 18, pp. 6935–6942, 2019.

[55] C.-C. Huang, R. G. Winkler, G. Sutmann, and G. Gompper, "Semidilute polymer solutions at equilibrium and under shear flow," *Macromolecules*, vol. 43, no. 23, pp. 10107–10116, 2010.

[56] C.-C. Huang, G. Gompper, and R. G. Winkler, "Non-equilibrium relaxation and tumbling times of polymers in semidilute solution," *J. Phys.: Condens. Matter*, vol. 24, no. 28, p. 284131, 2012.

[57] H. Pasch and B. Trathnigg, *HPLC of Polymers.* Springer, Berlin, 1999.

[58] H. C. Lee, H. Lee, W. Lee, T. Chang, and J. Roovers, "Fractionation of cyclic polystyrene from linear precursor by hplc at the chromatographic critical condition," *Macromolecules*, vol. 33, no. 22, pp. 8119–8121, 2000.

[59] W. Lee, H. Lee, H. C. Lee, D. Cho, T. Chang, A. A. Gorbunov, and J. Roovers, "Retention behavior of linear and ring polystyrene at the chromatographic critical condition," *Macromolecules*, vol. 35, no. 2, pp. 529–538, 2002.

[60] Y. Tezuka, K. Mori, and H. Oike, "Efficient synthesis of cyclic poly(oxyethylene) by electrostatic self-assembly and covalent fixation with telechelic precursor having cyclic ammonium salt groups," *Macromolecules*, vol. 35, no. 14, pp. 5707–5711, 2002.

[61] J. R. Montenegro-Burke, J. M. Bennett, J. A. McLean, and D. M. Hercules, "Novel behavior of the chromatographic separation of linear and cyclic polymers," *Analytical and Bioanalytical Chemistry*, vol. 408, pp. 677–681, Jan 2016.

[62] F. Barroso-Bujans and A. Alegria, "Kinetic differences in the intercalation of linear and cyclic penta(ethylene oxide)s into graphite oxide leading to separation by topology," *Phys. Chem. Chem. Phys.*, 2017.

[63] L. B. Weiss, A. Nikoubashman, and C. N. Likos, "Topology-sensitive microfluidic filter for polymers of varying stiffness," *ACS Macro Letters*, vol. 6, no. 12, pp. 1426–1431, 2017.

[64] A. J. Moreno, P. Bacova, F. L. Verso, A. Arbe, J. Colmenero, and J. A. Pomposo, "Effect of chain stiffness on the structure of single-chain polymer nanoparticles," *J. Phys.: Condens. Matter*, vol. 30, no. 3, p. 034001, 2018.

[65] I. B. Bekard, P. Asimakis, J. Bertolini, and D. E. Dunstan, "The effects of shear flow on protein structure and function," *Biopolymers*, vol. 95, no. 11, pp. 733–745, 2011.

Chapter 5

Gel Formation in Reversibly Cross-linking Polymers

5.1   Introduction

Since its beginnings at the start of the 21st century, the synthesis of single-chain nanoparticles has been dominated by polymer chemistries involving irreversibly cross-linking functional groups. In the past years, however, the possibility of exploiting reversible interactions to produce stimuli-responsive SCNPs is gaining increased interest [1, 2, 3, 4, 5, 6, 7, 8]. Separate classes of reversible interactions with distinct advantages have emerged in the field of single-chain technology: non-covalent and so-called dynamic covalent bonds. Non-covalent bonds are characterized by their relatively low energy (typically a few k_BT), which is modulated smoothly by external variables such as temperature, pH and solvent. Prominent examples of non-covalent interactions used in SCNPs are hydrogen bonds [9, 10], helical [11, 12] or $\pi - \pi$ stacking [13], host-guest interactions [14, 15], ionic attraction [16] and metal complex formation [17, 18]. In contrast to non-covalent bonds, reversible or dynamic covalent bonds are very robust and their formation, breaking or exchange can be induced rapidly by very specific external stimuli. These can be pH, photons, redox potentials or a catalyst. The classical example of a dynamic covalent bond is the disulfide bridge, which plays a prominent role in the stabilization of the native folded state of proteins. It served as inspiration for including disulfide bonds [19], but also hydrazone [20], enamine [21], coumarine [22] and anthrazene [23] bonds in the SCNP chemistry toolbox.

The advantage of dynamic covalent bonds is that the need for an external stimulus to catalyze their formation and breaking opens up the possibility of kinetically trapping the system. Furthermore, reversibility means that synthesis is never 'complete' and individual SCNPs of this kind can form intermolecular bonds in addition to their intramolecular bonds if their concentration is increased above the very high dilution limit. Such intermolecular bonds could potentially lead to aggregation, phase separation but also the formation of a physical gel. The interplay between intra- and intermolecular bond formation has been exploited recently by Fulton *et al.* in thermoresponsive polymers to produce a system that reversibly transitions between a SCNP solution and a hydrogel [24]. The thermoresponsive nature of the oligoethyleneglycol methyl ether branches causes the polymers to aggregate upon a rise in temperature, while a mildly acidic pH allows the acylhydrazone bonds to undergo component exchange processes. Combination of these two orthogonal triggers leads to the reversible reorganization of intramolecularly folded SCNPs into a robustly cross-linked hydrogel. The response of this material to multiple external stimuli could be exploited in situations where the behavior of the material should

depend on the specific makeup of the environment, for example the specific release of drugs in target tissues.

While the advances in synthesis of such reversible gels made from dynamic covalent SCNPs are promising, investigations of the structure of such materials is lacking until now. Moreover, the theoretical description of physical gels in general (as opposed to permanently cross-linked chemical gels), has come into focus in the soft matter community in relatively recent years. This is due in part to the difficulty of precisely defining the meaning of 'gel', as currently both systems exhibiting dynamical arrest and network formation in equilibrium are considered gels. A common working definition of a gel is a low density disordered state with solid-like properties such as a yield stress. It combines properties of a liquid through its disordered structure and a solid in that it does not flow. What distinguishes them from glasses is not only their typical low volume fraction but also their retention of quasi-ergodicity on all but the largest length scales dictated by the infinite percolating network [25, 26, 27, 28, 29]. A second obstacle for the establishment of a unifying theoretical framework of gel formation is the lack of an ideal model system that incorporates the minimal, necessary ingredients to reproduce the universal features of a gelling system.

In Hill's formalism of liquid condensation in terms of physical clusters, phase separation induced by strong attractive forces can be avoided by either complementing the attraction by a long-range repulsion [30, 31] or by modifying the attraction by limiting the valence of the interacting molecules [32]. The former can be induced by excessive surface charges on colloids [33], while the latter can be achieved by decorating colloidal particles with a small number of well defined attractive patches [34, 35] or the engineering of specific DNA sequences designed to form star-shaped architectures with sticky ends [36, 37]. The advantage of such limited-valence particles lies in the possibility of theoretically calculating their free energy within the formalism of Wertheim theory [38, 39], which allows one to determine the phase diagram of the system [40]. Furthermore, the increased experimental control over such patchy particles achieved in the past decade has paved the way for their use as highly tunable building blocks for the design of self-assembled materials [41, 42].

We believe that single-chain nanoparticles with reversible bonds will display characteristics of both microphase separating colloids and patchy particles due to the competition between intra- and intermolecular bonds. At very high dilution, intramolecular bonds should be favored by the separation of chains in good solvent conditions. Upon increasing

the volume fraction, some of these intramolecular bonds will be exchanged for connections with other chains for entropic reasons, possibly forming a system-spanning network for the right combination of system parameters. We expect phase separation of the system to be avoided through the combination of excluded volume interactions and the inherently limited 'valence' of the polymers because of the locally small number of (monovalent) monomers capable of forming bonds.

In this chapter, we aim to provide a preliminary investigation into the gel formation of such reversible SCNPs by means of Langevin dynamics simulations. We will show that the competition between intra- and intermolecular bonds is governed by a delicate balance of various entropic contributions and leads to a density dependent effective valence. System-spanning networks form at relatively low monomer densities, whose cluster size at the percolation threshold is well described by Flory-Stockmayer theory. The formation of intermolecular bonds furthermore induces a non-monotonic dependence of the polymers' size on the density in the limit of very high bond lifetimes. At the same time, the polymers in the percolating cluster adopt an intramolecular structure characteristic for self-avoiding chains, which constitutes a strong contrast to the collapse behavior (to crumpled globules) of irreversible SCNPs in semi-dilute solutions. Finally, we study the dynamics of the system, which displays the typical caging phenomena of gelling materials in the mean-squared displacement. Simultaneously, an interesting behavior emerges in the reorganization dynamics of the percolating cluster, where the time it takes for a free chain to reattach to the cluster is solely governed by the bond strength.

5.2   Simulation Details

We perform Langevin dynamics simulations (as introduced in Section 2.6 of Chapter 2) at a fixed temperature of $T = \epsilon/k_B T = 1$, with a time-step of $\Delta t = 0.01\sigma(m/\epsilon)^{1/2}$ and a friction coefficient of $\gamma = 0.05$.

The reversibly cross-linking polymers are modeled according to the coarse-grained bead-spring model introduced in Chapter 2.2. As such, they represent uncrossable flexible chains of Kuhn length σ with excluded volume interactions in good solvent conditions. They consist of $N = 200$ monomers, consecutively linked together by irreversible backbone bonds modeled via the FENE potential (Equation 2.2). A fraction $f = N_r/N$ of these monomers is randomly chosen to be of the reactive type, which can form monofunctional, reversible bonds with other reactive monomers. A bond is formed whenever two

monomers approach each other in space and are separated by less than the capture radius $r_c = 1.3$. This bond formation is identical to the cross-linking process in the case of irreversible single-chain nanoparticles. However, once a bond is formed, the two participating monomers do not interact via a FENE potential, but instead via a Morse potential

$$U^{\text{rev}}(r) = K \left[2e^{(r_0-r)} - e^{2(r_0-r)} \right] , \tag{5.1}$$

with an adjustable parameter K. Bonds can be broken again, if, at any given timestep, the participating monomers separate by more than r_c, upon which their interaction via the Morse potential terminates. The parameter K governs the bond strength through modulating the energy barrier that has to be overcome in order to break the bond, which is given by the energy difference $U(r_c) - U(r_0)$. As such, bond formation is independent of K, while bond breakage depends on K. Thus, varying K not only changes the average bond lifetime, but also the average probability of any reactive monomer being bonded at equilibrium. The remaining free parameter r_0 is chosen such that the minimum of the sum of non-bonded and bonded interactions for both irreversible and reversible bonds are similar (see Figure 2.1 of Chapter 2, which compares the various potentials used to simulate bonds between reactive monomers). Contrary to patchy particle models, in which the monofunctionality of the bonds is encoded in the geometry of the interaction [40, 43, 37, 44], we enforce monofunctionality by keeping a list of bonded pairs. Reactive monomers that are currently already bonded cannot form other bonds until their current one is broken.

Before simulating reversibly cross-linking chains at various densities, we perform exploratory simulations of single chains in the limit of very high dilution $\rho \to 0$ for various values of f (fraction of reactive groups) and K (bond strength). We calculate the radius of gyration R_{g} and the bond probability p_b, which is defined as the ratio between the number of bonds formed and the total number of possible bonds (a distinction between intra- and intermolecular bonds is not made). Our results are summarized in Table 5.1. As expected, the probability of any reactive monomer to be bonded at equilibrium depends strongly on K and mildly on f. Interestingly, a comparison of the radius of gyration of fully cross-linked irreversible SCNPs and the reversible chains of different K shows that SCNPs are still significantly smaller on average than the reversible chains whose bond probability approaches 1.

Since we are interested in exploring the possibility of forming gels from these reversibly cross-linking chains, the bond probability needs to be high enough for a system spanning cluster to form and give the material the ability to propagate stresses throughout the

f	K	r_0	R_{g}	p_B
	24.6	1.380	11.256	0.27
	27.0	1.420	10.942	0.47
	29.6	1.448	10.386	0.7
0.1	31.6	1.464	9.893	0.83
	33.7	1.477	9.349	0.91
	Irreversible		8.015	1
	24.6	1.38	10.977	0.48
	27.0	1.42	10.404	0.68
	29.6	1.448	9.809	0.84
0.2	31.6	1.464	9.363	0.92
	33.7	1.477	8.776	0.96
	Irreversible		7.714	1
	24.6	1.38	10.707	0.60
	27.0	1.42	10.186	0.78
	29.6	1.448	9.690	0.9
0.3	31.6	1.464	9.237	0.95
	33.7	1.477	8.547	0.97
	Irreversible		7.534	1

Table 5.1: Radius of gyration R_{g} and bond probability p_B as a function of bond strength K and fraction of reactive groups f at highly dilute conditions ($\rho \to 0$). The values for irreversibly cross-linked SCNPs are included for comparison.

whole system. We decided to choose the bond strength parameters $K = 29.6$ and 33.7 as well two fractions of reactive monomers, $f = 0.1$ and 0.3, for the subsequent simulations at different densities.

In the following simulations, we keep the total number of chains $N_c = 108$, and thus the total number of monomers $N_m = N \cdot N_c = 21600$, fixed for all systems, while varying the size of the cubic simulation box according to $L = V^{1/3} = \left(\frac{N}{\rho}\right)^{1/3}$. For the remainder of this chapter, we report the density of the system in reduced units $\rho/\rho^\star$, where $\rho^\star$ is the overlap concentration. We define the overlap concentration $\rho^\star = N(2R_{\mathrm{g}})^{-3}$ with respect to the radius of gyration of a chain with a given (f, K) parameter combination in the highly dilute limit $\rho \to 0$ (see Table 5.1). We expect intermolecular cross-links to begin forming significantly around the overlap concentration, when monomers of different chains start

to enter the same space. Irreversible SCNPs at equilibrium undergo a crossover in their scaling behavior around the overlap concentration. Their topological interactions prevent the concatenation of two or more SCNPs, which leads to their collapse to crumpled globules [45, 46], instead of the milder transition of inert linear polymers to Gaussian chains. We explore densities in the range $0 \leq \rho/\rho^\star \leq 4.4$. This corresponds to monomer densities up to $\rho \approx 0.14$, which lies below the entanglement density for linear chains of the same polymerization degree, $\rho_\mathrm{e} \gtrsim 0.42$ (see Chapter 4). Where possible, we initialize the system with equilibrated configurations of the polymers in a cubic lattice. Beyond a certain density, overlapping chains generate strong repulsive forces due to the excluded volume interactions and impede such an approach. We thus initialize the system in the smallest box possible and run a small simulation in which we periodically scale the volume and the monomer positions by a small factor $x \lesssim 1$ until we reach the desired size. For each parameter combination and each density, we run 8 independent simulation runs, each consisting of 1×10^7 equilibration steps and 4×10^7 production steps.

5.3 Results and Discussion

5.3.1 Competition between intra- and intermolecular bonds

Ideally, we would like to evaluate the complete $K - \rho$ phase diagram of these reversibly cross-linking polymers to find the regions in which gel formation is possible. However, performing calculations of a sufficient number of parameter combinations is beyond the scope of this work as a single run on a single CPU requires about 1 month of CPU time.

A different and more elegant approach is to derive a thermodynamic description of the system according to Wertheim theory [38, 39] by using inputs from computer simulations. Wertheim thermodynamic perturbation theory (TPT) was originally developed for associating liquids, but has also been successfully employed to elucidate the phase behavior of gel forming systems of limited valence, qualitatively and sometimes even quantitatively reproducing numerical results [40, 47, 48]. It assumes that the free energy of a system can be decomposed into two parts: one contribution coming from a reference system without bonds, and a contribution stemming from the bonds formed in the system. The former can be estimated via a virial expansion to second order, where the second virial coefficient is calculated from the effective potential between two purely repulsive reference particles. The latter is given directly by the theory, derived from a summation over certain classes
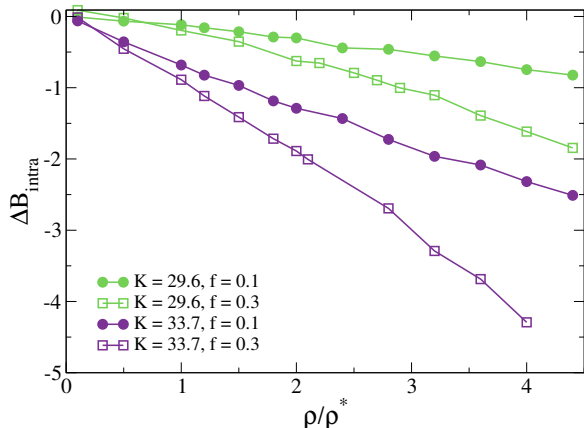
Figure 5.1: Relative change in average number of intramolecular bonds per molecule (with respect to infinite dilution) for different values of energy constant K and reactive monomer fraction f as a function of density.
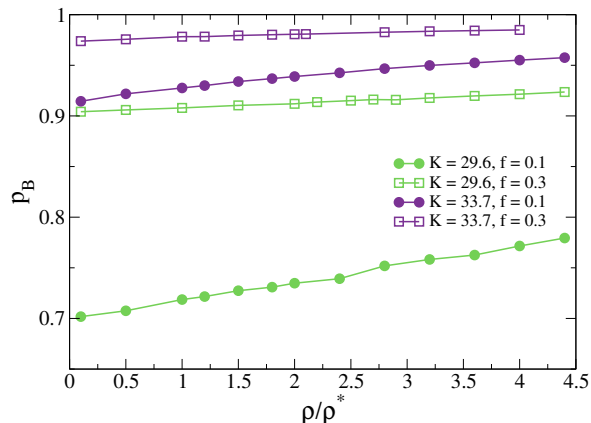
Figure 5.2: Total (intra- and intermolecular) bond probability p_B for different values of energy constant K and reactive monomer fraction f as a function of density.

of relevant graphs in the Mayer expansion, and depends on the effective valence of the system.

A few fundamental assumptions of TPT have to be satisfied in order to be able to describe the system according to its predictions: (i) bonds are strictly monofunctional, (ii) two molecules can not share more than one bond and (iii) molecules cannot form bonds with themselves. While (ii) might be problematic at very high densities, (iii) is inherently violated in a flexible polymeric molecule with many functional groups along its backbone. However, if the number of intramolecular bonds stays approximately constant at different densities for a specific K, we can neglect intramolecular bonds and view the polymers as having an 'effective' valence of $M = [1 - p_b(K, \rho = 0)] N \cdot f$. If this is the case, the polymers might behave similar to patchy particles, but with the distinction that the 'patches' are not located at specific points on their surface, but randomly distributed and fluctuate, due to the inherent softness of the polymer and the possible restructuring of the intramolecular bonds. In this view, the intramolecular bonds solely affect the reference free energy, which can be calculated with the Widom insertion method [49] by only allowing intramolecular bonds to form.

Thus, our first objective is to test whether this assumption of intramolecular bonds being unaffected by interactions with other nanoparticles holds over a certain range of densities. Figure 5.1 displays the relative loss of intramolecular bonds per chain as a function of density. Unfortunately, for all f, K parameter combinations, increasing the density of the system leads to a competition between intra- and intermolecular bonds,

instead of a simple addition of intermolecular bonds on the periphery of a cross-linked particle. The effect is strongest for $K = 33.7$ and $f = 0.3$, the system with the highest bond probability p_B in high dilution. This can be understood in terms of the overall bond probability p_B, which is reported in Figure 5.2. We notice that at $K = 33.7$ and $f = 0.3$, it is saturated already at a low density and stays constant upon crowding the system. Since bonds have a finite lifetime and the monomer density of reactive species is still relatively low at the highest reduced density, there will always be a period of being in a non-bonded state between the breakage of one connection and the formation of a new one, leading to a saturation of p_B below 1. Implementing a bond-swapping algorithm [50, 43], in which bonds can be exchanged between different reactive monomers without an energy penalty, could result in different outcomes and should be considered in future studies of this system. On the other hand, the parameter combination with the smallest bond probability at high dilution, $K = 29.6$ and $f = 0.1$ exhibits the strongest increase in p_B as a function of density. Here, the loss in entropy stemming from the crowding of surrounding molecules can apparently be compensated by the enthalpic gain of forming new additional intermolecular bonds.

The competition between intra- and intermolecular bonds has to be understood in terms of a delicate interplay between various entropic and energetic contributions to the free energy of the system. One could expect that the formation of intramolecular bonds is favorable over the formation of connections with other molecules, as the latter reduces the translational entropy of both molecules without a compensating energetic gain, since the bonds are energetically equivalent. On the other hand, depending on the contour length separating the monomers whose intramolecular bond is exchanged for an intermolecular bond, the breakage of the former could potentially increase the structural entropy of the molecule losing the intramolecular link. Figure 5.3 presents an example of two possible bond recombination events. In scenario (a), two intramolecular bonds between monomers separated by short contour distances are exchanged for an intermolecular bond (and a different intramolecular bond to keep the number of free reactive groups constant). The structural entropy is thus only mildly affected by the breakage of the intramolecular bonds, while the translational entropy is decreased significantly, as the two molecules now have to diffuse together. In scenario (b), the two separate molecules each contain a long-range loop formed by functional groups close to their ends. The opening of this loop via the exchange for an intramolecular bond increases the structural entropy of both molecules, as one of their ends (the one not participating in the newly formed intermolecular bond) becomes floppier and acquires increased freedom to explore different conformations. Apart from the entropic contributions of increasing or decreasing structural and translational

degrees of freedom, one has to consider the purely combinatorial increase in entropy due
to the possibility of forming intermolecular bonds [51]. A quantitative elucidation of this
effect in our system might be obtained via umbrella sampling [52] of two chains at varying
distances.

In conclusion, the delicate interplay between various entropic effects together with the
energetic equivalence of intra- and interchain bonds lead to a competition of the two and
a strong decrease in intrachain bonds with increasing density. This renders a theoretical
treatment of this system according to Wertheim theory impossible without significant
adaptations and we are not able to establish its complete phase diagram.
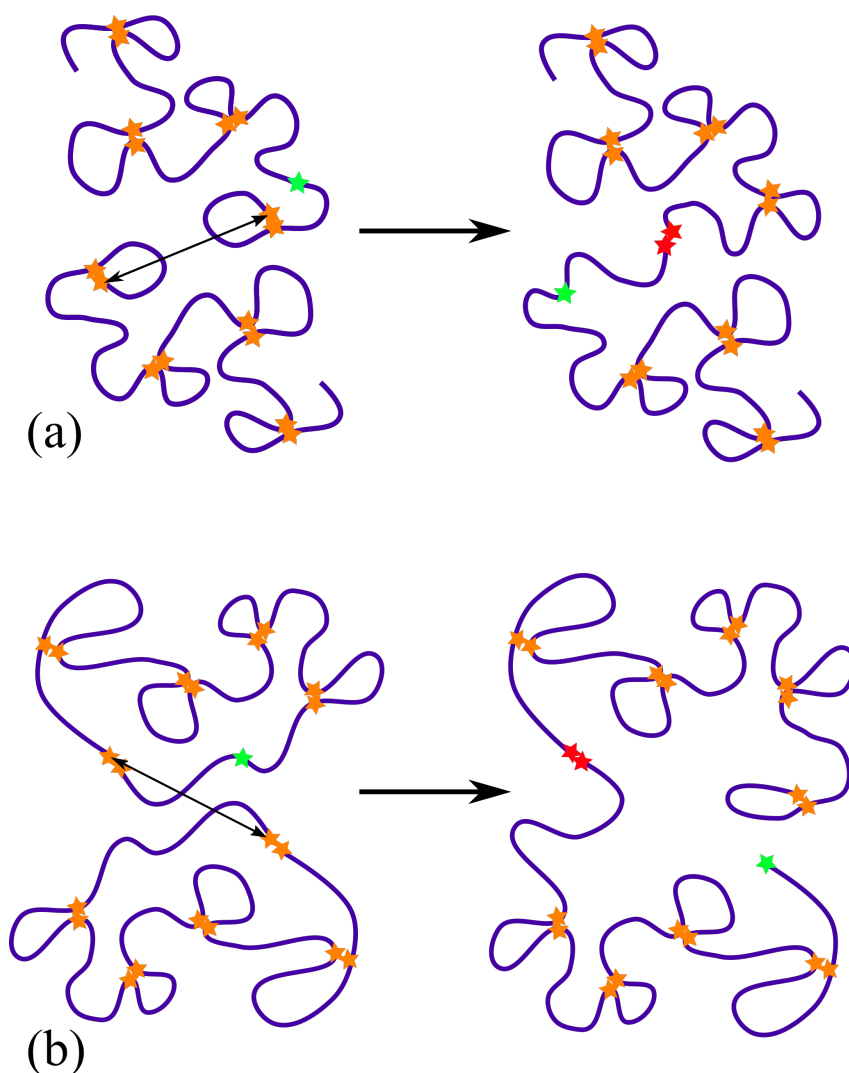

Figure 5.3: Schematic examples of two possible recombinations between intramolecular (yellow stars) and
intermolecular (red stars) bonds. The number of free reactive monomers (green stars) remains unchanged
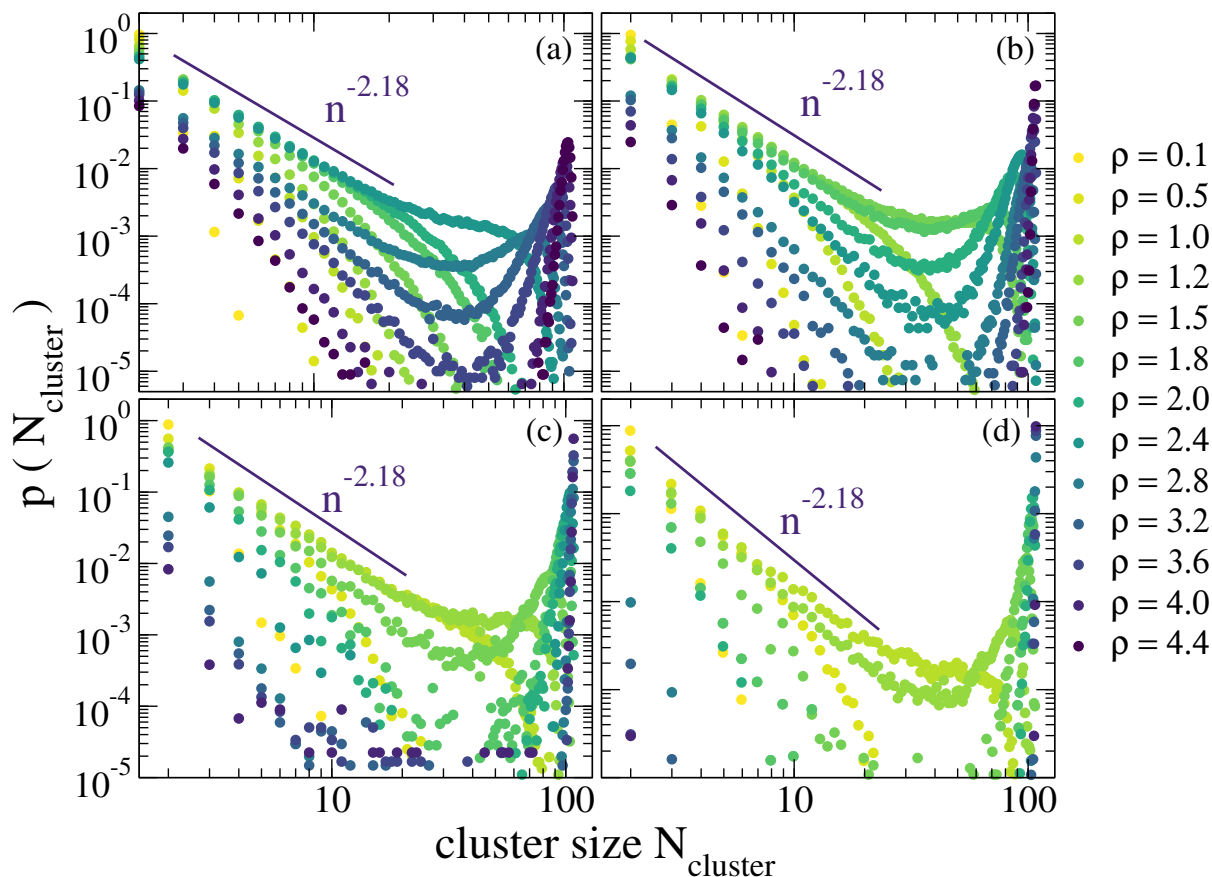in both events.

Figure 5.4: Cluster size distribution for $K = 29.6$ (a, b) and $K = 33.7$ (b, c) as well as $f = 0.1$ (a, c) and $f = 0.3$ (b, d) for various densities. Solid lines are the power-laws $p(N_{\text{cluster}}) \approx N_{\text{cluster}}^{-2.18}$.

5.3.2 Intermolecular Bonding and Percolation

A necessary, albeit not sufficient, prerequisite for gelation, is the emergence of a fully connected network, spanning the whole system in all three directions. In chemical gels, where bonds are irreversible, the onset of this percolation coincides with the system acquiring a finite shear modulus and an infinite zero shear viscosity – the gel stops flowing. In physical gels, where bonds are transient, clusters can break and reform over time, which strongly affects the mechanical and dynamical properties of the system. The transient appearance of a system spanning cluster does therefore not guarantee the propagation of external stresses throughout the whole system for all time scales, as would be expected of a gel.

Figure 5.4 displays the distribution of cluster sizes for the whole range of densities for all four parameter combinations. Here, two chains are said to belong to the same cluster if they share at least one intermolecular bond between them. Note that the maximum cluster size $N_{\text{cluster}}^{\max}$ is 108, as the number of polymers is constant in our simulations.

Irreversible gelation processes are well described by the Flory-Stockmayer mean-field theory of percolation, if two conditions are met: the bonds are independent from each other and loops are not present in the system [53, 54, 55]. Under these assumptions the percolation threshold can be calculated in terms of a critical bond probability p_b^c, which depends on temperature or attraction strength and volume fraction [53, 56]. Close to this critical point, the cluster size distribution follows a power law $p(N_{\mathrm{cluster}}) \sim N_{\mathrm{cluster}}^{-\tau}$ with exponent $\tau = 5/2$. In three dimensions, numerical calculations on different lattices yield an exponent of about $\tau \approx 2.18$ [57, 58, 59]. Both assumptions made in the Flory-Stockmayer theory are violated in our system. Indeed, we observe that close to the formation of a shoulder in the cluster size distribution, it is well described by a scaling law with the same exponent $\tau \approx 2.18$ as found in irreversible lattice models (see solid lines in Figure 5.4). This is found consistently for all parameter combinations.
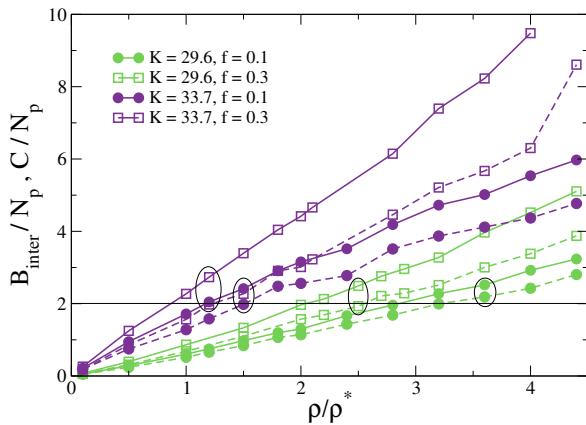

Figure 5.5: Average number of intermolecular bonds (B_{inter}, solid lines) and connectivity (C, dashed lines) per molecule for different values of energy constant K and reactive monomer fraction f as a function of density.
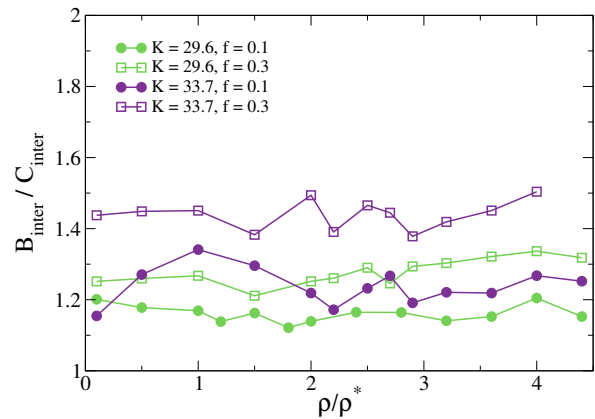
Figure 5.6: Average number of intermolecular bonds B_{inter} per connection with a different molecule for different values of energy constant K and reactive monomer fraction f as a function of density.

Since the 'effective valence' of these reversibly cross-linking polymers is dependent on density, reactive monomer fraction and bond strength, we are interested in how many intermolecular bonds a chain forms on average as the system starts to percolate. One has to keep in mind, however, that multiple bonds are possible between two specific polymers, and every additional bond shared between two chains does not add to the overall connectivity of the network. In Figure 5.5 we thus display both the average number of intermolecular bonds per chain as well as the average connectivity (i.e. to how many other chains is a chain connected, irrespective of the number of bonds mediating the connection). The values at which a pronounced peak at a high cluster size first appears in $P(N_{cluster})$ (see Figure 5.4) are marked by ellipses. We find that the average
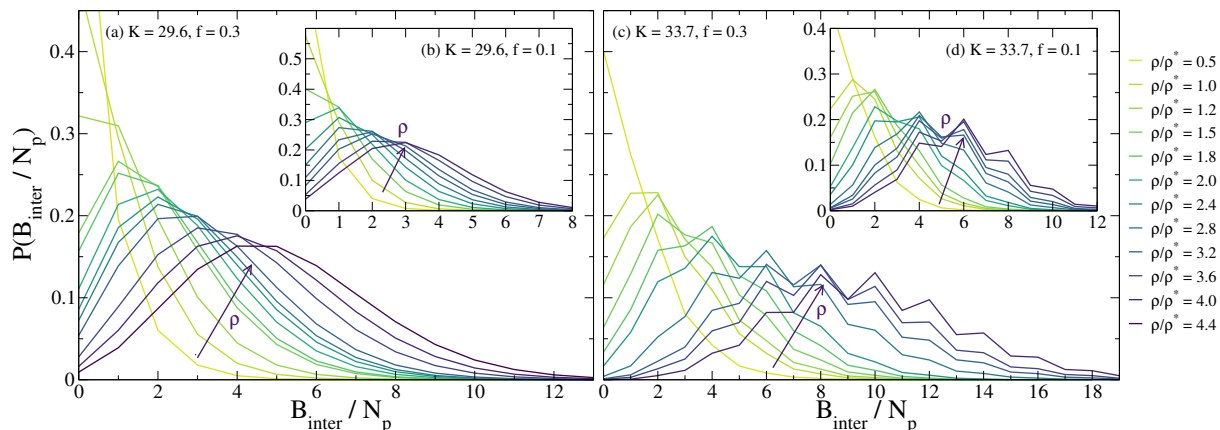
Figure 5.7: Distribution of intermolecular bonds per chain for $K = 29.6$ (a, b) and $K = 33.7$ (b, c) for various densities. The main panels depict the case of $f = 0.3$ (a, c), while the insets represent the case $f = 0.1$ (b, d).

connectivity is approximately two at the onset of the formation of an infinite network. In such a network, some chains need to act as branch points in the network with at least three connections, while chains with two connections will form long bridges between those. Thus, at an average connectivity of two, many chains are still left completely unbonded or forming small aggregates of two or three chains.

Looking at Figure 5.5 one might conclude from the increasing difference between the number of intermolecular bonds B_{inter} and the connectivity C at high densities, that at some point bonds are preferentially formed between chains which are already linked together. This intuitively makes sense, especially for a high fraction of reactive monomers, where reactive monomers on one chain are statistically close in space, which would facilitate the formation of further bonds once one connection between two polymers is established. To test this assumption, we calculate the ratio B_{inter}/C, i.e. how many bonds are formed on average per connection between chain i and j (Figure 5.6). Surprisingly, this value stays approximately constant (within the statistical error) across the whole range of densities for any of the (K, f) parameter combinations. On the other hand, a higher fraction of reactive monomers does lead to more intermolecular bonds per connection, as expected.

To gain a deeper understanding of the formation of intermolecular bonds, we next investigate the distribution of intermolecular bonds at specific densities. Figure 5.7 displays the histograms for $K = 29.6$ and $K = 33.7$, the main panels presenting the case $f = 0.3$ and the insets depicting the case $f = 0.1$, respectively. The distributions reveal a difference in the energy landscape of the system between the two bond strengths. Whereas for $K = 29.6$ the distributions are smooth with a clear maximum, the data for $K = 33.7$

exhibit a characteristic zig-zag pattern, marking even values of B_{inter} as favorable with respect to their closest uneven values. This can be understood in terms of the overall bond probability, which is close to 1 for $K = 33.7$. As the possible bonds within the system are close to saturation, forming an uneven number of intermolecular bonds means that at least one reactive monomer of that chain remains unbonded. The energetic penalty associated with this combinatorial property is high enough in this system to produce such a strong prevalence of even numbers of intermolecular bonds per chain.

5.3.3   Structural Properties

In the previous section, we have shown that the intramolecular bonds are not unaffected by the presence of other molecules, but rather that intra- and intermolecular bonds compete with each other, the outcome of which depends on a delicate interplay of various entropic contributions. We expect this exchange of intra- for intermolecular bonds to be accompanied by structural changes in the polymers. The partial unfolding induced by the opening of intramolecular loops might to some degree counteract the collapse of the polymers due to the steric repulsion with others above the overlap concentration.
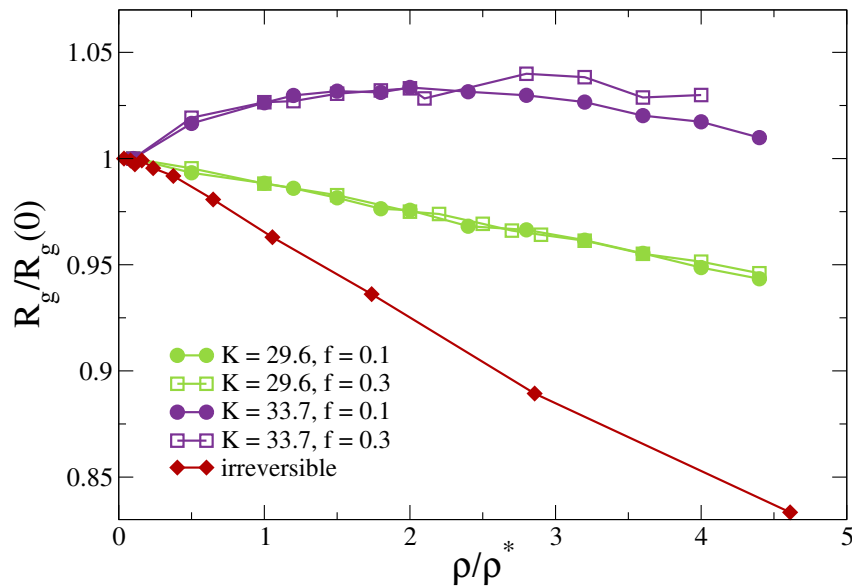

Figure 5.8: Normalized radius of gyration for different values of energy constant K and reactive monomer fraction f as well as for irreversible SCNPs as a function of density.

A first measure for structural changes upon increasing the density is the size of the polymers, given by the radius of gyration (see Equation 3.5). It is depicted in Figure 5.8. We find that the competition between steric repulsion and partial unfolding leads
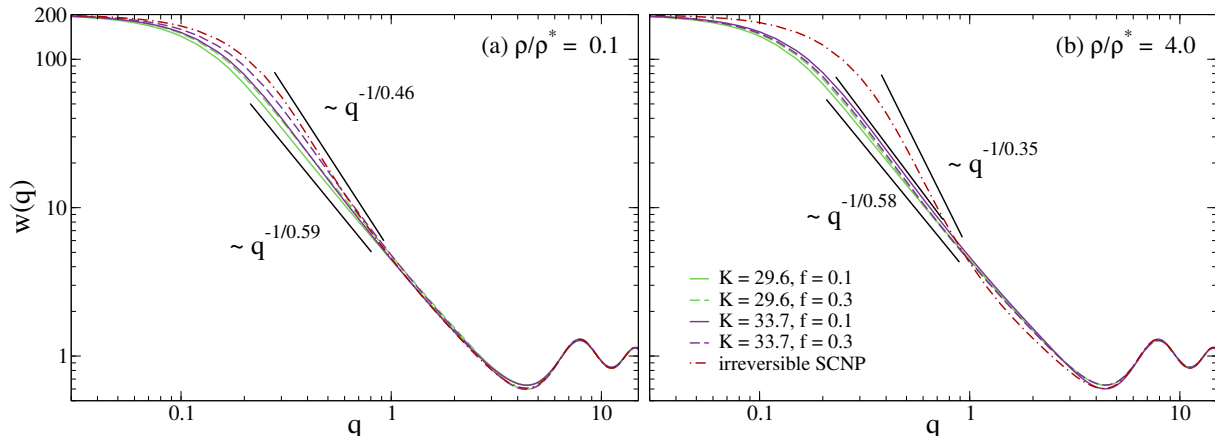
Figure 5.9: Intramolecular form factor $w(q)$ for all (f, K) parameter combinations at densities of (a) $\rho/\rho^\star = 0.1$ and (b) $\rho/\rho^\star = 4.0$, below and above the percolation threshold for all parameters, respectively. Dot-dashed lines are data for irreversibly cross-linked SCNPs. Solid black lines are power laws representing the approximate scaling of $w(q)$ in the fractal regime.

to qualitatively different density dependences of the polymer size for different bond parameters. For $K = 29.6$, shrinking due to macromolecular crowding dominates, whereas for the strong association energy $K = 33.7$, the polymers swell slightly compared to their conformations at high dilution. At high densities, however, a re-entrance of R_g can be observed. For comparison, we include the behavior of irreversibly cross-linked SCNPs (no intermolecular bonds) under crowding conditions, whose collapse behavior is much more pronounced and resembles that of ring polymers in melts [45]. For the remainder of this chapter, whenever we refer to SCNPs for comparison, we mean topologically polydisperse solutions of single-chain nanoparticles, which where obtained by an irreversible cross-linking procedure at infinite dilution, such that no intermolecular bonds are present in the system (see simulation details of Chapters 3 or 4).

A more detailed description of the intramolecular structure of the chains is given by their isotropic form factors,

$$w(q) = \left\langle \frac{1}{N} \sum_{j,k} \frac{\sin(qr_{jk})}{qr_{jk}} \right\rangle , \qquad (5.2)$$

where the sum only includes monomers j, k belonging to the same polymer. Being fractal objects, the form factors of polymers typically follow a scaling law $w(q) \sim q^{1/\nu}$ for wave vectors corresponding to length scales bigger than the bond length b, but smaller than the radius of gyration, i.e. $1/R_g \lesssim q \lesssim 1/b$. Figure 5.9 displays the form factors for all (f, K) parameter combinations at a low density ($\rho/\rho^\star = 0.1$, Figure 5.9a) and a high density ($\rho/\rho^\star = 4.0$, Figure 5.9b), beyond the percolation threshold for all parameters. The differences in scaling between the different parameter combinations are subtle and

almost vanish at a high density, when a system spanning network is formed. Below the overlap concentration, the scaling exponents adopted by the chains with a higher bond probability at $\rho \to 0$ are systematically lower than for those with lower p_B (compare with Table 5.1). This corresponds to the local compaction induced by the intermolecular bonds. Interestingly, even chains with $K = 33.7$ and $f = 0.3$, whose bond probability $p_\mathrm{B} = 0.97$ is very close to 1, still exhibit pronounced differences with irreversible SCNPs (red dot-dashed lines). Indeed, a recent review of experimental data of reversible SCNPs in high dilution showed that their structure is well described by a self-avoiding walk with a Flory-like scaling of $\nu \approx 0.6$, regardless of specific polymer chemistry or reversible interaction (e.g. hydrogen bonds, disulfide bridges, complex formation) [60]. This scaling is also found in our system for the lower bond strength $K = 29.6$. The deviation from the self-avoiding character when the bond life-time approaches infinity (irreversible case) is a kinetic effect that stems from the occasional arrest of a rare conformation through the formation of a long-range loop.

Beyond the percolation threshold, the form factors of the polymers of different bond strength and reactive fraction are nearly indistinguishable. Their scaling exponent $\nu \approx 0.58$ still corresponds to self-avoiding conformations, which could reflect that long-range intramolecular loops are more likely to be exchanged for intermolecular bonds than short-range ones. As discussed earlier, this can be explained by a gain in structural entropy via the opening of long-range loops (Figure 5.3). We also note that the cross-links in irreversible SCNPs render them less penetrable (concatenation of permanent loops is not possible), which leads to their collapse to crumpled globules [45].

The structure of the whole system can be probed by calculating correlations between all monomers j, k, also those belonging to different polymers. The resulting structure factor,

$$S(\mathbf{q}) = \left\langle \frac{1}{N} \sum_{j,k} \exp\left[i\mathbf{q} \cdot (\mathbf{r}_j - \mathbf{r}_k)\right] \right\rangle,$$
(5.3)

is shown in Figure 5.10 for $K = 33.7$ and $f = 0.3$ at various densities. The other parameters show qualitatively the same behavior and are therefore not shown. As a comparison, we include the structure factors for irreversible SCNPs at comparable densities. In the intermediate to high-q range, both the reversibly bonded polymers as well as the irreversible, purely intramolecularly cross-linked SCNPs exhibit qualitatively the same behavior. In the limit of $q \to 0$ the structure factor expresses the compressibility χ of the material
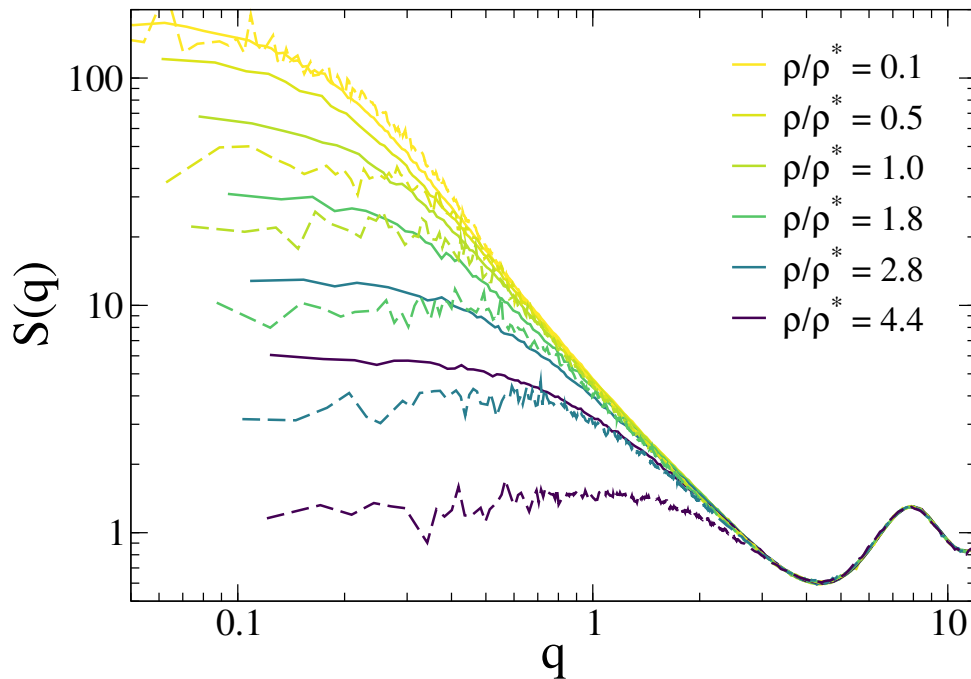
$$\lim_{q \to 0} S(q) = \chi \rho k_B T.$$
(5.4)

Figure 5.10: Intermolecular structure factors for reversible chains (solid lines) with reactive monomer fraction of $f = 0.3$ and $K = 33.7$. Dashed lines represent data for irreversibly cross-linked SCNPs.

Apart from high dilution ($\rho/\rho^\star = 0.1$), the low-q plateau is significantly and consistently lower for the solution formed by irreversible SCNPs than for the network made up of reversibly bonded chains. The permanent cross-links in irreversible SCNPs prevent interpenetration of different SCNPs, rendering the system less compressible than the reversible network at a given density. Furthermore, the structure factor shows no sign of phase separation or inhomogeneities in the system (through diverging or growing $S(q \to 0)$).

To assure that no phase separation is indeed intervening with gelation, we investigate density fluctuations in the system. To this end, the box is divided into sub-boxes of a defined side-length L_s and the monomer density ϕ is calculated within each of them. Density fluctuations are then defined by the demixing parameter

$$\sigma_\phi = \left\langle (\phi - \langle \phi \rangle)^2 \right\rangle, \tag{5.5}$$

where the average is both taken over all sub-boxes and over various conformations. If phase separation occurs, we should observe a sharp increase in density fluctuations for a certain density. One has to keep in mind that the choice of L_s influences the results of σ_ϕ. If L_s is too small, fluctuations are inherently limited, while if it is too big, the phase occupying less volume might not be properly sampled. We varied L_s in the range $3 \leq L_s \leq 20$ and obtained most consistent results with $L_s = 5$.

As demonstrated in Figure 5.11, we observe no clear signs of a phase separation within
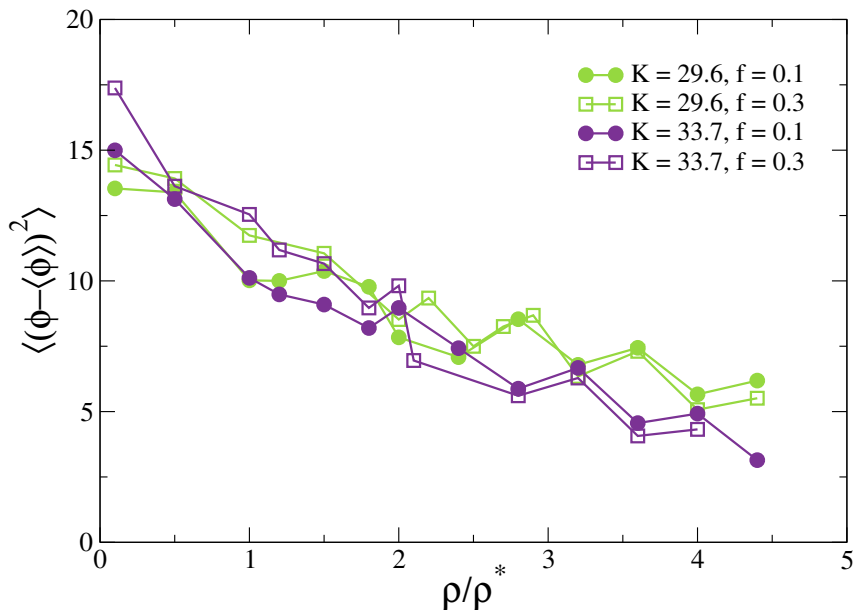
Figure 5.11: Average monomer density fluctuation for a bin size of $L_{\text{bin}} = 5\sigma$ for different values of energy constant K and reactive monomer fraction f.

the investigated parameter space, consistent with the behavior of the structure factor. However, the increased values of σ_ϕ at low densities $\rho/\rho^\star < 1$, suggest that the two lowest investigated densities might be close to or lie within the phase separated region. Since the system is finite, density fluctuations are limited and cannot diverge, such that the evaluation of the phase diagram for small densities is quite challenging. We hope to better sample this parameter space in future research.

Density fluctuations furthermore decrease with increased density. This can be explained by the self-avoiding conformations adopted by the chains upon increasing the density. At low densities, primarily intramolecular bonds are present in the polymers, leading to their local compaction and separation from other polymers. The higher the density, the more intramolecular bonds are exchanged for intermolecular ones. This leads to more interpenetration and entanglements and at the same time, locally less compact structures and thus decreased density fluctuations.

5.3.4   Dynamic Properties

After having discussed in detail the structural properties of the gels formed through the reversible intermolecular bonds, we now shift our focus to the dynamics of the system. First, we calculate the mean-squared displacement of the individual monomers,

$$\text{MSD}(t) = \langle (\boldsymbol{r}_i(t) - \boldsymbol{r}_i(0))^2 \rangle , \tag{5.6}$$
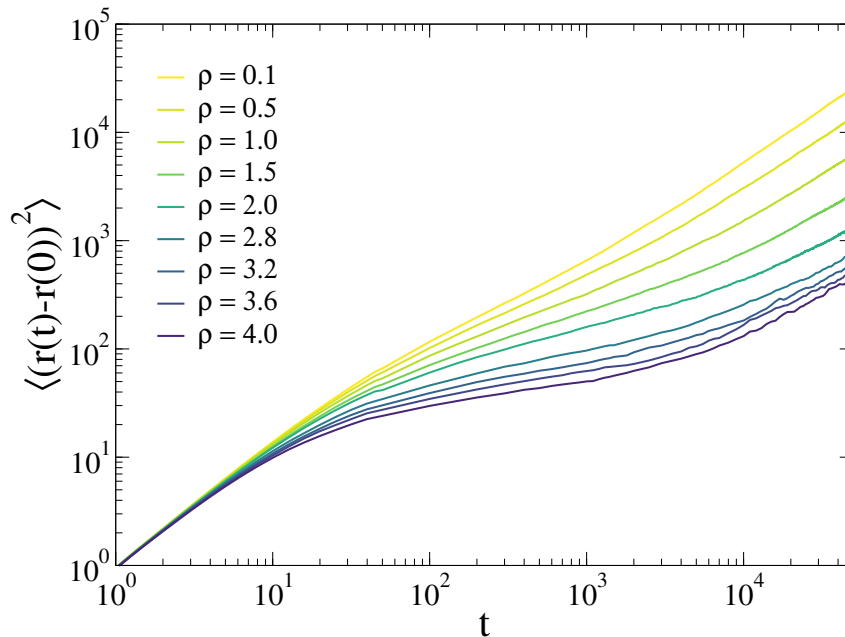
Figure 5.12: Monomer mean-squared displacement for $K = 33.7$ and $f = 0.3$ at various densities.

where angular brackets denote both a time and ensemble average.

Figure 5.12 displays the MSD of $K = 33.7$ and $f = 0.1$ at various densities. Other parameters display qualitatively the same trends (not shown). At short time-scales, monomers diffuse freely without a density dependence. Upon increasing the density, a clear plateau appears in the MSD, marking a slowing down of the dynamics. At the highest density considered, this plateau extends over more than an order of magnitude in time. The square-root of the value of the MSD at this plateau, sometimes called the localization length, $\Delta = \sqrt{\mathrm{MSD}(t^\star)} \approx 5 - 8$, is of the order of the radius of gyration of the polymers. This is quite large, given that on average every third monomer along the chain is reactive and could potentially be engaged in a bond that strongly limits fluctuations.

One should note that the lack of an intermediate Rouse dynamics ($\mathrm{MSD}(t) \sim t^{0.6}$) prior to the plateau regime, typical of polymers is absent here because of the low friction constant employed to speed up equilibration and sampling. At large time-scales, monomers reach a diffusive regime, characterized by $\mathrm{MSD} \sim 6Dt$, with diffusion constant D. Still, the large localization length and the progressive slowing down reflected in Figure 5.12 are clear signatures of approaching a gel transition. The values of D for different parameters are presented in Figure 5.13.

Finally, we investigate the bond dynamics and the reorganization of the percolating cluster once it is formed. We first ask whether the lifetime of intermolecular bonds is affected by gelation or whether cooperativity plays a role in the formation of intermolecular
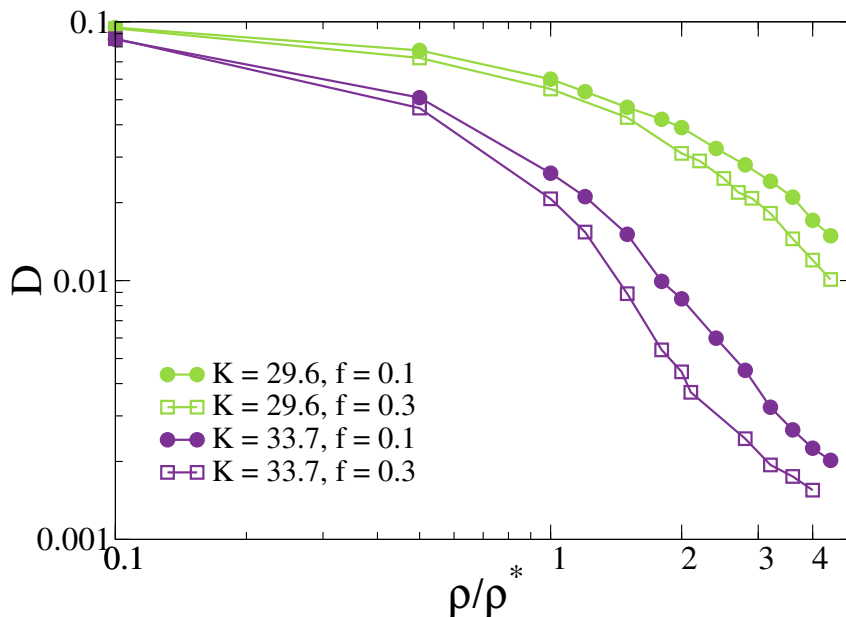
Figure 5.13: Diffusion constant calculated from the monomer mean-squared displacement in the diffusive regime for $K = 33.7, 29.6$ and $f = 0.1, 0.3$ at various densities.

bonds. To this end, we calculate the intermolecular bond autocorrelation

$$S_{\text{inter}}(t) = \frac{\langle B_{i,j}(t) \cdot B_{i,j}(0) \rangle}{\langle B_{i,j}(0) \rangle^2} , \qquad (5.7)$$

where $B_{i,j}(t) = 1$ if monomers i and j (belonging to different chains) form a bond at time t, which has not been broken since $t = 0$ and $B_{i,j}(t) = 0$ otherwise. Furthermore, we calculate the autocorrelation of the cluster

$$S_{\text{cluster}}(t) = \frac{\langle M_i(t) \cdot M_i(0) \rangle}{\langle M_i(0) \rangle^2} , \qquad (5.8)$$

where $M_i(t) = 1$ if polymer i has been a member of the percolating cluster at all times $0 \leq t' \leq t$ and $M_i(t) = 0$ otherwise. As such, $S_{\text{cluster}}(t)$, is a measure for the average dissociation time from the cluster. Figure 5.14 displays the intermolecular bond autocorrelation as well as the cluster autocorrelation for $f = 0.3$ and for both bond strengths. The bond autocorrelation is not affected by changes in density in both cases and can be well described by an exponential decay, $S_{\text{inter}}(t) \sim e^{-t/\tau}$. This is also true for the intramolecular bonds (not shown), demonstrating that bond breaking is purely governed by temperature (as the bond strength corresponds to an inverse temperature) and bonding is not cooperative. On the other hand, the cluster autocorrelation (weakly non-exponential) is strongly affected by density. For $K = 33.7$, at high densities the percolating cluster becomes so stable that almost no polymers leave it within the simulation time window. This, however, does not mean that the cluster does not rearrange. After all, within the simulation time frame, the monomers still diffuse more than the box length even at $\rho = 4.0$
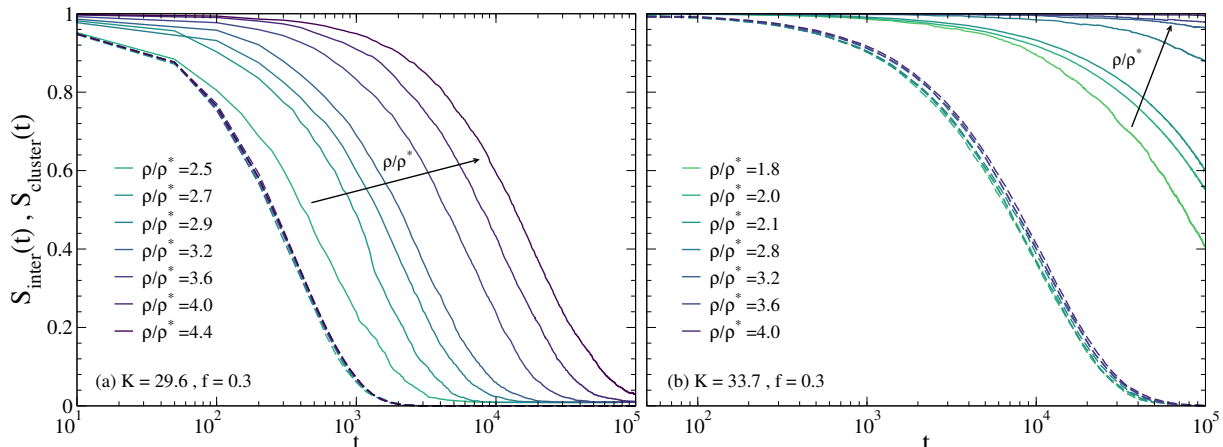
Figure 5.14: Average intermolecular bond ($S_{\mathrm{inter}}(t)$, dashed lines) and cluster (S_{cluster}, solid lines) correlation for $f = 0.3$ and (a) $K = 29.6$, (b) $K = 33.7$. Only densities in which a percolating cluster is at least transiently present are considered.

(see Figure 5.12). An average of 6 intermolecular contacts, however, allows polymers to move through the cluster, breaking and reforming bonds, without ever detaching from it. This stability of the cluster, along with its potential to rearrange, could lead to an interesting behavior under external stresses, which should be investigated in future work. Furthermore, it is not clear whether intermolecular or intramolecular bonds would break first under shear, potentially leading to an interesting viscoelastic response.

At intermediate densities, chains do detach from the cluster from time to time and move through the system before getting reabsorbed in it again. We calculate the time a polymer spends outside of the percolating cluster before reattaching and report the results in Figure 5.15. Surprisingly, the distributions of times spent outside the main percolating cluster is independent of the number of reactive monomers (governed by the reactive monomer fraction f) and the density. We find a universal distribution solely dependent on the bond strength K that follows a stretched exponential $p(t_c) \sim e^{-(t/\tau_c)^\beta}$. Since diffusion depends strongly on density, we believe that the reattachment time is not controlled by the time it takes to reach a different reactive monomer, but rather the time it takes to break a bond, so that a different bonding partner becomes available.
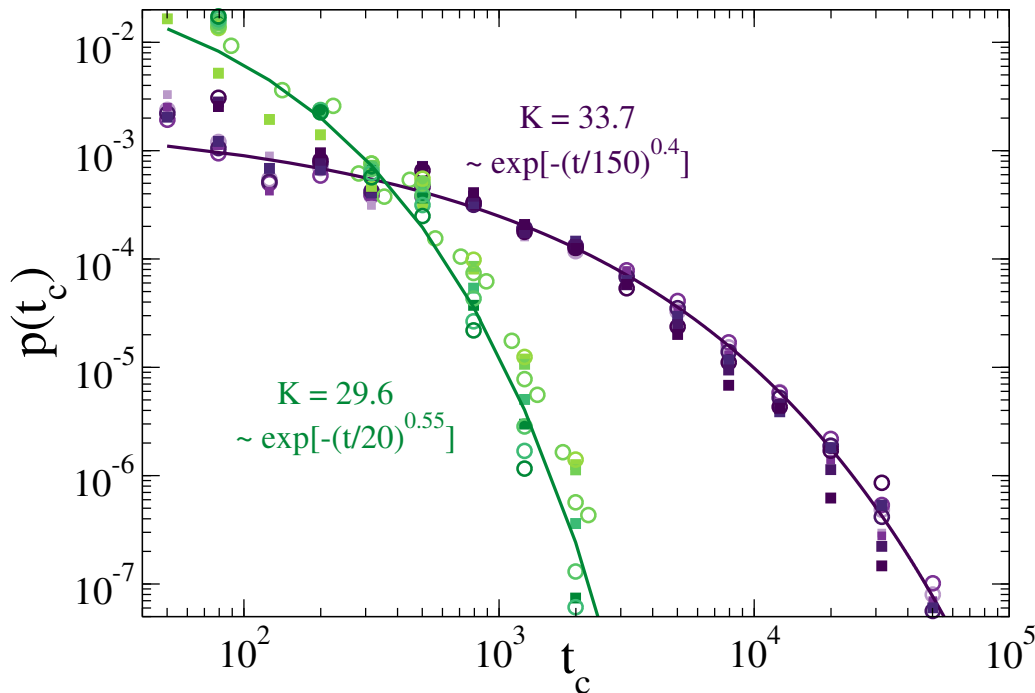
Figure 5.15: Distribution of times a polymer spends outside the system-spanning cluster for $K = 29.6$ (green symbols) and $K = 33.7$ (purple symbols). Data correspond to both $f = 0.1$ (squares) and $f = 0.3$ (circles) at various densities above the percolation threshold. Darker colours correspond to higher densities. Solid lines are fits to stretched exponential functions.

5.4 Conclusion

In this chapter, we have investigated the gel formation of linear polymer chains decorated with functional groups with the ability to form reversible bonds. We employed Langevin dynamics simulations and a reversible bond potential that mimics the reversible covalent bonds currently in use experimentally for the synthesis of reversible single-chain nanoparticles. A specific system of thermoreversible polymers with the potential to switch between a SCNP solution and a hydrogel in response to external triggers [24] has recently attracted a lot of attention to the interplay of intra- and intermolecular bonds. Here, we studied in detail the competition between these two types of bonds and showed that the replacement of intramolecular links by intermolecular ones prohibits a treatment of the system via Wertheim theory. As such, we were limited to investigating a finite set of state points and could not elucidate the complete phase diagram. Nonetheless, we found that the formation of a system-spanning cluster indeed takes place at relatively low monomer densities due to the inherently limited valence of the polymers. Furthermore, the percolation transition can be well described by Flory-Stockmayer theory.

Surprisingly, we showed that the introduction of intermolecular bonds induces a non-

monotonic dependence of the radius of gyration on the density for high bond strengths, while the polymers collapse to a small degree for lower bond strengths. However, the conformations adopted by the chains beyond the percolation transition can be described by self-avoiding walk statistics independent of the bond strength, as is evidenced by the scaling of the form factor $w(q) \sim q^{0.58}$. This result represents a strong difference between the structure of a semi-dilute system of irreversible SCNPs [45, 46] and a reversible SCNP gel. The purely intramolecular irreversible cross-links present in the former prevent entanglements and interpenetration of two chains, which leads to an effective repulsion between two polymers and collapse to crumpled globules. In the reversible case, the intramolecular bonds creating steric hindrance and topological interactions between two chains can be broken and the microsegration seen in irreversible SCNPs is circumvented, making the system significantly more compressible in the process.

Finally, we demonstrated that the dynamics of the system display the typical caging phenomena expected for gelling materials in the mean-square displacement. The reorganization dynamics of the percolating cluster, however, exhibit a remarkable universal behavior: the time a polymer spends outside of the main cluster is independent of density and solely depends on the bond lifetime, which suggests that reattachment to the percolating cluster is limited by the availability of free reactive groups and not the diffusion of the free chain.

In conclusion, we believe that our results present valuable preliminary insights into the gelling process of reversibly cross-linking polymers with randomly distributed functional groups. The competition between intra- and intermolecular bonds leads to complex structural rearrangements purely governed by entropical contributions. However, systems in which such a competition is present have not been studied extensively theoretically or by computer simulations in the literature to this date. We hope that our results will motivate further research efforts in this direction.

References

[1] M. Gonzalez-Burgos, A. Latorre-Sanchez, and J. A. Pomposo, "Advances in single chain technology," *Chemical Society Reviews*, vol. 44, no. 17, pp. 6122–6142, 2015.

[2] S. Mavila, O. Eivgi, I. Berkovich, and N. G. Lemcoff, "Intramolecular cross-linking methodologies for the synthesis of polymer nanoparticles," *Chemical reviews*, vol. 116, no. 3, pp. 878–961, 2016.

[3] A. M. Hanlon, C. K. Lyon, and E. B. Berda, "What is next in single-chain nanoparticles?," *Macromolecules*, vol. 49, no. 1, pp. 2–14, 2016.

[4] O. Altintas and C. Barner-Kowollik, "Single-chain folding of synthetic polymers: a critical update," *Macromolecular rapid communications*, vol. 37, no. 1, pp. 29–46, 2016.

[5] C. K. Lyon, A. Prasher, A. M. Hanlon, B. T. Tuten, C. A. Tooley, P. G. Frank, and E. B. Berda, "A brief user's guide to single-chain nanoparticles," *Polymer Chemistry*, vol. 6, no. 2, pp. 181–197, 2015.

[6] A. Sanchez-Sanchez and J. A. Pomposo, "Single-chain polymer nanoparticles via non-covalent and dynamic covalent bonds," *Part. Part. Syst. Charact.*, vol. 31, no. 1, pp. 11–23, 2014.

[7] M. Artar, E. Huerta, E. Meijer, and A. R. Palmans, "Dynamic single chain polymeric nanoparticles: from structure to function," in *Sequence-Controlled Polymers: Synthesis, Self-Assembly, and Properties*, pp. 313–325, ACS Publications, 2014.

[8] O. Altintas and C. Barner-Kowollik, "Single chain folding of synthetic polymers by covalent and non-covalent interactions: Current status and future perspectives," *Macromol. Rapid Commun.*, vol. 33, no. 11, pp. 958–971, 2012.

[9] M. Seo, B. J. Beck, J. M. Paulusse, C. J. Hawker, and S. Y. Kim, "Polymeric nanoparticles via noncovalent cross-linking of linear chains," *Macromolecules*, vol. 41, no. 17, pp. 6413–6418, 2008.

[10] E. J. Foster, E. B. Berda, and E. Meijer, "Metastable supramolecular polymer nanoparticles via intramolecular collapse of single polymer chains," *Journal of the American Chemical Society*, vol. 131, no. 20, pp. 6964–6966, 2009.

[11] T. Terashima, T. Mes, T. F. A. De Greef, M. A. J. Gillissen, P. Besenius, A. R. A. Palmans, and E. W. Meijer, "Single-chain folding of polymers for catalytic systems in water," *Journal of the American Chemical Society*, vol. 133, no. 13, pp. 4742–4745, 2011. PMID: 21405022.

[12] N. Hosono, M. A. Gillissen, Y. Li, S. S. Sheiko, A. R. Palmans, and E. Meijer, "Orthogonal self-assembly in folding block copolymers," *Journal of the American Chemical Society*, vol. 135, no. 1, pp. 501–510, 2012.

[13] S. Burattini, H. M. Colquhoun, J. D. Fox, D. Friedmann, B. W. Greenland, P. J. Harris, W. Hayes, M. E. Mackay, and S. J. Rowan, "A self-repairing, supramolecular polymer system: healability as a consequence of donor–acceptor π–π stacking interactions," *Chemical communications*, no. 44, pp. 6717–6719, 2009.

[14] E. A. Appel, J. Dyson, J. del Barrio, Z. Walsh, and O. A. Scherman, "Formation of single-chain polymer nanoparticles in water through host–guest interactions," *Angewandte Chemie International Edition*, vol. 51, no. 17, pp. 4185–4189, 2012.

[15] F. Wang, H. Pu, and X. Che, "Voltage-responsive single-chain polymer nanoparticles via host–guest interaction," *Chemical Communications*, vol. 52, no. 17, pp. 3516–3519, 2016.

[16] J. Huh, H. J. Park, K. H. Kim, K. H. Kim, C. Park, and W. H. Jo, "Giant thermal tunability of the lamellar spacing in block-copolymer-like supramolecules formed from binary-end-functionalized polymer blends," *Advanced Materials*, vol. 18, no. 5, pp. 624–629, 2006.

[17] H. Hofmeier and U. S. Schubert, "Combination of orthogonal supramolecular interactions in polymeric architectures," *Chemical Communications*, no. 19, pp. 2423–2432, 2005.

[18] J.-F. Gohy, H. Hofmeier, A. Alexeev, and U. S. Schubert, "Aqueous micelles from supramolecular graft copolymers," *Macromolecular Chemistry and Physics*, vol. 204, no. 12, pp. 1524–1530, 2003.

[19] B. T. Tuten, D. Chao, C. K. Lyon, and E. B. Berda, "Single-chain polymer nanoparticles via reversible disulfide bridges," *Polymer Chemistry*, vol. 3, no. 11, pp. 3068–3071, 2012.

[20] B. S. Murray and D. A. Fulton, "Dynamic covalent single-chain polymer nanoparticles," *Macromolecules*, vol. 44, no. 18, pp. 7242–7252, 2011.

[21] A. Sanchez-Sanchez, D. A. Fulton, and J. A. Pomposo, "ph-responsive single-chain polymer nanoparticles utilising dynamic covalent enamine bonds," *Chemical Communications*, vol. 50, no. 15, pp. 1871–1874, 2014.

[22] J. He, L. Tremblay, S. Lacelle, and Y. Zhao, "Preparation of polymer single chain nanoparticles using intramolecular photodimerization of coumarin," *Soft Matter*, vol. 7, no. 6, pp. 2380–2386, 2011.

[23] P. G. Frank, B. T. Tuten, A. Prasher, D. Chao, and E. B. Berda, "Intra-chain photodimerization of pendant anthracene units as an efficient route to single-chain nanoparticle fabrication," *Macromolecular rapid communications*, vol. 35, no. 2, pp. 249–253, 2014.

[24] D. E. Whitaker, C. S. Mahon, and D. A. Fulton, "Thermoresponsive dynamic covalent single-chain polymer nanoparticles reversibly transform into a hydrogel," *Angewandte Chemie International Edition*, vol. 52, no. 3, pp. 956–959, 2013.

[25] E. Zaccarelli, "Colloidal gels: equilibrium and non-equilibrium routes," *Journal of Physics: Condensed Matter*, vol. 19, no. 32, p. 323101, 2007.

[26] S. Corezzi, D. Fioretto, D. Puglia, and J. M. Kenny, "Light scattering study of vitrification during the polymerization of model epoxy resins," *Macromolecules*, vol. 36, no. 14, pp. 5271–5278, 2003.

[27] E. Del Gado, A. Fierro, L. de Arcangelis, and A. Coniglio, "A unifying model for chemical and colloidal gels," *EPL (Europhysics Letters)*, vol. 63, no. 1, p. 1, 2003.

[28] I. Saika-Voivod, E. Zaccarelli, F. Sciortino, S. V. Buldyrev, and P. Tartaglia, "Effect of bond lifetime on the dynamics of a short-range attractive colloidal system," *Physical Review E*, vol. 70, no. 4, p. 041401, 2004.

[29] L. Rovigatti and F. Sciortino, "Self and collective correlation functions in a gel of tetrahedral patchy particles," *Molecular Physics*, vol. 109, no. 23-24, pp. 2889–2896, 2011.

[30] J. Groenewold and W. Kegel, "Colloidal cluster phases, gelation and nuclear matter," *Journal of Physics: Condensed Matter*, vol. 16, no. 42, p. S4877, 2004.

[31] F. Sciortino, P. Tartaglia, and E. Zaccarelli, "One-dimensional cluster growth and branching gels in colloidal systems with short-range depletion attraction and screened electrostatic repulsion," *The Journal of Physical Chemistry B*, vol. 109, no. 46, pp. 21942–21953, 2005.

[32] E. Zaccarelli, S. Buldyrev, E. La Nave, A. Moreno, I. Saika-Voivod, F. Sciortino, and P. Tartaglia, "Model for reversible colloidal gelation," *Physical review letters*, vol. 94, no. 21, p. 218301, 2005.

[33] P. Segre, V. Prasad, A. Schofield, and D. Weitz, "Glasslike kinetic arrest at the colloidal-gelation transition," *Physical Review Letters*, vol. 86, no. 26, p. 6042, 2001.

[34] V. N. Manoharan, M. T. Elsesser, and D. J. Pine, "Dense packing and symmetry in small clusters of microspheres," *Science*, vol. 301, no. 5632, pp. 483–487, 2003.

[35] Y.-S. Cho, G.-R. Yi, J.-M. Lim, S.-H. Kim, V. N. Manoharan, D. J. Pine, and S.-M. Yang, "Self-organization of bidisperse colloids in water droplets," *Journal of the American Chemical Society*, vol. 127, no. 45, pp. 15968–15975, 2005.

[36] S. Biffi, R. Cerbino, F. Bomboi, E. M. Paraboschi, R. Asselta, F. Sciortino, and T. Bellini, "Phase behavior and critical activated dynamics of limited-valence dna nanostars," *Proceedings of the National Academy of Sciences*, vol. 110, no. 39, pp. 15633–15637, 2013.

[37] L. Rovigatti, F. Smallenburg, F. Romano, and F. Sciortino, "Gels of dna nanostars never crystallize," *ACS nano*, vol. 8, no. 4, pp. 3567–3574, 2014.

[38] M. Wertheim, "Fluids with highly directional attractive forces. i. statistical thermo-dynamics," *Journal of statistical physics*, vol. 35, no. 1-2, pp. 19–34, 1984.

[39] M. Wertheim, "Fluids with highly directional attractive forces. ii. thermodynamic perturbation theory and integral equations," *Journal of statistical physics*, vol. 35, no. 1-2, pp. 35–47, 1984.

[40] E. Bianchi, J. Largo, P. Tartaglia, E. Zaccarelli, and F. Sciortino, "Phase diagram of patchy colloids: Towards empty liquids," *Physical review letters*, vol. 97, no. 16, p. 168301, 2006.

[41] G. M. Whitesides and M. Boncheva, "Beyond molecules: Self-assembly of mesoscopic and macroscopic components," *Proceedings of the National Academy of Sciences*, vol. 99, no. 8, pp. 4769–4774, 2002.

[42] S. C. Glotzer, "Some assembly required," *Science*, vol. 306, no. 5695, pp. 419–420, 2004.

[43] F. Smallenburg and F. Sciortino, "Liquids more stable than crystals in particles with limited valence and flexible bonds," *Nature Physics*, vol. 9, no. 9, p. 554, 2013.

[44] E. Locatelli, P. H. Handle, C. N. Likos, F. Sciortino, and L. Rovigatti, "Condensation and demixing in solutions of dna nanostars and their mixtures," *ACS Nano*, vol. 11, no. 2, pp. 2094–2102, 2017. PMID: 28157331.

[45] A. J. Moreno, F. Lo Verso, A. Arbe, J. A. Pomposo, and J. Colmenero, "Concentrated solutions of single-chain nanoparticles: A simple model for intrinsically disordered proteins under crowding conditions," *J. Phys. Chem. Lett.*, vol. 7, no. 5, pp. 838–844, 2016.

[46] M. Gonzalez-Burgos, A. Arbe, A. J. Moreno, J. A. Pomposo, A. Radulescu, and J. Colmenero, "Crowding the environment of single-chain nanoparticles: A combined study by sans and simulations," *Macromolecules*, vol. 51, no. 4, pp. 1573–1585, 2018.

[47] S. Roldán-Vargas, F. Smallenburg, W. Kob, and F. Sciortino, "Phase diagram of a reentrant gel of patchy particles," *The Journal of chemical physics*, vol. 139, no. 24, p. 244910, 2013.

[48] B. D. Marshall, D. Ballal, and W. G. Chapman, "Wertheim's association theory applied to one site patchy colloids: Beyond the single bonding condition," *The Journal of chemical physics*, vol. 137, no. 10, p. 104909, 2012.

[49] B. M. Mladek and D. Frenkel, "Pair interactions between complex mesoscopic particles from widom's particle-insertion method," *Soft Matter*, vol. 7, no. 4, pp. 1450–1455, 2011.

[50] D. Montarnal, M. Capelot, F. Tournilhac, and L. Leibler, "Silica-like malleable materials from permanent organic networks," *Science*, vol. 334, no. 6058, pp. 965–968, 2011.

[51] F. Sciortino, "Entropy in self-assembly," *Rivista del Nuovo Cimento*, vol. 42, no. 11, pp. 511–548, 2019.

[52] D. Frenkel and B. Smit, *Understanding molecular simulations: from algorithms to applications.* Academic Press, 1996.

[53] P. Flory, "Molecular size in three dimensional polymers. i. gelation. ii. tri-functional branching units. iii. tetrafunctional branching units," *J. Am. Chem. Soc.*, vol. 63, p. 3083, 1941.

[54] W. H. Stockmayer, "Theory of molecular size distribution and gel formation in branched-chain polymers," *The Journal of chemical physics*, vol. 11, no. 2, pp. 45–55, 1943.

[55] W. H. Stockmayer, "Theory of molecular size distribution and gel formation in branched polymers ii. general cross linking," *The Journal of Chemical Physics*, vol. 12, no. 4, pp. 125–131, 1944.

[56] D. Stauffer and A. Aharony, *Introduction to percolation theory.* Taylor & Francis, London, 1992.

[57] D. Stauffer, "Violation of dynamical scaling for randomly dilute ising ferromagnets near percolation threshold," *Physical Review Letters*, vol. 35, no. 6, p. 394, 1975.

[58] S. Kirkpatrick, "Percolation phenomena in higher dimensions: Approach to the mean-field limit," *Physical Review Letters*, vol. 36, no. 2, p. 69, 1976.

[59] D. Stauffer, "Scaling theory of percolation clusters," *Physics reports*, vol. 54, no. 1, pp. 1–74, 1979.

[60] J. A. Pomposo, J. Rubio-Cervilla, A. J. Moreno, F. Lo Verso, P. Bacova, A. Arbe, and J. Colmenero, "Folding single chains to single-chain nanoparticles via reversible interactions: What size reduction can one expect?," *Macromolecules*, vol. 50, no. 4, pp. 1732–1739, 2017.

Chapter 6

Conclusions

6.1   Conclusions and Outlook

Since the beginning of the 21st century, the field of single-chain technology, that is, the precise production of functionalized polymers capable of purely intra-molecular collapse to unimolecular, soft nanoparticles, has seen a veritable boom in literature regarding different polymer chemistries, synthesis procedures and proof-of-concept experiments for potential applications. However, the theoretical description of their structural and dynamical unique characteristics has been poorly explored until fairly recently. In this thesis, we used computer simulations as a powerful tool to add to our understanding of the response of SCNPs in complex environments and elucidate the role of their topological polydispersity. Furthermore, we were able to envision and test new protocols for producing globular nanoparticles to overcome the limitations of the standard synthesis at high dilution. The value of computer simulations in complementing and proposing future experiments is twofold: First, they allow us to access any observable on the single-molecule level, which helps us understand the underlying microscopic mechanism resulting in macroscopic properties probed by experiments. Secondly, our complete control over any variable lets us study several effects independently from each other to gain insight about the dominating contribution governing any process in the system.

In this thesis, we have employed a variety of different simulation methods to study SCNPs in complex environments, propose new synthesis methods and elucidate the consequences of replacing irreversible bonds by reversible ones. The main findings of this work shall be summarized in the following.

In the realm of new synthesis methods, we proposed a novel approach combining different precursor topologies and the presence of purely steric crowder molecules of the same architecture as the precursor. We were able to show that ring polymers constitute promising new candidates for SCNP precursors for the design of compact, globular nanoparticles. While crowding the solution in which synthesis takes place proved to only have minor effects on the size and shape of the produced SCNPs in the case of linear polymers, we found both a compaction and a trend towards more spherical conformations in the case of ring polymers. The resulting "single-ring nanoparticles" (SRNPs) essentially retained, in the swollen state at high dilution, the scaling behavior observed for their precursor molecules at the corresponding density at which synthesis took place. We can explain this effect by the intrinsic topology of ring polymers, which leads to a collapse to crumpled globules under crowding conditions, facilitating the formation of long-range loops and enabling the SRNP to freeze its topology in a typical conformation of the precursor.

Regarding the behavior of SCNPs in complex environments, we performed extensive hydrodynamic simulations of SCNPs in high dilution and semi-dilute systems under homogeneous shear flow. Upon deciphering the intrinsic response of particular topologies through single-molecule simulations, we discovered, to our surprise, that SCNPs of different topologies ranging from sparse to globular exhibit universal scaling laws independent of their specific connectivity for several static and dynamic observables. The set of scaling exponents adopted for the Wi-dependence of the gyration tensor, the orientational resistance, the rotational frequency and the viscosity is characteristic for the sparse network-like character of SCNPs and clearly differs from those found in other polymer architectures. We believe this result allows us to claim that SCNPs constitute a separate class of polymeric nanoparticles in terms of their response to shear flow.

In semi-dilute and crowded solution we have discovered another feature distinguishing SCNPs from simpler polymer architectures, such as linear or star polymers: Contrary to these, whose shear dependence of various static observables depends at most marginally on the concentration, SCNPs exhibit an astounding density dependent response in the intermediate to high Weissenberg number regime. We found two limiting scaling regimes at low and high densities, with a cross-over around the overlap concentration. Interestingly, by comparing mono- and polydisperse solutions, which respond qualitatively in the same way, we could discard the possibility that the interplay of various time-scales produces this effect. Instead, we proposed that it is linked to the intrinsic impenetrabilty of SCNPs and their transition to crumpled globular structures under crowding conditions. This behavior makes them interesting candidates for tuning the rheological properties of advanced materials, especially all-polymer nanocomposites.

Albeit being used routinely experimentally, computational investigations of SCNPs with reversible bonds are mostly lacking to this date. We have presented a preliminary study elucidating the competition between intra- and intermolecular cross-links in a system mimicking dynamic covalent interactions. These are particularly relevant to potential applications due to their responsiveness to external stimuli. Our simulations revealed that the structural properties of reversible SCNPs are qualitatively different from irreversible ones and these differences are augmented by intermolecular bonds that form already at relatively low concentrations. Interestingly, these induce a non-monotonic dependence of SCNP size on density for high bond strengths. Furthermore, we showed that systems of all parameter combinations (bond strength and reactive monomer fraction) form system-spanning clusters in the semi-dilute regime. Finally, we found that the microsegregation present in crowded solutions of irreversible SCNPs is completely absent due to the ex-

change of intra- for intermolecular bonds, which are favored due to a gain in combinatorial entropy.

In conclusion, we believe the outcome of this thesis proves the value of coarse-grained computer simulations for the establishment and advancement of new polymeric systems, which are governed by topology rather than specific chemistries. We hope our results will inspire future experiments, especially the implementation of novel synthesis protocols and rheological measurements of SCNP solutions. Furthermore, the analysis and interpretation of our data has led to additional questions, which could be addressed in subsequent computational investigations, for example: Can we quantify the precise effect of combinatorial entropy in the competition between intra- and intermolecular bonds in reversible SCNPs? How does the presence of both intra- and intermolecular bonds affect the mechanical properties of such a polymeric gel under stress? For every question answered, two more pop up. That's the beauty of science.

6.2 List of Publications

This thesis has contributed to the following publications:

- **Effects of Precursor Topology and Synthesis under Crowding Conditions on the Structure of Single-Chain Polymer Nanoparticles.**

  M. Formanek and A. J. Moreno, *Soft Matter*, 2017, *13*, 6430–6438.

- **Single-Chain Nanoparticles under Homogeneous Shear Flow.**

  M. Formanek and A. J. Moreno, *Macromolecules*, 2019, *52*, 1821–1831.

- **Crowded Solutions of Single-Chain Nanoparticles under Shear Flow.**

  M. Formanek and A. J. Moreno, *submitted to Macromolecules* (2019)

- **Gel Formation in Reversibly Cross-linking Polymers.**

  M. Formanek, L. Rovigatti and E. Zaccarelli, F. Sciortino and A. J. Moreno, *in preparation.*

Acknowledgements

> *"Hope" is the thing with feathers*
> *That perches in the soul*
> *And sings the tune without the words*
> *And never stops - at all -*
> *And sweetest - in the Gale - is heard*
> *And sore must be the storm*
> *That could abash the little Bird*
> *That kept so many warm*
> *I've heard it in the chillest land*
> *And on the strangest Sea*
> *Yet - never - in Extremity,*
> *It asked a crumb - of me.*

— Emily Dickinson, 1862[1]

Anyone who has ever written a PhD thesis will know that it is a serious undertaking that requires discipline, focus and perseverance, but draws just as much strength from creativity, a sense of playfulness and the joy found in one's own work. Perhaps most importantly though, a young writer in the midst of their transition from student to researcher needs the support of mentors, colleagues, friends and family to both initiate them in the way of science, but also pick them up off the floor when the inevitable struggles strike and celebrate the little and big achievements along the way. The little bird called hope perched within them can only guide them towards their goal if it is fed appropriately. *"It takes a village"* is just as true for an independent scientist to blossom as it is for raising a child. And even though at times I felt lonely and isolated in this unfamiliar place I tried to call home for the past three years, I am eternally grateful that I did have my own little village accompanying me on this journey. Now, as it is coming to an end, I would like to pause and take the time to thank all of its inhabitants, so that they may know of the role they have played in the writing of this thesis and the place in my heart they have earned because of it.

First of all, I want to thank my supervisor, Angel Moreno, who has always been available for scientific discussions, but also listened to me when I was discontent and accommodated my wishes regarding research projects. Furthermore, I greatly appreciate

---

[1] T. H. Johnson (Ed.), *The complete poems of Emily Dickinson*, Harvard University Press, 1960.

the supervision I received from Emanuela Zaccarelli and Lorenzo Rovigatti during my stay in Rome. Their ideas were a great inspiration and they made me feel very welcome in their group. I am also grateful for the ongoing presence of Christos Likos in my scientific career, who taught me most of what I know about soft matter and who keeps answering my silly questions to this day.

Staying in the realm of science and work, my heart goes out to my 'simulated' family (pun totally intended), Daniel Arismendi Arrieta and Mariarita Paciolla. You two have kept me out of my shell that I had built here, I don't think you realize how much that means to me. Dani, your advice has always been incredibly valuable and I will miss hearing you say *"poco a poco"* whenever I'm groaning with frustration. To me, you'll always be Dani Uno. Mariarita, your honesty has made me feel a lot less alone since you arrived in Donostia. I wish you all the best with your PhD, I hope the experiences I shared with you will be of some help.

I would also like to thank the rest of the *Polymers and Soft Matter* group, all the PhD students and postdoctoral researchers, who have accompanied me in those past three years, Dani, Beatriz, Paula, Jorge, Isabel, Amaia, Timo, Jordan, Ali, Julen, Javier, Ester, Thomas, Jon, Alex, Natalia, Izaskun and Marina, and our group leader Juan Colmenero for letting me join the group. I would not want to forget the connections I kept to my former group in Vienna. Some of them, especially David Toneian, Ioana Garlea, Ronald Blaak, Lisa Weiss and Max Liebetreu have helped me with intriguing scientific discussions and useful career advice, but most of all have brightened my conference attendances with happy reunions.

Equally important has been my biological family, especially my parents, Susanne Formanek and Sepp Linhart. They have given me their full support in everything I wanted to do throughout my life and have let me get away with more than a few bad decisions, for which I am deeply grateful. Although I ended up choosing a subject very different from theirs, they have shown me what an academic life looks like from the beginning. I remember going to conferences in various countries with them since I was old enough to understand that you are not supposed to speak during a lecture. I learnt that science is not separate from life, but encompasses everything: the extended conference holidays, the friendships forged at conference dinners, the wood-block print collections, the Japanese breakfast for dinner, the analysis of the daughter's favourite TV show, Pokémon, in terms of its incorporation of Japanese myths and fairytales. Now that I have finally decided to step into your footsteps, *Mapa*, I want you to know how much I appreciate having had

this insight into what it means to be a researcher. I hope I can continue to make you proud.

Mama, I would like to thank you especially: As a child with cerebral palsy just barely learning to walk, you believed in my own agency and fought for my right to move as I wanted, even when others considered this freedom dangerous and you a bad mother for granting it. They couldn't have been farther from the truth. Without your encouragement and your own courage, I would not be here today. I love you.

Papa, you have always been a role model for me, a prime example of a true polymath, a species sadly threatened with extinction in today's rapidly moving world, but always fascinating to me. My love for physics and biology was at least partly established during our shared mornings spent reading the newspaper, me devouring the science section while you pondered culture, after we had 'fought' over the politics part.

I would like to thank the Materials Physics Center for granting me a PhD scholarship and for the funding that allowed me to attend conferences and training courses and visit other research groups during my PhD. Not only have these experiences repeatedly sparked my passion for science through the exposure to new ideas, but they have also allowed me to connect with fascinating new people, who I would not have met otherwise. Some of them are part of this work: First and foremost, my wonderful boyfriend Charlie Wand, whose kindness, perseverance and activism are a constant source of inspiration. Our Pokémon gif exchanges kept me smiling at the darkest hours; My PhD partner-in-crime Hugh Barlow, with whom I shared the ups and downs of thesis writing with the occasionally necessary long-distance glass of whisky, but who also kept me human in times when I felt like a cog in some great machinery; Fausto Martelli, who granted me a much-needed break from my PhD that (alongside his encouragement) helped me re-evaluate my relationship with the academic world; Rory Brown, Jenny Wilshaw, Cameron Shand and Giorgiana Neculae, my IBM co-interns, who taught me what teamwork could look like and that learning from one another is one of the most empowering tools available to a scientist; Brandon Green, who, in a time when I felt lost and needed direction, inadvertently showed me that passion is the most important ingredient in science and reminded me that I had to reconnect with mine; Francois Nédéléc and the rest of the Sainsbury Laboratory in Cambridge, who affirmed my successful metamorphosis into a 'real' scientist and whose offer to join them kept me motivated in the last months.

When I decided to start a PhD abroad, I felt very scared about being forgotten and loosing all ties with my home. It makes me even more grateful to have such wonderful

friends, who, whenever I returned for a short visit to Vienna, always made me feel like I had never been away. Special thanks and hugs to: Felicitas Natmessnig, who continues to defy the fragmentation of human communication through instant messaging and social media and whose heart-to-heart calls and long emails have provided the sunshine I needed on rainy Basque days. *Umärmelung*; Angela Koffler and David Toneian for accompanying me on the wonderful trip to Andalusia and happily succumbing to my autocratic holiday planning; The girls of the *Kochklub*, Anita Klemenjak, Marianne Stephanides, Alina Bimashofer and Julia Maderner for pretending like they could not cook without me, even though we all know that our gatherings are not really about the food, but the gossip and lewd tales; Laura Kalb for being my emotional support human, my '[insert mental health problem here] anonymous' group and lately also my virtual gym buddy; Patrick Derflinger for being complicit in my decision to leave and making me realize that leaving is not about taking a plane, but about embracing the unknown.

Finally, as a female, polyamorous bisexual with a semi-visible disability and a mental health disorder, which makes me a minority in physics in several ways, I wish to acknowledge the marginalized scientists that came before me to fight for their place at the table. Their courage, strength and perseverance in the face of exclusion and ridicule is what gave me hope that there could be a place for me, too, and that step by step we will reach the goal of valuing merit over conformity. In the context of the CFM, I would like to thank Idoia Mugika and Daniel Martinez-Tong for their efforts in creating an inclusive work environment.